VNIVERSITAT DE VALÈNCIA

Departament de Física Teòrica

Phenomenology of massive neutrinos: from oscillations to new physics

David Vanegas Forero

TESIS DOCTORAL

Directora: Dra. **Maria Amparo Tórtola Baixauli**

Co-director: Prof. **Jose W. Furtado Valle**

Tutor: Prof. Manuel J. Vicente V.

Valencia

2014

Certificado

Dr. Jose W. Furtado Valle, profesor de investigación del CSIC,
Dra. Maria Amparo Tórtola Baixauli, investigadora contratada por el CSIC,

CERTIFICAN:

Que la presente memoria, 'Phenomenology of Massive Neutrinos: From Oscillations to New Physics', ha sido realizada bajo su dirección en el Departamento de Física Teórica de la Universidad de Valencia por David Vanegas Forero, y que constituye su tesis doctoral para optar al grado de Doctor en Física.

Para que así conste, en cumplimiento de la legislación vigente, presentan en el Departamento de Física Teórica de la Universidad de Valencia la referida Tesis Doctoral, y firman el presente certificado.

Dr. Jose W. Furtado Valle

Dra. Maria Amparo Tórtola Baixauli

A Clara y Gonzalo

Acknowledgments

Quiero agradecer primero a mi 'gente', especialmente a mi madre y a mi hermano, por el apoyo incondicional que siempre me han brindado.

Agradezco al personal del instituto, la universidad y principalmente al grupo AHEP. Quiero agradecer a Jose por haberme vinculado al grupo, brindado todo su apoyo en lo económico, científico y sobre todo por las múltiples y enriquecedoras discusiones de física; y finalmente, por la dirección de esta tesis. A todos los miembros y ex-miembros del grupo AHEP con los que he tenido la fortuna de colaborar y aprender: agradezco a Mariam por su atención, paciencia y dedicación durante el desarrollo de nuestros proyectos y la dirección de esta tesis; agradezco también a Stefano con quien tuve el gusto de colaborar, a Sergio y a Martin por estar pendientes de los asuntos burocráticos y el desarrollo de esta tesis; finalmente, quiero agradecer en general a los 'AHEPians' que me han hecho sentir como en casa y con los cuales he compartido más que el día a día, en particular a Lucho y Vale; también a Caro por compartir conmigo su afición a correr. No podría dejar de agradecer especialmente a Sofiane por las discusiones de variedad de temas, entre tantos otros de física también, pero sobre todo por estar ahí presente de forma incondicional.

Agradezco al profesor Omar por la acogida durante mi breve estancia en el D.F. y con quien he tenido la oportunidad colaborar también.

Quero agradecer ao pessoal do CFTP especialmente ao professor Jorge pela acolhida, durante o tempo que esteve no IST em Lisboa, e pelas discussões em física. Senti-me muito

afortunado de ter tido a oportunidade de colaborar com o professor Jorge. Agradeço também ao pessoal do gabinete 'The Office', pelos bons momentos e as conversas dos cafés; e especialmente ao Leonardo Pedro pelas atividades fora do instituto. Finalmente, quero agradecer à Paula pela sua gentileza e por contar comigo, não vou esquecer as discussões e as viagens que fizemos.

Son muchas las personas con las que he tenido el gusto de compartir el periodo de doctorado y que incidieron de alguna forma en el desarrollo de este proyecto. Es difícil especificar a cada una ellas. Igualmente, muchas gracias a todos!

Contents

Contents ix

Introduction 1

List of publications 10

1 Neutrino oscillations 11

1.1 Neutrino and antineutrino oscillation formalism . . . 12

1.2 Three neutrino framework in vacuum . . . 17

1.3 Neutrino oscillations with matter effects . . . 21

1.3.1 Effective potential . . . 22

1.3.2 Hamiltonian in matter . . . 24

1.3.3 Two neutrino framework . . . 24

1.3.4 Three neutrino framework . . . 28

1.4 Solar and atmospheric neutrinos . . . 30

1.4.1 Solar neutrinos . . . 30

1.4.2 Atmospheric neutrinos . . . 35

1.5 Reactor experiments . . . 40

1.5.1 Reactor event calculation . . . 40

1.5.2 Daya Bay as an example . . . 42

1.6 Accelerator experiments . . . 43
1.6.1 T2K as an example . . . 45
1.7 Global analysis . . . 48
1.8 Results . . . 51
1.8.1 The role of long–baseline neutrino data in atmospheric parameter determination . . . 51
1.8.2 The θ_{23} octant and the CP violation phase δ . . . 52
1.8.3 Summary of global fit . . . 56

2 Neutrino mass model with a flavor symmetry 59
2.1 The A_4 group . . . 60
2.2 A model with degenerate neutrino masses . . . 62
2.3 Babu Ma and Valle (BMV) Model . . . 64
2.4 Modifying the BMV model . . . 69
2.4.1 Charged lepton corrections to lepton mixing . . . 70
2.4.2 Minimal flavon extension of the original A_4 model . . . 70
2.4.3 Neutrino predictions . . . 71
2.5 Analytical understanding . . . 74

3 Neutrino mass and low energy observables 77
3.1 Preliminaries . . . 78
3.2 Neutrino mass in the Electroweak theory . . . 81
3.2.1 The standard type-I see-saw . . . 83
3.3 Low scale see-saw mechanism . . . 84
3.3.1 Lepton number conserving case . . . 85
3.3.2 Inverse see-saw mechanism . . . 86
3.3.3 Linear see-saw mechanism . . . 88
3.4 Unitarity deviation of the lepton mixing matrix . . . 88
3.5 Lepton flavor violation . . . 90
3.5.1 Radiative leptonic decays . . . 91
3.6 Numerical analysis . . . 92
3.6.1 Inverse type-I Seesaw . . . 93

3.6.2 Linear type-I Seesaw . . . 94
3.7 Numerical results . . . 95

4 Non–Standard Interactions at Daya Bay 105
4.1 NSI at reactor experiments . . . 107
4.2 Specific settings . . . 110
4.3 NSI effect on the oscillation probability . . . 112
4.3.1 Effective probability in presence of NSI . . . 112
4.3.2 Correlations between NSI parameters and θ_{13} . . . 114
4.4 Bounds on NSI from Daya Bay data . . . 117
4.4.1 Constraints on electron-NSI couplings . . . 117
4.4.2 Constraints on muon/tau-NSI couplings . . . 120
4.4.3 Constraints for the universal-NSI case . . . 120
4.5 Bounds on NSI from Daya Bay data II . . . 123

Conclusions 127

Appendices 131

A $\mu \to e\gamma$ Branching ratio 133
A.1 Limiting cases . . . 134

B Neutrino oscillation probabilities in presence of NSI for other relevant cases 137
B.1 Case 2 : non-standard interaction at production only . . . 137
B.2 Case 3: Same-size production and detector effect with different phases . . . 138
B.3 Neutrino states with normalization . . . 138

C Matrix block diagonalization 141

Bibliography 143

Introduction

Neutrinos are historically known for being elusive particles. Almost thirty years passed since they were proposed by Pauli in order to be consistent with the observed electron spectrum in β-decay process, to their discovery by Cowan and Reines in the late fifties. Aside of that, neutrinos do not conserve flavor when traveling, which kept busy the neutrino community for almost forty years until it was realized that neutrinos do oscillate. The difficulty comes from the fact that one needs a compromise between the traveled distance and the neutrino energy to be sensitive to neutrino oscillations. However, thanks to the technical improvements, neutrinos are now less elusive. In fact, with the current facilities, we are able to detect neutrinos from several sources, from extraterrestrial origin like the Sun or supernova explosions, as well as from the cosmic protons that collide with the atmosphere. In addition to natural, we also have artificial neutrino sources like reactors and accelerators. Even though the relic neutrinos from the Big Bang have not been directly detected so far, they constitute another background of neutrinos filling the universe. Thus, the neutrino spectrum spans several orders of magnitude in neutrino energy, from eV to PeV.

When the experimental search for neutrinos started in the sixties with the radiochemical experiments, almost all the attention and dedication was directed to the solar neutrino deficit. Later on, with `Kamiokande` at the scene, atmospheric neutrino observations showed that there was a deficit in the expected number of muon neutrinos. The development of new detector technologies such as water Cherenkov detectors was needed to provide real time information.

Only thanks to the reactor experiment KamLAND, the oscillation neutrino pattern started to be unveiled. Another crucial experimental facility was the Sudbury Neutrino Observatory (SNO), sensitive not only to electron neutrinos, as the other solar experiments, but also to the other neutrino flavors through its neutral current (NC) interaction detection process. This new detection technique established the electron neutrino flavor transition to muon and tau neutrinos. Together with the results from Super-Kamiokande (SK) on the zenith dependence of the atmospheric neutrino flux, all the mentioned facilities favor the neutrino oscillation mechanism as the explanation for the neutrino flavor change in solar and atmospheric neutrinos. Roughly this was the situation in 2002.

The neutrino oscillation mechanism is based on the idea that flavor neutrino states are a linear combination of mass eigenstates. A given neutrino flavor state, created in a weak process together with a charged lepton with the same flavor, after traveling a long enough distance, can be detected as a different flavor state. Notice that what is indeed detected is the charged lepton created together with the neutrino. Thanks to the measurement of the Z boson decay width by the electron-positron collider LEP, we know the number of active neutrinos is equal to three, which is the number of flavors in the Standar Model (SM). In the three neutrino framework, the oscillation mechanism relies on six parameters: three mixing angles, two mass squared splittings (defining the solar and atmospheric scales) and a CP violating phase. In order to gain information about those parameters, different neutrino experiments have been designed. In general, neutrino experiments can be classified, according to the neutrino oscillation channel explored, in two types: appearance and disappearance experiments. In an appearance experiment neutrinos are detected with a different flavor with respect to the one present in the initial neutrino beam. On the other side, a disappearance experiment tests the survival probability, i.e how many neutrinos of a given flavor have disappeared when traveling. Current accelerator neutrino experiments are based on muon neutrino and antineutrino beams since a tau beam is experimentally challenging due to the tau decays. Therefore, five oscillation channels can be studied: electron appearance and muon disappearance, running in neutrino and antineutrino modes and also the tau disappearance channel. Accelerator based neutrino experiments are sensitive to the atmospheric mass splitting and mixing angle through the muon disappearance channel, thus they are complementary to the atmospheric neutrino experiments. The other channels one can study at neutrino oscillation experiments are electron

neutrino disappearance from solar neutrinos and antineutrino disappearance from reactors.

Currently, with the design of artificial sources of neutrinos, mainly reactors and accelerators, the attention has moved from the sky to the Earth. As expected, since 2002 neutrino oscillation parameters have been determined more precisely. In particular, the atmospheric mass splitting and very recently the corresponding mixing angle are better determined from the muon disappearance channel at the accelerator experiments MINOS and T2K, respectively. However, the breakthrough in the neutrino field came from the measurement of the last mixing angle by the observation of electron antineutrino disappearance at the Daya Bay, RENO and Double Chooz reactor neutrino experiments in 2012. Likewise, the mentioned accelerator experiments MINOS and T2K, are sensitive to the reactor mixing angle through the electron appearance channel, also sensitive to the Dirac CP phase.

Neutrino oscillations are the leading mechanism that explains the neutrino flavor conversion from all the detected sources. Thus, neutrinos have provided the first experimental evidence for flavor violation in the leptonic sector. In addition, the striking implication from neutrino oscillations is that neutrinos are massive. Using the particle content of the SM, Weinberg showed that it is possible to construct an dimension five effective operator, suppressed by a large scale, that will provide the masses to the neutrinos. However, the origin of this operator has not been understood yet. Since neutrinos do not carry electric charge, a right-handed Majorana mass term is allowed in the Lagrangian of the theory implying a violation of the lepton number by two units. In the SM however, lepton or family number are accidental symmetries and therefore, without the presence of a right-handed neutrino, the neutrinos are massless. Nevertheless there is no fundamental reason why lepton number conservation should be imposed. Consequently, it is expected that a general theory for massive neutrinos includes both Dirac and Majorana mass terms.

Realizations of the Weinberg operator have their origin in seminal works done in the late seventies and eighties, in particular guided by grand unified theories (GUT), motivated by the idea that the scale that suppresses the neutrino masses is close to the GUT scale. In fact, the Kamiokande experiment was originally designed to observe proton decay, in order to test GUT theories. However, having such a big scale, GUT theories can not be probed directly and thus they are not as interesting for neutrino mass generation as a low-scale realization of the Weinberg operator. For instance, in the context of the inverse or linear see-saw mechanism,

the active neutrinos are massless when lepton number conservation is imposed. Once one allows for lepton number violation, active neutrinos become massive and in this case the mass is naturally small since the lepton symmetry is recovered in the massless limit, and without the necessity of any large scale. This point is phenomenologically attractive because those scenarios may be probed at the LHC accelerator.

On the other side, lepton flavor violation (LFV) has not been observed in the charged lepton sector so far. However, many extensions of the SM predict an enhancement of LFV in charged leptons that can be as large as the experimental bounds. In particular, LFV may be enhanced by the inclusion of massive neutrinos. Among the charged LFV processes, leptonic tau and muon decays as well as muon conversion in nuclei provide the strongest constraints. From the experimental side, current facilities like MEG at PSI have improved the limit on the radiative muon decay branching ratio in one order of magnitude with respect to their previous measurement and now the limit is 5.7×10^{-13}, currently the strongest limit for LFV compared with the other mentioned processes. Future sensitivities for the muon to electron conversion in nuclei, in particular from the PRISM group, will improve up to five orders of magnitude the current limits, of the order of $\sim 10^{-12}$. Thus, with current and future sensitivities, charged LFV processes are a powerful tool to exclude or constrain some degrees of freedom in models with a significant contribution to LFV.

Low-scale see-saw models are phenomenologically attractive since they can be tested by low energy observables from neutrino oscillations as well as from the charged LFV. Also, the new energy scale can be at the energy frontier and therefore it can be tested at the LHC. Finally, since these models predict more than three mass eigenstates for the neutrinos, the lepton mixing matrix is rectangular with three rows and more than three columns due to the extra singlet states. However, only the light part, the effective three by three part of the lepton mixing matrix, is observable through neutrino oscillations. Therefore, the three by three part of the lepton mixing matrix is no longer unitary. In the type-I see-saw the lack of unitarity is inversely proportional to the scale that suppresses the neutrino masses, and therefore negligible. Differently, in the low scale see-saw schemes, heavy neutrinos can be at $\sim$ TeV, while neutrino masses are naturally small, producing a unitarity deviation at the percent level that might be seen in oscillation experiments as a zero distance effect.

As it has been discussed, extensions of the SM are needed in order to provide neutrino masses and also other observations such as the baryon asymmetry of the universe and the existence of dark matter (DM). Related to neutrinos, we have roughly described the type-I see-saw and the low-scale see-saw just in the previous paragraph, and we have also mentioned that they can have an origin from GUT inspired models. It is expected that in a particular model beyond the SM, additional neutrino interactions might appear. In order to study those new neutrino interactions in a model-independent way one can use an effective approach parametrizing the extra contribution as general coefficients, as if we had integrated out the heavy field contributions. The standard approach to the phenomenological study of the neutrino non-standard interactions (NSI) consists in parametrizing their strength with respect to the SM effective neutrino interactions, proportional to the Fermi constant. Thus, one may keep the Lorentz structure of the SM with generic dimensionless couplings. We should distinguish between two kinds of NSI: neutral current (NC), which is mostly relevant for neutrino propagation in matter (although it may also affect detection as well), and charged current (CC) NSI that may affect neutrino production and/or detection. There exist many works in the literature constraining NC NSI using oscillation neutrino experiments as well as neutrino elastic scattering data. However, few works are dedicated to constrain the CC NSI and since we are entering in a precision era for the determination of the oscillation neutrino parameters, it is worthy to test the possible impact of CC NSI at current oscillation experiments.

In order to develop the main ideas commented above, the outline of this thesis is the following: in the first chapter we introduce the neutrino oscillation mechanism in general. Then, we focus on the three neutrino framework introducing the parameters involved in the process and how they are determined using the data sets from different sources. Individual reactor and accelerator neutrino experiments are also discussed. We conclude with the results of global fit analysis where we determine the impact of the new data upon all the neutrino oscillation parameters.

Before 2012, the lepton mixing matrix was compatible with particular structure with two large mixing angles, solar and atmospheric, while the reactor mixing angle compatible with zero. This pattern might result from the imposition of a discrete flavor symmetry. Particularly,

the so called tri-bimaximal mixing was a suggestive way to explain the leptonic mixing that can be realized by the A_4 group. However, after the determination of a non zero reactor mixing angle, the tri-bimaximal ansatz is excluded. In the second chapter, we modify the model by Babu, Ma and Valle, which is an A_4 based model, in order to predict a leptonic mixing matrix compatible with current neutrino phenomenology.

Then we move to the study of the low scale seesaw mechanism from a phenomenological point of view. In the third chapter, from a bottom–up approach, we introduce the basic ingredients to obtain inverse and linear seesaw type I realizations by adding extra singlets in the SM. Since those models predict an enhancement of the LFV and large NSI effects that will manifest as a unitarity deviation, we list the current observable limits and we introduce the corresponding theoretical value for radiative charged LFV process branching ratio. Finally, we constrain the amount of NSI using the complementarity between the low energy observables, neutrino oscillations, and the current bounds on radiative charged LFV processes.

Using as a motivation of the NSI prediction the models discussed in chapter 3, in the last chapter we adopt a model independent approach to develop the basic formalism to introduce the NSI. Then, we focus on the CC NSI and we study its effects on the determination of the reactor mixing angle using the Daya Bay data.

Resumen de la tesis

Transiciones de sabor han sido observadas en diferentes fuentes de neutrinos. Históricamente, una cantidad menor de neutrinos solares y atmosféricos fue medida en comparación con lo esperado según los modelos teóricos. En el 2002, el mecanismo de oscilación explicó con éxito el déficit tanto de los neutrinos solares como de los neutrinos atmosféricos. Actualmente, las transiciones de sabor en neutrinos producidos en diversas fuentes como el Sol, la atmósfera terrestre, aceleradores y reactores son correctamente descritas dentro del marco de oscilación de tres neutrinos. Desde el punto de vista teórico, la importancia de la oscilación de neutrinos radica en la existencia de neutrinos masivos no considerada en primera instancia en el modelo estándar de partículas (SM). Por lo tanto la oscilación de neutrinos es una de la evidencias experimentales de física más allá del SM.

El mecanismo de oscilación, puede ser descrito por seis parámetros: tres ángulos de mezcla, una fase de violación CP y dos escalas de masa definidas por la diferencia de masas de neutrinos al cuadrado. Uno de los objetivos de esta tesis es determinar los valores de los seis parámetros en mención, usando la información disponible de los eventos de neutrinos de las diferentes fuentes reportados por las colaboraciones experimentales. A lo largo del primer capítulo de la tesis explicamos en qué consiste el mecanismo de oscilación, las relaciones funcionales entre los parámetros de oscilación y cómo obtener los valores de los parámetros dando ejemplos del análisis de datos experimentales en ciertos canales de oscilación. Finalmente, mostramos los valores de los seis parámetros de oscilación como resultado del análisis

global de los experimentos de neutrinos.

El sector leptónico del SM por lo tanto, debe ser extendido para incluir neutrinos masivos, lo cual lleva a una mayor brecha entre las masas de las partículas de las diferentes familias del SM. Adicionalmente, dos de los ángulos de mezcla, atmosférico y solar, son mucho más grandes que el ángulo de Cabbibo (que caracteriza la mezcla en el sector de quarks). En particular, el ángulo de mezcla atmosférico es compatible con el valor máximo de mezcla. Si asumimos que el ángulo de mezcla medido recientemente en experimentos de reactor es cero, como era el caso antes de 2012, podríamos asumir que la estructura de la mezcla de neutrinos tiene un patrón que puede ser consecuencia de imponer una simetría de sabor. Éste ha sido el punto de partida hacia una formulación basada en simetrías de sabor para explicar el patrón de mezcla en el sector leptónico, en algunos casos incluyendo también el sector de quarks. Sin embargo, el valor del ángulo de mezcla de reactores no es compatible con cero lo cual no es simple de obtener a través de simetrías de sabor. En particular, la estructura conocida como tri-bi-maximal, la cual es obtenida en modelos con la simetría de sabor A_4, está excluida. En el segundo capítulo de esta tesis mostramos cómo a partir de un modelo basado en la simetría de sabor A_4 conseguimos explicar la matriz de mezcla actual en el sector leptónico a través de correcciones al sector cargado.

Está claro que debemos incluir neutrinos masivos en el SM. Sabemos que las masas de los neutrinos pueden ser generadas efectivamente a través de un operador de dimensión cinco pero, sin embargo, no sabemos la naturaleza de dicho operador. Varias formas de generar el operador de dimensión cinco son posibles, algunas implicando una alta escala (del orden de la escala GUT) mientras que otras realizaciones pueden estar a una baja escala (del orden del TeV). Así, los esquemas de baja escala, como el seesaw inverso y lineal, son fenomenológicamente interesantes porque no solo explican la pequeñez de la masa del neutrino sino que también contribuyen a procesos que violan el sabor leptónico (LFV), saturando los limites actuales. Como la escala seesaw es baja en estos modelos, la matriz leptónica de mezcla efectiva no es unitaria lo que produce efectos no estándar (no incluida en el capítulo 1) en la propagación de los neutrinos. En el capítulo 3 estudiamos la desviación de la unitariedad de la matriz de mezcla de los neutrinos usando los límites de procesos que violan el sabor leptónico con leptones cargados. Encontramos que la desviación de la unitariedad, en estos modelos, pude ser hasta del uno por ciento.

Motivados por los efectos no estándar en los modelos de baja escala, como los seesaw tipo inverso y lineal, en el último capítulo estudiamos, de una manera independiente del modelo, las llamadas interacciones no estándar de los neutrinos (NSI). Tras introducir la parametrización de las NSI como operadores de cuatro fermiones con acoplamientos generales proporcionales a la constante de Fermi, determinamos los parámetros específicos que afectan la producción y la detección de neutrinos generados en reactores. Notamos que las NSI afectan la determinación del ángulo de mezcla θ_{13} dependiendo también de los valores de las fases no estándar y de la fase de violación CP. Acotamos los acoplamientos adimensionales de las NSI usando los datos de la colaboración Daya Bay, que son los datos que han determinado mejor el ángulo de mezcla θ_{13}. Encontramos que los limites dependen de los valores de las las fases no estándar y especialmente del tratamiento del error en la determinación de la normalización del flujo de antineutrinos que viene de los reactores.

List of publications

This thesis is based on research articles done in collaboration with AHEP members and external collaborators. The list of papers organized by chapter is the following:

- Chapter 1

  D. V. Forero , M. Tortola and J. W. F. Valle,
  "Global status of neutrino oscillation parameters after Neutrino-2012,"
  Phys. Rev. D **86**, 073012 (2012) arXiv:1205.4018 [hep-ph].

  D. V. Forero , M. Tortola and J. W. F. Valle,
  "Neutrino oscillations refitted,"
  arXiv:1405.7540 [hep-ph].

- Chapter 2

  S. Morisi, D. V. Forero , J. C. Romão and J. W. F. Valle,
  "Neutrino mixing with revamped A_4 flavor symmetry,"
  Phys. Rev. D **88**, 016003 (2013) arXiv:1305.6774 [hep-ph].

- Chapter 3

  D. V. Forero , S. Morisi, M. Tortola and J. W. F. Valle,
  "Lepton flavor violation and non-unitary lepton mixing in low-scale type-I seesaw,"
  JHEP **1109**, 142 (2011) arXiv:1107.6009 [hep-ph].

- Chapter 4

  S. K. Agarwalla, P. Bagchi, D. V. Forero and M. Tortola,
  "Testing Non-Standard Interactions at Daya Bay," [In preparation].

CHAPTER 1

Neutrino oscillations

Neutrino flavor transitions have been observed from different neutrino sources. Historically, less solar and atmospheric neutrinos were measured compared to the theoretical expectations. In the case of the solar neutrino deficit, the SNO measurement of the NC and CC solar neutrino interactions established the electron neutrino flavor conversion into muon or tau neutrinos. In the case of atmospheric neutrinos, the SK measurements showed a zenith angle dependence of the muon neutrino fluxes implying a different number of muon neutrinos observed depending on their arrival direction. The neutrino oscillation mechanism explained the neutrino deficit of both solar and atmospheric neutrinos. Currently, the three neutrino oscillation mechanism successfully explains neutrino flavor transitions in solar, atmospheric, reactor and accelerator experiments. From the theoretical point of view, the importance of neutrino oscillations is that they imply the existence of neutrino masses, not included the SM. Therefore, they are one of the strongest experimental evidences for physics Beyond the SM (BSM).

Neutrino oscillations are probed at different experiments and the relevant parameters have been measured with good precision thanks to the interplay between different sets of neutrino experiments. The goal of this chapter is to establish the six oscillation parameters (three mixing angles, a Dirac CP phase and two mass splittings) from the neutrino experiments. We specifically show the parameters involved and the statistical analysis in the particular cases of

T2K and Daya Bay.

In what follows we describe the basics of the neutrino oscillation mechanism in sections 1.1 to 1.3. Then, we review the main aspects of solar and atmospheric neutrino experiments in section 1.4. The main part of this chapter is devoted to the phenomenological study of reactor and accelerator neutrino experiments with the specific examples of the experiments Daya Bay and T2K in section 1.5 and 1.6, respectively. Finally, we describe the main work that comes out from this phenomenological study, *the global fit analysis* [1, 2].

1.1 Neutrino and antineutrino oscillation formalism

A neutrino of defined flavor α created in a charged current process at time $t = 0$, is represented by a quantum state $|\nu_\alpha\rangle$. Since flavor eigenstates are superpositions of mass eigenstates, it is possible to define the flavor eigenstates in terms of mass eigenstates through the following transformation:

$$|\nu_\alpha\rangle = \sum_k V^*_{\alpha k}|\nu_k\rangle, \tag{1.1}$$

where latin indices represent the neutrino mass eigenstates and V is the mixing matrix. Notice that the number of mass eigenstates has not been specified yet.
Massive neutrinos propagate in vacuum (and in matter). Their propagation is represented in the quantum mechanical description by [3]:

$$|\nu_\alpha(x^\mu)\rangle = \exp\left(-iP^0t + i\vec{P}\cdot\vec{x}\right)|\nu_\alpha\rangle, \tag{1.2}$$

where P^μ is the energy-momentum operator. Now we can calculate the conversion probability from one defined flavor state $|\nu_\alpha\rangle$ to another $|\nu_\beta\rangle$ in a simple way. First, we define the transition amplitude as:

$$A_{\alpha\to\beta}(x^\mu) \equiv \langle\nu_\beta|\exp\left(-iP^\mu x_\mu\right)|\nu_\alpha\rangle \ . \tag{1.3}$$

In the *plane wave approximation*, the mass states $|\nu_k\rangle$ are eigenstates of the energy-momentum operator with the energy eigenvalues:

$$p^0_k = E_k = \sqrt{m^2_k + |\vec{p}_k|^2} \ , \tag{1.4}$$

where $\vec{p}_k$ is the neutrino momentum. The transition amplitude in Eq. (1.3) can then be written as:

$$A_{\alpha\to\beta}(x^\mu) = \sum_k V^*_{\alpha k} \exp\left(-i\, E_k\, t + i\, \vec{p}_k \cdot \vec{x}\right) V_{\beta k} \ . \tag{1.5}$$

One can assume all massive neutrino momenta $\vec{p}_k$ are aligned along $\vec{x}$ and then, the propagation process occurs in one dimension. Within this approximation, the phase in the transition amplitude in Eq. (1.5) is given by:

$$-\ E_k\, t + \ \vec{p}_k \cdot \vec{x} = -\ E_k\, t + \ p_k L \ , \tag{1.6}$$

where we have $|\vec{x}| \equiv L$.

Finally, in order to obtain the transition probability, an additional assumption is made:

- Neutrinos are ultra-relativistic particles, therefore $p_k \gg m_k$ and we can consider $L \approx t$. The phase in Eq. (1.6) can now be written as:

$$-\ E_k\, t + \ p_k L = -(E_k - p_k)L = -\frac{m_k^2}{E_k + p_k} L \approx -\frac{m_k^2}{2E} L \ , \tag{1.7}$$

  where E is the neutrino energy neglecting mass contributions [3].

Notice that to obtain the final expression in Eq. (1.7) we have not made any assumption neither on the values of the neutrino energies nor on the neutrino momentum p_k. In principle energies and momentum have different values for each of the massive neutrinos considered. However, in order to properly include the neutrino momentum distribution in the neutrino propagation, a wave-packet treatment should be used. Here we used the plane wave treatment since for the neutrino experiments we consider it is equivalent to the wave-packet treatment. We refer the interested reader to the books in Refs [3] and [4] and the references therein.

The probability expression is obtained from the transition amplitude in Eq. (1.5) with the phase given in Eq. (1.7):

$$\begin{aligned} P_{\nu_\alpha\to\nu_\beta}(L) &= \sum_{j,k} V^*_{\alpha j} V_{\beta j} V_{\alpha k}\, V^*_{\beta k} \exp\left(-i\, \frac{m_j^2 - m_k^2}{2E}\, L\right) \\ &\equiv \sum_{j,k} Y^j_{\alpha\beta} Y^{k*}_{\alpha\beta} \exp\left(-i\, \frac{\Delta m^2_{jk}}{2E}\, L\right), \end{aligned} \tag{1.8}$$

with the definition of the squared mass difference:

$$\Delta m^2_{jk} \equiv m_j^2 - m_k^2$$

and the two products of the mixing matrix expressed as:

$$Y^{j}_{\alpha\beta} \equiv V^{*}_{\alpha j} V_{\beta j}. \tag{1.9}$$

Here the conjugation of the V matrix will be tagged to the α index in Y. Therefore a flip in the flavor index is equivalent to conjugate Y.
Some general remarks about Eq. (1.8) can be done at this point:

- A non-zero neutrino mass is required in order to have neutrino oscillations. The mixing in the lepton sector then will appear.
- In the three neutrino framework, the dependence with the mass squared difference implies at least two different massive neutrinos since there are two different mass squared splittings, the atmospheric and the solar and the absolute mass scale has not been determined. Thus, one of the three massive neutrinos can remain massless.
- A rephasing in the V matrix columns does not change the probability. This fact will have phenomenological consequences when we will discuss Dirac and Majorana phases.

The neutrino oscillation probability in Eq. (1.8) can be expressed in terms of the real and imaginary parts of quartic products of V (two products of Y), subdividing the sum in three parts:

$$\begin{aligned}
P_{\nu_\alpha \to \nu_\beta}(L) &= \sum_j Y^{j}_{\alpha\beta} Y^{j*}_{\alpha\beta} + \sum_{j>k} Y^{j}_{\alpha\beta} Y^{k*}_{\alpha\beta} \exp\left(-i\,\frac{\Delta m^2_{jk}}{2E}\,L\right) \\
&\quad + \sum_{k>j} Y^{k*}_{\alpha\beta} Y^{j}_{\alpha\beta} \exp\left(i\,\frac{\Delta m^2_{kj}}{2E}\,L\right) \\
&= \sum_j Y^{j}_{\alpha\beta} Y^{j*}_{\alpha\beta} + 2\sum_{j>k} \Re\left\{ Y^{j}_{\alpha\beta} Y^{k*}_{\alpha\beta} \exp\left(-i\,\frac{\Delta m^2_{jk}}{2E}\,L\right)\right\} \\
&= \sum_j Y^{j}_{\alpha\beta} Y^{j*}_{\alpha\beta} + 2\sum_{j>k} \Re\{Y^{j}_{\alpha\beta} Y^{k*}_{\alpha\beta}\} \cos\left(\frac{\Delta m^2_{jk}\,L}{2E}\right) \\
&\quad + 2\sum_{j>k} \Im\{Y^{j}_{\alpha\beta} Y^{k*}_{\alpha\beta}\} \sin\left(\frac{\Delta m^2_{jk}\,L}{2E}\right) \\
&= \sum_j Y^{j}_{\alpha\beta} Y^{j*}_{\alpha\beta} + 2\sum_{j>k} \Re\{Y^{j}_{\alpha\beta} Y^{k*}_{\alpha\beta}\} - 4\sum_{j>k} \Re\{Y^{j}_{\alpha\beta} Y^{k*}_{\alpha\beta}\} \sin^2\left(\frac{\Delta m^2_{jk}\,L}{4E}\right) \\
&\quad + 2\sum_{j>k} \Im\{Y^{j}_{\alpha\beta} Y^{k*}_{\alpha\beta}\} \sin\left(\frac{\Delta m^2_{jk}\,L}{2E}\right).
\end{aligned}$$

Finally, we obtain:

$$P_{\nu_\alpha \to \nu_\beta} = \sum_{j,k} Y^j_{\alpha\beta} Y^{k*}_{\alpha\beta} - 4 \sum_{j>k} \Re\{Y^j_{\alpha\beta} Y^{k*}_{\alpha\beta}\} \sin^2\left(\frac{\Delta m^2_{jk}\, L}{4E}\right) + 2 \sum_{j>k} \Im\{Y^j_{\alpha\beta} Y^{k*}_{\alpha\beta}\} \sin\left(\frac{\Delta m^2_{jk}\, L}{2E}\right). \tag{1.10}$$

The general probability expression in Eq. (1.10) has been calculated without any assumption about the mixing matrix V, which can be in general *non unitary*.

Anti-neutrino oscillations

In analogy with the neutrino state definition in Eq. (1.1), we can define the anti-neutrino states in terms of flavor eigenstates as:

$$|\bar{\nu}_\alpha\rangle = \sum_k V_{\alpha k} |\bar{\nu}_k\rangle, \tag{1.11}$$

and we end up with the same relations we have for neutrinos in Eq. (1.8) and Eq. (1.10) with a re-definition of the coefficient $Y^j_{\alpha\beta}$:

$$\tilde{Y}^j_{\alpha\beta} \equiv V_{\alpha j}\, V^*_{\beta j}. \tag{1.12}$$

Coefficients in Eq. (1.12) are not independent of the coefficients for neutrinos in Eq. (1.9), they are related by:

$$\tilde{Y}^j_{\alpha\beta} = \left(Y^j_{\alpha\beta}\right)^* \quad \text{where} \quad \left(Y^j_{\alpha\beta}\right)^* = Y^j_{\beta\alpha}. \tag{1.13}$$

We can write the anti-neutrino oscillation probability in terms of neutrino coefficients using

the first equality in Eq. (1.13):

$$\begin{aligned}
P_{\bar{\nu}_\alpha\to\bar{\nu}_\beta} &= \sum_{j,k}\tilde{Y}^{j}_{\alpha\beta}\tilde{Y}^{k*}_{\alpha\beta} - 4\sum_{j>k}\Re\{\tilde{Y}^{j}_{\alpha\beta}\tilde{Y}^{k*}_{\alpha\beta}\}\,\sin^2\left(\frac{\Delta m^2_{jk}\,L}{4E}\right)\\
&+ 2\sum_{j>k}\Im\{\tilde{Y}^{j}_{\alpha\beta}\tilde{Y}^{k*}_{\alpha\beta}\}\,\sin\left(\frac{\Delta m^2_{jk}\,L}{2E}\right)\\
&= \sum_{j,k}Y^{*j}_{\alpha\beta}Y^{k}_{\alpha\beta} - 4\sum_{j>k}\Re\{Y^{j*}_{\alpha\beta}Y^{k}_{\alpha\beta}\}\,\sin^2\left(\frac{\Delta m^2_{jk}\,L}{4E}\right)\\
&+ 2\sum_{j>k}\Im\{Y^{*j}_{\alpha\beta}Y^{k}_{\alpha\beta}\}\,\sin\left(\frac{\Delta m^2_{jk}\,L}{2E}\right)\\
&= \sum_{j,k}Y^{j}_{\alpha\beta}Y^{k*}_{\alpha\beta} - 4\sum_{j>k}\Re\{Y^{j}_{\alpha\beta}Y^{k*}_{\alpha\beta}\}\,\sin^2\left(\frac{\Delta m^2_{jk}\,L}{4E}\right)\\
&- 2\sum_{j>k}\Im\{Y^{j}_{\alpha\beta}Y^{k*}_{\alpha\beta}\}\,\sin\left(\frac{\Delta m^2_{jk}\,L}{2E}\right),
\end{aligned} \tag{1.14}$$

where in the last line we have kept the order between the flavor indexes. In this case, we can calculate the anti-neutrino probability from the expression for neutrinos in Eq. (1.10) just flipping the sign in the imaginary part. We have found a relation between neutrino and anti-neutrino oscillation probabilities. This relation can be understood as a CP *transformation* because it relates properties of neutrinos (particles) with their antiparticles. Formally, it is equivalent to:

$$\bar{\nu}_\alpha \to \bar{\nu}_\beta \overset{CP}{\Longleftrightarrow} \nu_\alpha \to \nu_\beta$$

On the other side, a *time reversal transformation* T consists of the interchange of initial and final (anti) neutrino states:

$$\bar{\nu}_\alpha \to \bar{\nu}_\beta \overset{T}{\Longleftrightarrow} \bar{\nu}_\beta \to \bar{\nu}_\alpha$$
$$\nu_\alpha \to \nu_\beta \overset{T}{\Longleftrightarrow} \nu_\beta \to \nu_\alpha$$

Finally, if we apply both transformations CP and T transformations to the (anti) neutrino probabilities we find, assuming CPT conservation:

$$P_{\bar{\nu}_\alpha\to\bar{\nu}_\beta} = P_{\nu_\beta\to\nu_\alpha}, \tag{1.15}$$

which is expected from Eq. (1.13) since the antineutrino coefficients are related to ones for neutrinos through a conjugation and finally the conjugation is equivalent to the α-β interchange.

We summarize this section with some remarks:

- It is well known that CPT is conserved in field theories in which the Standard Model of particle physics is based on. Therefore, the relation in Eq. (1.15) is a consequence of CPT conservation.

- If CPT is conserved, a violation of CP implies a violation of T. Additionally, from Eq. (1.15) neutrinos and antineutrinos must be sensitive to the same oscillation parameters. Later we will see this is the case for accelerator neutrino experiments that run independently in both modes, neutrino and antineutrino.

- Neutrinos can probe whether CP is conserved or not. Following the last lines of Eqs. (1.14) and Eq. (1.10) we see that the effect of the CP transformation is encoded in the imaginary products of the mixing matrix V. Later, in specific framework, we will see that is the case, and the effect can be parametrized as a CP phase(s).

1.2 Three neutrino framework in vacuum

Here we will introduce the standard oscillation mechanism for three generations of neutrinos. This corresponds to the number of active neutrinos in the SM after the measurement of the invisible Z-boson decay width [5]. Within this framework in vacuum it is possible to calculate all neutrino conversion probabilities in an exact way. All that we need are the expressions we have developed in the last two sections.

To this purpose, we should explicitly provide a parametrization for the lepton mixing matrix V. A general parametrization is given in Ref. [6] for any number of flavor states. In general the lepton mixing matrix is not unitary, but here we will assume there are no extra fermion states. In this case, V is unitary. We can write V as a product of three complex rotations:

$$V = \omega_{23}(\theta_{23};\phi_{23})\omega_{13}(\theta_{13};\phi_{13})\omega_{12}(\theta_{12};\phi_{12})\,,$$

or, explicitly:

$$V = \begin{pmatrix} 1 & 0 & 0 \\ 0 & c_{23} & e^{-i\phi_{23}}s_{23} \\ 0 & -e^{i\phi_{23}}s_{23} & c_{23} \end{pmatrix} \begin{pmatrix} c_{13} & 0 & e^{-i\phi_{13}}s_{13} \\ 0 & 1 & 0 \\ -e^{i\phi_{13}}s_{13} & 0 & c_{13} \end{pmatrix} \begin{pmatrix} c_{12} & e^{-i\phi_{12}}s_{12} & 0 \\ -e^{i\phi_{12}}s_{12} & c_{12} & 0 \\ 0 & 0 & 1 \end{pmatrix} \tag{1.16}$$

Before going ahead we want to check the rephase-invariant property of the lepton mixing matrix V. Even if V in Eq. (1.16) has been written in terms of all physical phases ϕ_{ij}, only one combination of them is rephase-invariant and can not be factorized as a diagonal matrix. Therefore, this combination will appear in the neutrino probabilities and it could be observed in neutrino oscillation experiments. In order to find the conditions to obtain the same mixing matrix V after the rephasing by P matrix, the phase shift can be written as:

$$P^{-1}\,V\,P = P^{-1}\omega_{23}(\theta_{23};\phi_{23})P\,P^{-1}\omega_{13}(\theta_{13};\phi_{13})P\,P^{-1}\omega_{12}(\theta_{12};\phi_{12})P\,,$$

Where $P = \text{diag}\left(e^{i\alpha}, e^{i\beta}, e^{i\gamma}\right)$. The left product by P^{-1} redefines the ω_{ij} rows while the right side product by P modifies the columns; therefore only the ω_{ij} off-diagonal elements will be modified by the rephasing. For simplicity we can modify just the ω_{ij} elements for $j > i$. To see how to absorb the P phases $e^{i(p_j - p_i)}$ in the off-diagonal ω_{ij} entries, for $j > i$, $\omega_{ij} = s_{ij}\,e^{-(i\phi_{ij})}$, one should redefine $\phi_{ij} \equiv \phi'_{ij} + p_j - p_i$ what results in the following expression for $P^{-1}\,V\,P$:

$$P^{-1}\,V\,P = \omega_{23}(\theta_{23};\phi'_{23} + \gamma - \beta)\omega_{13}(\theta_{13};\phi'_{13} - \gamma - \alpha)\omega_{12}(\theta_{12};\phi'_{12} + \beta - \alpha),$$

where it is possible to find one combination that does not depend on the P matrix elements [6–8]:

$$I = \phi'_{13} - \phi'_{12} - \phi'_{23} = \phi_{13} - \phi_{12} - \phi_{23}. \tag{1.17}$$

The invariant I implies that we can not redefine the three physical phases in order to obtain a unitary real matrix times a diagonal matrix of phases. With three active neutrinos and three mass eigenstates we have one invariant phase that can be observed in neutrino oscillations. In other words we can not solve ϕ'_{ij} in terms of p_{ij}. In the standard parametrization [5], the phase invariant is assigned to the matrix rotation ω_{13} and the other two phases are factorized out as a diagonal matrix of phases. This assignment is clearly a convention since the order in the product of the rotations is not fixed and then, we can assign the invariant to any of the ω_{ij}. Additionally, we can factorize out as a diagonal matrix of phases only two phases. In Ref. [5], the authors have defined $\alpha = 0$, then the mixing matrix can also be written as:

$$V^{PDG} = \omega_{23}(\theta_{23};0)\omega_{13}(\theta_{13};\delta)\omega_{12}(\theta_{12};0)\,\text{diag}\left(1, e^{i\beta}, e^{i\gamma}\right)\,. \tag{1.18}$$

Here we can map the PDG parametrization to the 'symmetric' parametrization in Eq. (1.16) through the following rephasing relations:

$$\begin{aligned}\delta \equiv I &= \phi_{13} - \phi_{12} - \phi_{23},\\ \beta &= \phi_{12},\\ \gamma &= \phi_{12} + \phi_{23}.\end{aligned}$$

As we already mentioned, from Eq. (1.8) the neutrino oscillation probabilities are given by quartic products of the lepton mixing matrix in such a way that they are invariant after row or column rephasing. Therefore, the phases β and γ in Eq. (1.18) can not be observed in neutrino oscillations, unlike what happens with the invariant phase δ. In this case, keeping only the invariant phase, the PDG parametrization is convenient for studying neutrino oscillations. Unless explicitly quoted we will use the following parametrization for the neutrino mixing matrix:

$$\begin{aligned}V &= \omega_{23}(\theta_{23};0)\omega_{13}(\theta_{13};\delta)\omega_{12}(\theta_{12};0)\\ &\equiv R_{23}(\theta_{23})\omega_{13}(\theta_{13};\delta)R_{12}(\theta_{12}).\end{aligned} \tag{1.19}$$

Here R_{ij} correspond to real rotations. After evaluating the products in Eq. (1.19) we get:

$$V = \begin{pmatrix} c_{12}c_{13} & s_{12}c_{13} & s_{13}e^{-i\delta} \\ -s_{12}c_{23} - c_{12}s_{13}s_{23}e^{i\delta} & c_{12}c_{23} - s_{12}s_{13}s_{23}e^{i\delta} & c_{13}s_{23} \\ s_{12}s_{23} - c_{12}s_{13}c_{23}e^{i\delta} & -c_{12}s_{23} - s_{12}s_{13}c_{23}e^{i\delta} & c_{13}c_{23} \end{pmatrix}. \tag{1.20}$$

To close the discussion about the CP phase that we have explained as the rephasing invariant, let us introduce another way to see the same quantity. An appropriate way to quantify the amount of CP violation is the Jarlskog invariant, defined as:

$$J_{CP} = \Im\left\{Y^1_{\mu e} Y^{3*}_{\mu e}\right\} = V^*_{\mu 1} V_{e1} V_{\mu 3} V^*_{e3} \tag{1.21}$$

that except for a sign, is equal to the imaginary term in Eq. (1.10).

Mass hierarchy

As we have mentioned before, neutrino oscillations are sensitive to the squared mass differences but not to the absolute neutrino mass scale. Given that the Sun produces electron neutrinos and not antineutrinos and as we will see later, from the observation of matter effects in solar

neutrino oscillations, we know $\Delta m^2_{21} > 0$. On the other hand, the non-observation of matter effects associated to atmospheric or accelerator neutrinos so far leaves the sign of the second mass splitting Δm^2_{31} undetermined. Therefore, with three massive neutrinos and $\Delta m^2_{21} > 0$, two orderings are possible: normal and inverted.

The normal hierarchy (NH) scheme is defined by the relation $m_1 < m_2 < m_3$. Then, the absolute neutrino masses can be written as:

$$\begin{aligned} m_1 &= m_0, \\ m_2 &= \sqrt{m_0^2 + \Delta m^2_{21}}, \\ m_3 &= \sqrt{m_0^2 + \Delta m^2_{31}}, \end{aligned} \tag{1.22}$$

where m_0 defines the absolute neutrino mass scale.

The inverted hierarchy (IH) scheme is defined by the relation $m_3 < m_1 < m_2$. Analogous relations for the absolute neutrino masses for the IH case are given by the following expressions:

$$\begin{aligned} m_1 &= \sqrt{m_0^2 + |\Delta m^2_{31}|}, \\ m_2 &= \sqrt{m_0^2 + \Delta m^2_{21} + |\Delta m^2_{31}|}, \\ m_3 &= m_0 \end{aligned} \tag{1.23}$$

Since the neutrino mass hierarchy is still unknown, all our results will be given in terms of each mass ordering.

Constraints on the absolute mass scale can be obtained by measuring the spectrum of electrons near the end point of the single β decay spectrum. The following combination of neutrino parameters is constrained from the measurements:

$$m^2_\beta = \sum_k m^2_k |V_{ek}|^2 \ . \tag{1.24}$$

The most stringent upper bounds on m_β were obtained in the `Troitzk` and `Mainz` experiments [5]:

$$m_\beta < 2.05 \text{ eV} \quad (95\% \text{ C.L}) \ .$$

From the non-observation of the neutrinoless double beta decay process ($0\nu\beta\beta$) it is also possible to constrain the absolute neutrino mass scale, but with a different combination of

parameters:

$$m_{\beta\beta} = \sum_k |m_k V_{ek}^2| \ .$$

This quantity is sensitive to the CP violating phases. This process is of particular interest since the observation of a $0\nu\beta\beta$ event will imply that neutrinos are Majorana particles. The most stringent upper bound on $m_{\beta\beta}$ comes from ^{136}Xe half-life bound obtained at the EXO experiment: $T_{1/2}^{0\nu\beta\beta} \geq 1.6 \times 10^{25}$ years [9]:

$$m_{\beta\beta} \lesssim (0.2 - 0.4) \text{ eV} \quad (90\% \text{ C.L}) \ ,$$

where the range comes from uncertainties in the nuclear matrix elements.

Finally, the sum of the three neutrino masses is constrained by cosmological data. The current bound reported by the Planck collaboration is [10]:

$$\sum_i^3 m_i < (0.23 - 1.08) \text{ eV}, \tag{1.25}$$

at 95% of C.L, where the range of values relies on the data set used in the bound derivation.

1.3 Neutrino oscillations with matter effects

Neutrino propagation in matter differs from vacuum propagation due to neutrino interactions with fermions in the medium. Neutrinos suffer forward scattering while traveling in matter. Even though neutrinos interact weakly, and therefore the neutrino cross section is small, neutrinos can 'feel' the matter potential of the medium depending on the density of fermions in the medium. The neutrino interactions with matter can be encoded as an effective matter potential, as we will show later. Under some special conditions, flavor conversion of (anti)neutrinos propagating in matter can be enhanced by the medium. This effect was first used to explain the deficit of solar neutrinos due to their resonant matter interaction inside the Sun, or MSW, effect that we will introduce later. The resonance condition depends not only on the fermion density but also on the neutrino energy. Thus, atmospheric neutrinos (more energetic than solar) are expected to be modified by Earth matter effects (less dense than the Sun). Even in the case where the resonance condition in not fulfilled, interaction with matter will affect neutrino propagation if neutrinos propagate long enough inside the medium.

1.3.1 Effective potential

Assuming an effective interaction of neutrinos with electrons in the medium (four fermion or Fermi interaction), its charged current (CC) part can be written as:

$$\mathcal{H}_{eff}^{CC} = \frac{G_F}{\sqrt{2}}(j_W)^\dagger_\mu j^\mu_W = \frac{G_F}{\sqrt{2}}[\bar{\nu}_e\gamma^\mu(1-\gamma^5)e][\bar{e}\gamma_\mu(1-\gamma^5)\nu_e] \ ,$$

where G_F is the Fermi constant. After a Fierz transformation we get:

$$\mathcal{H}_{eff}^{CC}(x) = \frac{G_F}{\sqrt{2}}[\bar{\nu}_e(x)\gamma^\mu(1-\gamma^5)\nu_e(x)][\bar{e}(x)\gamma_\mu(1-\gamma^5)e(x)] \ . \tag{1.26}$$

A general form of the effective Hamiltonian in Eq. (1.26) is given by:

$$H_{eff}^{CC} = \frac{G_F}{\sqrt{2}}\bar{\nu}\gamma^\mu(1-\gamma_5)\nu\bar{e}\gamma_\mu(g_V+g_A\gamma_5)e \ , \tag{1.27}$$

where g_V and g_A are the vector an axial-vector coupling constants of the SM, respectively. The effect of the interaction of neutrinos with the medium can be parametrized as an effective potential:

$$V = \langle\Psi|H_{eff}^{CC}|\Psi\rangle \ , \tag{1.28}$$

where Ψ is the wave function of the system neutrino-medium. The medium may consist of normal matter: electrons and nucleons (fermions of the first generation of the SM) or in the case of the interstellar medium, (anti)fermions and electromagnetic fields. With the definition in Eq. (1.28), and considering the propagation of ultra-relativistic neutrinos with helicity -1 in a medium with free electrons, the potential is in general given by [11]:

$$\begin{aligned} V^V(\vec{p}_e) &= \sqrt{2}G_F\, g_V \frac{f_e(\vec{p}_e)}{(2\pi)^3}\left(1-\frac{\vec{p}_e\cdot\widehat{k}_\nu}{E_e}\right), \\ V^A(\vec{\lambda}_e,\vec{p}_e) &= \sqrt{2}G_F\, g_A \frac{f(\vec{\lambda}_e,\vec{p}_e)}{(2\pi)^3}\left[\frac{(\vec{p}_e\cdot\vec{\lambda}_e)}{E_e} - \frac{m_e}{E_e}(\widehat{k}_\nu\cdot\vec{\lambda}_e) - \frac{(\vec{p}_e\cdot\vec{\lambda}_e)(\vec{p}_e\cdot\widehat{k}_\nu)}{E_e(E_e+m_e)}\right], \end{aligned} \tag{1.29}$$

where $\widehat{k}_\nu \equiv \vec{p}_\nu/|\vec{p}_\nu|$, with $\vec{p}_\nu$ being the neutrino momentum and E_e the electron energy. The electron distribution function $f(\vec{\lambda}_e,\vec{p}_e)$ depends on the electron vector polarization $\vec{\lambda}_e$ and the electron momentum $\vec{p}_e$. First and second lines in Eq. (1.29) correspond to the vector and axial-vector interaction contributions, respectively.

Depending on the medium properties, a simple expression for the matter potential can be obtained. For the specific case of the Sun and the Earth, the medium can be considered as isotropic and unpolarized, therefore we have:

- For isotropic medium the average over $\vec{p}_e$ cancels out the second term in Eq. (1.29) for $V^V(\vec{p}_e)$.
- For unpolarized medium $\vec{\lambda}_e = 0$ and therefore V^A vanishes.

These two assumptions imply that only the first term from the vectorial part in Eq. (1.29) contributes to the effective neutrino potential:

$$V^{CC}(x) = \sqrt{2} G_F \, g_V n_e(x), \tag{1.30}$$

where $n_e(x)$ is the number of electrons in the medium:

$$n_e = \sum_{\vec{\lambda}} \int \frac{d^3 p_e}{(2\pi)^3} \, f(\vec{\lambda}_e, \vec{p}_e). \tag{1.31}$$

Neutrinos also interact via Neutral Current (NC) process with the fermions in the medium. The effective NC Hamiltonian is given by:

$$\begin{aligned} \mathcal{H}^{NC}_{eff} &= \frac{G_F}{\sqrt{2}} (j_Z)^\dagger_\mu j^\mu_Z \\ &= \frac{G_F}{\sqrt{2}} \sum_{\alpha=e,\mu,\tau} \left[\bar{\nu}(x)\gamma^\mu \left(1-\gamma^5\right) \nu(x)\right] \sum_f \left[\bar{f}(x)\gamma^\mu \left(g^f_V + g^f_A \gamma^5\right) f(x)\right] \ . \end{aligned} \tag{1.32}$$

All the active neutrinos interact with the fermions in the medium through the effective potential V_{NC} which, under the same assumptions of isotropy and polarization, is given by:

$$V_{NC}(x) = \sqrt{2} G_F \sum_f g^f_V \, N_f(x). \tag{1.33}$$

If the medium is neutral, only the neutrons in the medium contribute to V_{NC} in Eq. (1.33) as a consequence of $g^e_V = -g^p_V$. Now we can explicitly write the total effective potential summing up the CC and the NC contributions as:

$$V_\alpha = V_{CC}\delta_{\alpha e} + V_{NC} = \sqrt{2} G_F \left(N_e \delta_{\alpha e} - \frac{1}{2} N_n\right) \ , \tag{1.34}$$

where we used the SM values for the vectorial couplings.

Because all the active neutrinos feel the NC interaction with the same strength, the effective potential coming from the NC effective interaction can be extracted from the Hamiltonian as a rephasing of the neutrino wave function. If there are extra fermions that do not interact with the SM via CC and NC (for example sterile neutrinos), after the rephasing a $(-V_{NC})$ potential will appear in the corresponding entries in the Hamiltonian. For active neutrinos, however, only the CC contribution to the potential will affect neutrino propagation in matter.

1.3.2 Hamiltonian in matter

From the effective potential in Eq. (1.34) we can write the total Hamiltonian as the vacuum part $\mathcal{H}_0$ plus the interaction contribution $\mathcal{H}_I$:

$$\mathcal{H} = \mathcal{H}_0 + \mathcal{H}_I = \frac{1}{2E} V \,\text{diag}\{0, \Delta m^2_{21}, \Delta m^2_{31}, \dots\} V^\dagger + \text{diag}\{V_{CC} + V_{NC}, V_{NC}, V_{NC}, 0, \dots\} \,, \tag{1.35}$$

which is all that we need to study the neutrino propagation in matter for media like the Sun or the Earth.

Along this work we will consider only three active neutrinos, thus the Hamiltonian in matter is given by:

$$\mathcal{H} = \frac{1}{2E} V \,\text{diag}\{0, \Delta m^2_{21}, \Delta m^2_{31}\} V^\dagger + \text{diag}\{V_{CC}, 0, 0, \} \,. \tag{1.36}$$

The Hamiltonian in Eq. (1.36) is written in the interaction basis and, after its diagonalization, neutrino oscillation probabilities can be computed using the expression for the amplitude in Eq. (1.5). Formally we have found the probability expression in matter, but it implies the diagonalization of Eq. (1.36) which is not always possible in an exact way. In particular, we should remember that the potential V_{CC} is proportional to the density of electrons in the medium, n_e, and it may have a functional dependence with the distance. For instance, in the case of the Sun, the density is nearly a decreasing exponential function of the radius.

In order to develop some concepts and has a theoretical approach to the neutrino propagation in matter, the case of the two neutrinos will be introduced. The two neutrino framework in matter is not only a pure academic case but it can be used to describe how neutrinos propagate in the Sun when oscillations are driven mainly by the mass squared splitting Δm^2_{21}.

1.3.3 Two neutrino framework

In order to discuss some neutrino oscillation properties in matter it is useful to rewrite the Hamiltonian in Eq. (1.36) for the two neutrino case where only one mass splitting appears. Keeping all the terms in Eq (1.36) for the two neutrino case we have:

$$\mathcal{H}' = \frac{1}{2}\begin{pmatrix} \Delta m^2_{21}/2E + V_{CC} & 0 \\ 0 & \Delta m^2_{21}/2E + V_{CC} \end{pmatrix} + \frac{1}{2}\begin{pmatrix} -\frac{\Delta m^2_{21}}{2E}\cos 2\theta + V_{CC} & \frac{\Delta m^2_{21}}{2E}\sin 2\theta \\ \frac{\Delta m^2_{21}}{2E}\sin 2\theta & \frac{\Delta m^2_{21}}{2E}\cos 2\theta - V_{CC} \end{pmatrix} \,.$$

Absorbing the first line as a global phase in the neutrino wave function, we have:

$$\mathcal{H} = \frac{1}{2}\begin{pmatrix} -\frac{\Delta m^2}{2E}\cos 2\theta + \sqrt{2}G_F\, n_e(x) & \frac{\Delta m^2}{2E}\sin 2\theta \\ \frac{\Delta m^2}{2E}\sin 2\theta & \frac{\Delta m^2}{2E}\cos 2\theta - \sqrt{2}G_F\, n_e(x) \end{pmatrix} , \tag{1.37}$$

where for simplicity we have dropped out the 21 subindex. Also, the matter potential has been written explicitly. Even if Eq. (1.37) looks simple, still some specification (and approximations) on the matter density profile $n_e(x)$ should be made in order to understand the physical consequences of the matter potential in the neutrino propagation. The eigenvalues of Eq. (1.37) are easily calculable as:

$$\lambda = \pm\sqrt{\left[\Delta m^2\cos(2\theta) - 2\sqrt{2}E\, G_F\, n_e(x)\right]^2 + \left[\Delta m^2\sin(2\theta)\right]^2}.$$

The neutrino mixing angle in matter can be obtained from the diagonalization condition:

$$U_M^\dagger \mathcal{H} U_M = \frac{1}{2}\text{diag}(\lambda_-/2E, \lambda_+/2E) , \tag{1.38}$$

solving one of the off-diagonal entries, and it is given by:

$$\sin\left[2\theta_M(x)\right] = \frac{\Delta m^2\sin(2\theta)}{|\lambda|} = \frac{\Delta m^2\sin(2\theta)}{\sqrt{\left[\Delta m^2\cos(2\theta) - 2\sqrt{2}E\, G_F\, n_e(x)\right]^2 + \left[\Delta m^2\sin(2\theta)\right]^2}} . \tag{1.39}$$

Finally, to see the complexity and phenomenological richness implied by the Hamiltonian in Eq. (1.37) it is enough to write the expression that defines the neutrino propagation in the mass basis [3]:

$$\begin{aligned} i\frac{d}{dx}\left[U_M\Phi(x)\right] &= H_F\left[U_M\Phi(x)\right] \\ U_M i\frac{d}{dx}\Phi(x) + i\left[\frac{d}{dx}U_M\right]\Phi(x) &= U_M\left(U_M^\dagger\mathcal{H}U_M\right)\Phi(x) \\ i\frac{d}{dx}\Phi(x) &= \frac{1}{2}\text{diag}\{-|\lambda|/2E, |\lambda|/2E\}\,\Phi(x) - iU_M^\dagger\left[\frac{d}{dx}U_M\right]\Phi(x), \end{aligned}$$

where U_M depends on the mixing angles in matter as it appears in Eq. (1.39). Specifically we have:

$$i\frac{d}{dx}\Phi(x) = \frac{1}{2}\begin{pmatrix} -\frac{|\lambda|}{2E} & -i2\frac{d\theta_M}{dx} \\ i2\frac{d\theta_M}{dx} & \frac{|\lambda|}{2E} \end{pmatrix}\Phi(x) . \tag{1.40}$$

Then, one sees that the Hamiltonian is not diagonal if the matter potential varies with the distance. When the off-diagonal entries are important, and under some conditions, additional

transitions can occur when neutrinos are crossing the resonance region. At this point it is useful to define a parameter that will help us to identify when this level crossing probabilities have to be taken into account. The adiabatic parameter is defined as the diagonal over the off-diagonal entry in the Hamiltonian in the mass basis in Eq. (1.40):

$$\gamma \equiv \frac{|\lambda(x)|}{4E\,|d\theta_M/dx|}, \tag{1.41}$$

and it allows us to introduce two different regimes. In the *adiabatic* regime, characterized by $\gamma \gg 1$, the off-diagonal entries can be neglected. The mixing angle variation $|d\theta_M/dx|$, due to a smooth change in the matter potential, is in this case less important than the magnitude of the wave vector in matter $|\lambda(x)|/4E$. In the *non-adiabatic regimen*, as we will explain later, additional transitions between neutrino mass eigenstates during the resonance can occur.

To solve the amplitude in Eq. (1.40), an initial condition is needed. Assuming that at $x = 0$ only electron neutrinos are produced, which is the case of solar neutrinos, then the probability to detect an arbitrary state is given by:

$$\mathcal{A}_{e\,\alpha} = \langle \nu_\alpha^f | \exp\left(-i\mathcal{H}x\right) | \nu_e^i \rangle \ ,$$

where the indices i and f indicate mixing angles in matter for initial (production point x_i) and final states (detection point x_f), respectively. After a straightforward calculation, the transition probability in the adiabatic regime is expressed as:

$$\begin{aligned} P^{(\gamma\gg1)}_{\nu_e\to\nu_\alpha}(x) &= |\mathcal{A}_{e\,\alpha}|^2 \\ &= \frac{1}{2} - \frac{1}{2}\cos(2\theta_M^i)\cos(2\theta_M^f) - \frac{1}{2}\sin(2\theta_M^i)\sin(2\theta_M^f)\cos\left[\int_0^x dy \frac{|\lambda(y)|}{2E}\right]. \end{aligned} \tag{1.42}$$

The simplest case of constant matter potential is included in Eq.(1.42) as a limiting case. For constant matter potential, $\theta_M^i = \theta_M^f = \theta_M$, the transition probability is given by:

$$P^{Mat}_{\nu_e\to\nu_\alpha}(x) = \sin^2(2\theta_M)\sin^2\left(\frac{|\lambda|}{4E}x\right),$$

which, after averaging over the distance, can be written as:

$$\langle P^{Mat}_{\nu_e\to\nu_\alpha}\rangle_x = \frac{(\Delta m^2)^2 \langle P^{Vac}_{\nu_e\to\nu_a}\rangle_x}{\left[\Delta m^2\cos(2\theta) - 2\sqrt{2}EG_F n_e(x)\right]^2 + \left[\Delta m^2 \sin(2\theta)\right]^2}, \tag{1.43}$$

where Eq. (1.39) has also been used. The average probability in constant matter in Eq. (1.43), in terms of the vacuum probability P^{Vac}, explicitly shows the resonance enhancement of neutrinos when they propagate in matter. This effect is known as MSW effect due to Wolfenstein [12], Mikheyev and Smirnov [13, 14] who first discussed it. This effect is relevant when

neutrinos pass through the resonance region. In this region, when the resonance condition:

$$n_e^R = \frac{\Delta m^2 \cos 2\theta}{2\sqrt{2}\, E\, G_F}. \tag{1.44}$$

is fulfilled, the mixing angle in matter is maximal (complete ν_e conversion into ν_α) even though the mixing angle in vacuum is small.

In the case of the Sun, the matter potential is approximately exponentially decaying with the distance from a dense region in the center to the surface. We can estimate the survival probability (disappearance of electron neutrinos) using Eq. (1.42) as:

$$P^{(\gamma\gg1)}_{\nu_e\to\nu_e}(x) = 1 - P^{(\gamma\gg1)}_{\nu_e\to\nu_\alpha}(x). \tag{1.45}$$

Given the large distance between neutrino production and detection, last oscillatory term averages to zero:

$$\langle P^{(\gamma\gg1)}_{\nu_e\to\nu_e}(x)\rangle_x = \frac{1}{2} + \frac{1}{2}\cos(2\theta^i_M)\cos(2\theta), \tag{1.46}$$

where the mixing angle $\theta^f_M \equiv \theta$ is the vacuum mixing angle for neutrinos that are out of the Sun. The probability expression in Eq. (1.46) depends on the matter potential at the production point through θ^i_M.

When the resonance region is long enough, additional transitions between mass eigenstates in matter can occur. These *non-adiabatic* transitions modify the survival probability in Eq. (1.46). First, we can estimate the change of the electron density during the resonance, δn_e, assuming the condition in Eq. (1.44) is satisfied within the half-width $\Delta m^2 \sin 2\theta$ as [15]:

$$\delta n_e \approx \frac{\Delta m^2 \sin(2\theta)}{2\sqrt{2}\, G_F\, E}$$

which allows us to estimate the resonance range, δx, using $\delta n_e = |dn_e/dx|_R dx$:

$$\delta x \approx \frac{\Delta m^2 \sin(2\theta)}{|dn_e/dx|_R\, 2\sqrt{2}\, G_F\, E} = \frac{\sin(2\theta)}{\cos(2\theta)|d\log n_e/dx|_R}. \tag{1.47}$$

Finally, when δx in Eq. (1.47) is comparable to the oscillation distance, there is a non-zero transition probability between mass eigenstates (level crossing transitions). The expression that takes into account non-adiabatic level crossing transitions during the resonance is the Parke formula [16]:

$$\langle P^{(\gamma\ll1)}_{\nu_e\to\nu_e}(x)\rangle_x = \frac{1}{2} + \left(\frac{1}{2} - P_c\right)\cos(2\theta^i_M)\cos(2\theta), \tag{1.48}$$

where P_c is the level crossing (transition between adiabatic states) probability. In the linear expansion of the potential around the resonance point, P_c can be calculated using the Landau and Zenner formalism [16], and can be written as a function of the adiabatic parameter in the resonance γ_R:

$$P_c = \exp\left[-(\pi\,\gamma_R)/2\right].$$

We note that the probability in Eq. (1.46) is recovered from Eq. (1.48) for the case of no level crossing transitions, i.e, $P_c = 0$.

1.3.4 Three neutrino framework

As mentioned before, it is not always possible to analytically diagonalize the Hamiltonian in Eq. (1.36). Only in the case of constant matter potential it is possible to approximately calculate the oscillation probabilities. This result is useful for neutrinos propagating through the Earth because in some approximation the Earth matter profile can be considered as two slabs of constant density: the mantle and the crust (the core density can not be considered as constant). When the neutrino propagation longitude (baseline) is short enough to cross only the crust, the matter potential can be considered as constant.

Here we present the main results for the oscillation probability functions for the muon appearance and electron disappearance channels. We refer to the interested reader to Ref. [17] for the results for other channels as well as for the detailed technique used to determine these probabilities. The calculation is based on the expansion of the Hamiltonian in matter in Eq. (1.36) around small parameters until some order and its subsequent diagonalization. Here we quote some of the results for the expansion until second order in the small parameters:

$$\begin{aligned} \alpha &\equiv \frac{\Delta m^2_{21}}{\Delta m^2_{31}} \\ s_{13} &\equiv \sin\theta_{13}\ . \end{aligned} \tag{1.49}$$

Later we will see why the parameters in Eq. (1.49) are considered as small quantities.

For later reference, we are particularly interested in the conversion probability for the channel $\nu_\mu \to \nu_e$ and the survival one for the channel $\nu_\mu \to \nu_\mu$. These specific channels correspond to the ones explored at current accelerator based experiments. The expression for ν_e appearance

channel can be obtained from [18]:

$$
\begin{aligned}
P_{e\mu} \approx\; & \alpha^2 \, \sin^2(2\theta_{12}) \, c_{23}^2 \frac{\sin^2(A\Delta)}{A^2} + 4\, s_{13}^2 \, s_{23}^2 \frac{\sin^2[(A-1)\Delta]}{(A-1)^2} \\
& + 2\,\alpha\, s_{13} \, \sin(2\theta_{12}) \, \sin(2\theta_{23}) \cos(\Delta - \delta_{\rm CP}) \, \frac{\sin(A\Delta)}{A} \, \frac{\sin[(A-1)\Delta]}{A-1} \, .
\end{aligned}
\tag{1.50}
$$

for the ν_μ disappearance channel we have:

$$
\begin{aligned}
P_{\mu\mu} \approx\; & 1 - \sin^2(2\theta_{23}) \, \sin^2\Delta + \alpha \, c_{12}^2 \, \sin^2(2\theta_{23}) \, \Delta \, \sin(2\Delta) \\
& - \alpha^2 \, \sin^2(2\theta_{12}) \, c_{23}^2 \, \frac{\sin^2(A\Delta)}{A^2} - \alpha^2 \, c_{12}^4 \, \sin^2(2\theta_{23}) \, \Delta^2 \, \cos(2\Delta) \\
& + \frac{1}{2A} \, \alpha^2 \, \sin^2(2\theta_{12}) \, \sin^2(2\theta_{23}) \left(\sin\Delta \, \frac{\sin(A\Delta)}{A} \, \cos[(A-1)\Delta] - \frac{\Delta}{2} \, \sin(2\Delta) \right) \\
& - 4\, s_{13}^2 \, s_{23}^2 \frac{\sin^2[(A-1)\Delta]}{(A-1)^2} \\
& - \frac{2}{A-1} \, s_{13}^2 \, \sin^2(2\theta_{23}) \left(\sin\Delta \, \cos(A\Delta) \, \frac{\sin[(A-1)\Delta]}{A-1} - \frac{A}{2}\Delta \, \sin(2\Delta) \right) \\
& - 2\,\alpha\, s_{13} \, \sin(2\theta_{12}) \, \sin(2\theta_{23}) \, \cos\delta_{\rm CP} \, \cos\Delta \, \frac{\sin(A\Delta)}{A} \, \frac{\sin[(A-1)\Delta]}{A-1} \\
& + \frac{2}{A-1} \, \alpha \, s_{13} \, \sin(2\theta_{12}) \, \sin(2\theta_{23}) \, \cos(2\theta_{23}) \, \cos\delta_{\rm CP} \, \sin\Delta \\
& \times \left(A \sin\Delta - \frac{\sin(A\Delta)}{A} \, \cos[(A-1)\Delta] \right) \, ,
\end{aligned}
\tag{1.51}
$$

where we have defined:

$$
\begin{aligned}
\Delta &\equiv \frac{\Delta m_{31}^2 L}{4E} \, , \\
A &\equiv \frac{2EV}{\Delta m_{31}^2} = \frac{VL}{2\Delta} \, .
\end{aligned}
\tag{1.52}
$$

To close this subsection we want to make a comment, on the limit for neutrino oscillations in vacuum and on the validity of the approximations considered. The equivalent expressions in vacuum can be obtained from Eq. (1.50) and Eq. (1.51) in the limit $V \to 0$. The authors in Ref. [17] stressed on this point because the eigenvalues are not finite in this limit, although the combination in the amplitude that produces the probabilities ends in well behaved expressions in the vacuum limit. The accuracy of the expressions is also discussed on the original reference comparing with the numerical exact solution of the Hamiltonian. Basically, since we are working in the limit when $\alpha \ll 1$ this is also valid for:

$$
\frac{\Delta m_{21}^2 L}{4E} \ll \frac{\Delta m_{31}^2 L}{4E} \, ,
$$

which implies that oscillations driven by Δm_{21}^2 should not be relevant.

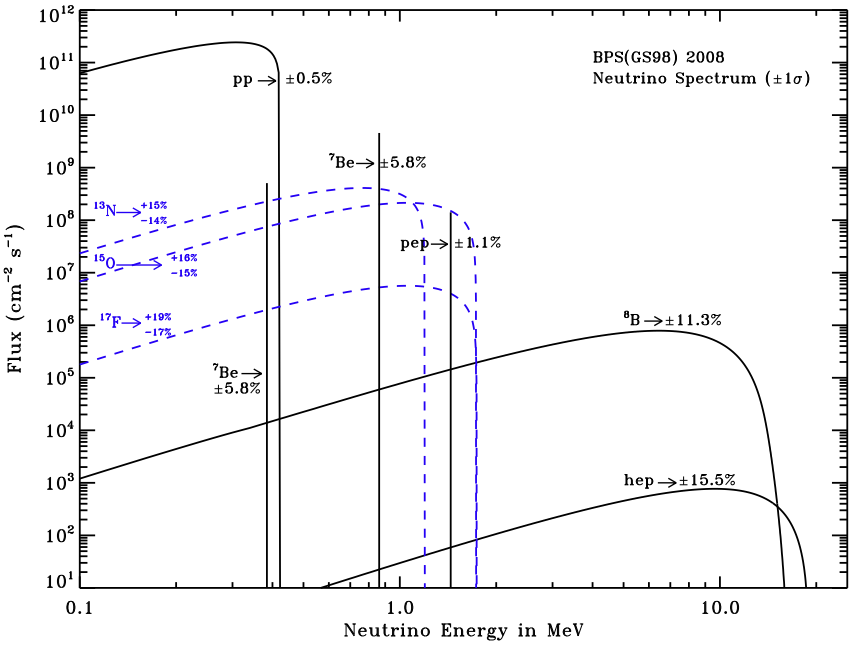

Figure 1.1: Calculated neutrino fluxes from BPS08 standard solar model (SSM). Figure taken from http://www.mpa-garching.mpg.de/~aldos/.

1.4 Solar and atmospheric neutrinos

1.4.1 Solar neutrinos

Neutrinos coming from the Sun are generated as a product of several thermonuclear processes mainly through the proton-proton (pp) chain and the CNO cycle. In terms of the source reaction, the pp chain processes are: pp, pep, hep, ^{7}Be and ^{8}B while in the CNO cycle the three relevant processes are known as: ^{13}N, ^{15}O and ^{17}F. For a better understanding of the sources and number of neutrinos generated in the Sun, Fig. 1.1 shows the predicted neutrino fluxes from the processes we have mentioned so far. The final result is the fusion of four protons into one nucleus of ^{4}He:

$$4p \rightarrow {}^{4}\text{He} + 2e^{+} + 2\nu_e + \gamma$$

releasing an energy of $Q = 4m_p - m_{^4\text{He}} - 2m_e \simeq 26\,\text{MeV}$, mainly radiated through photons and a small fraction by neutrinos $\langle E_{2\nu_e} \rangle = 0.59\,\text{MeV}$ [19].

Historically, the interest to detect solar neutrinos started in the sixties with experiments using specific chemical reactions known as radiochemical neutrino experiments. Another kind of neutrino detector technology is based on the detection of the Cherenkov light emitted by a

Experiment	Detection process	E-Threshold.	Sensitivity to
Homestake (Chlorine)	$\nu_e + {}^{37}Cl \rightarrow {}^{37}Ar + e^-$ (CC)	814 keV	all but pp and one ^{7}Be line
GALLEX, GNO	$\nu_e + {}^{71}$Ga $\rightarrow {}^{71}$Ge $+ e^-$ (CC)	233 keV	all
SAGE	$\nu_e + {}^{71}$Ga $\rightarrow {}^{71}$Ge $+ e^-$ (CC)	233 keV	all
(Super)Kamiokande	$\nu_e + e^- \rightarrow \nu_e + e^-$ (ES)	(3.5) 5.0 MeV	^{8}B+hep
SNO	$\nu_e + d \rightarrow p + p + e^-$ (CC)	5 MeV	^{8}B+hep
	$\nu_x + d \rightarrow p + n + \nu_x$ (NC)	5 MeV	^{8}B+hep
	$\nu_x + e^- \rightarrow \nu_x + e^-$ (ES)	5 MeV	^{8}B+hep
Borexino	$\nu_e + e^- \rightarrow \nu_e + e^-$ (ES)	250 keV	^{7}Be and pep
		3 MeV	^{8}B

Table 1.1: Solar neutrino experiments with the corresponding detection process, detection energy threshold and the part of neutrino flux they can observe.

charged particle traveling faster than light in a medium, which gave origin to the Cherenkov neutrino experiments. The leaders of the two pioneer neutrino experiments using these techniques, Raymond Davis and Masatoshi Koshiba were awarded with the 2002 Nobel Prize in Physics.

The energy threshold of a given detection process defines the portion of solar neutrino fluxes that can be observed. Table 1.1 provides a list of all solar neutrino experiments together with the detection process used, the corresponding energy threshold and the respective flux that can be detected. Cherenkov experiments such as `Super Kamiokande (SK)` and `SNO` are *real-time experiments*, meaning that they can determine the neutrino energy, direction and detection time event by event. This allows a more complete evidence about the origin and time variation of neutrino events, such as the day and night variation in the solar neutrino fluxes. They provide spectral and zenith angle information, richer than the total rate given by the radiochemical experiments. Up to date `SK` and `SNO` have reported several results in different phases. In particular the three phases of `SNO`, according to the detection techniques used for NC events, are known as: heavy water, salt and ^{3}He, respectively. Since we cannot describe all experiments and measurements exhaustively, here we will describe just the results from the 391 live days salt phase of the `SNO` experiment [20] that allow us to determine the *neutrino flavor conversion*. For a general review of solar neutrino experiments and measurements see

Refs. [5, 19] and references therein. The SNO measured fluxes, in units of $10^6\ \mathrm{cm}^{-2}\mathrm{s}^{-1}$, are [20]

$$\begin{aligned}
\phi_{\mathsf{CC}} &= 1.68^{+0.06}_{-0.06}(\mathsf{stat})^{+0.08}_{-0.09}(\mathsf{syst})\ , \\
\phi_{\mathsf{ES}} &= 2.35^{+0.22}_{-0.22}(\mathsf{stat})^{+0.15}_{-0.15}(\mathsf{syst})\ , \\
\phi_{\mathsf{NC}} &= 4.94^{+0.21}_{-0.21}(\mathsf{stat})^{+0.38}_{-0.34}(\mathsf{syst})\ ,
\end{aligned} \tag{1.53}$$

and the ratios of the CC flux to NC and ES respectively are

$$\begin{aligned}
\frac{\phi_{\mathsf{CC}}}{\phi_{\mathsf{NC}}} &= 0.340 \pm 0.023\ (\mathsf{stat})\ ^{+0.029}_{-0.031}\ (\mathsf{syst})\ , \\
\frac{\phi_{\mathsf{CC}}}{\phi_{\mathsf{ES}}} &= 0.712 \pm 0.075\ (\mathsf{stat})\ ^{+0.045}_{-0.044}\ (\mathsf{syst}).
\end{aligned} \tag{1.54}$$

Taking into account the processes in table 1.1, the neutrino flavor content detected at SNO is given by:

$$\begin{aligned}
\phi_{\mathsf{CC}} &= \phi_e\ , \\
\phi_{\mathsf{ES}} &= \phi_e + r\,\phi_{\mu,\tau}\ , \\
\phi_{\mathsf{NC}} &= \phi_e + \phi_{\mu,\tau}\ ,
\end{aligned} \tag{1.55}$$

where r is the ES cross section rate $\sigma_\mu/\sigma_e = 0.1553$ [19, 20]. From the first and last relation in Eq. (1.55) the flux $\phi_{\mu,\tau}$ is determined to be [20]:

$$\phi^{\mathsf{NC}}_{\mu\tau} = 3.26 \pm 0.25\ (\mathsf{stat})\ ^{+0.40}_{-0.35}\ (\mathsf{syst})\ , \tag{1.56}$$

which in the SSM is expected to be equal to zero (only electron neutrinos are produced in the Sun), implying the evidence of a *neutrino flavor transition*. The plot in Fig. 1.2 represents the measured fluxes in Eq. (1.53) as a function of the flavor content in Eq. (1.55). The measurement of the NC flux, that is equally sensitive to all active neutrinos, allowed SNO to determine the electron neutrino deficit through the ratio $\Phi_{\mathsf{CC}}/\Phi_{\mathsf{NC}}$ in Eq. (1.54) independently of the SSM. The dashed lines in Fig. 1.2 also show the prediction for total neutrino flux from the SSM and we see it is compatible with the $\phi_{\mu,\tau}$ measurement implying that the SSM prediction for the ϕ_e in the production is correct. However, in the detection, the electron neutrinos appeared redistributed in the three flavors as indicated by the first relation in Eq. (1.54).

Nowadays we know neutrino oscillation is the dominant mechanism to explain the flavor conversion of solar neutrinos. In this context, when solar neutrinos arrive at the Earth, before being detected, they can additionally interact with the terrestrial matter in a resonant way, as

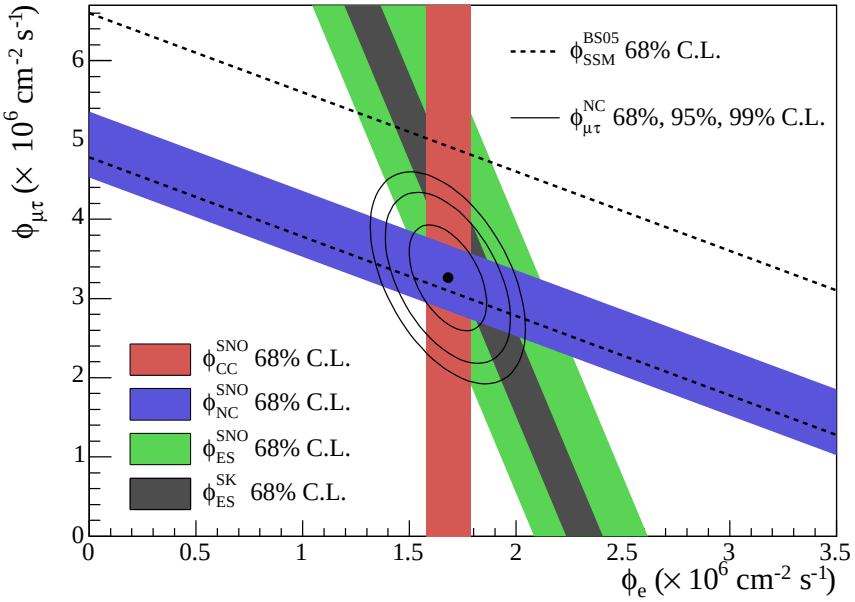

Figure 1.2: SNO measured fluxes for each of the processes CC, NC and ES, represented as bands. Dashed lines represent the SSM [21] expectation. The point corresponds to the observed value $(\phi_e, \phi_{\mu\tau})$. Figure taken from [20].

explained in Sec. 1.3.3. This effect is called ν_e *regeneration inside the Earth*. If it is the case, this effect can be noticed by a difference between the neutrino fluxes measured in the night compared to the ones measured during the day, due to the Earth matter effect. The *day-night asymmetry (A)* is defined as:

$$A \equiv 2(\phi_N - \phi_D)/(\phi_N + \phi_D) \ , \tag{1.57}$$

where the day and night fluxes ϕ_D and ϕ_N are measured for each reaction. This is one of the advantages of real-time experiments. The last experimental value for the asymmetry has been measured by the SK collaboration [22]:

$$A = -3.2 \pm 1.1(\text{stat.}) \pm 0.5(\text{sys.}),$$

showing a 2.7σ deviation from zero. This result implies a *regeneration of electron neutrinos* as a result of interactions between neutrinos and terrestrial matter.

Going back to SNO results, assuming neutrino oscillations, the allowed region for the mixing angle and the solar splitting, are determined from the fit to the observables: CC spectra, NC and ES integrated fluxes, separately for day and night allowing to include the day-night asymmetry information [20]. The parameter region allowed only by SNO data spans three orders

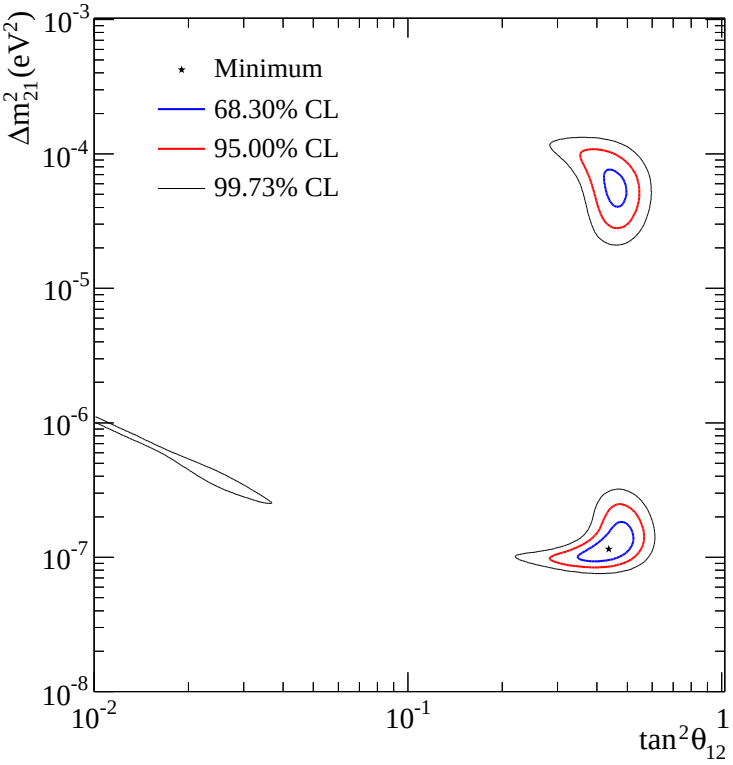

Figure 1.3: Allowed region of oscillation parameters from the SNO collaboration in the two neutrino framework, see the original Ref. [23] for details of the analysis.

of magnitude in the solar mass splitting, as it is shown in Fig. 1.3. After the combination with other solar neutrino experiments, and specially with the KamLAND reactor experiment, the solar neutrino parameters are well determined and the unique valid solution is the region known as *Large Mixing Angle (LMA)*.

1.4.2 Atmospheric neutrinos

When cosmic rays interact in the Earth atmosphere, mesons are produced, mainly pions and some kaons, which will decay into neutrinos. Atmospheric neutrinos are then mainly produced by the chain:

$$\begin{aligned} \pi^+(\pi^-) \rightarrow & \mu^+(\mu^-) + \nu_\mu(\bar{\nu}_\mu) \\ & \mu^+(\mu^-) \rightarrow e^+(e^-) + \nu_e(\bar{\nu}_e) + \bar{\nu}_\mu(\nu_\mu) \ . \end{aligned} \tag{1.58}$$

If all the muons decay, we can expect twice more muon neutrinos plus antineutrinos than electron neutrinos plus antineutrinos. In terms of flux it means:

$$\phi(\nu_\mu + \bar{\nu}_\mu) \approx 2\phi(\nu_e + \bar{\nu}_e). \tag{1.59}$$

The flux from the muons that do not decay (for energies above a few GeV neutrino energy), before reaching the Earth surface, can also be estimated and the rate $\phi(\nu_\mu + \bar{\nu}_\mu)/\phi(\nu_e + \bar{\nu}_e)$ can be calculated accurately [24], however, Eq. (1.59) in not valid in this case.
Another relation between the neutrino fluxes is provided by the decay chain in Eq. (1.58), in particular:

$$\phi(\nu_\mu) \approx \phi(\bar{\nu}_\mu),$$

and also the same relation is expected for electron neutrinos, due to correlations between μ^+/μ^- that can also be measured. The key point is that ratios of neutrino fluxes can be calculated within some accuracy depending on the energy range. In the energy region below 10 GeV, muon neutrinos are produced by pion decays and their ratio of fluxes from Eq. (1.59) has an uncertainty of less than 4% [24]. The comparison between different flux calculations is shown in Fig. 1.4.

Assuming the cosmic ray flux is isotropic and the Earth is spherically symmetric, it is expected that, without oscillations, the neutrino fluxes are approximately up-down symmetric [24]:

$$\phi_{\nu_\alpha}(E, \cos\Theta) \approx \phi_{\nu_\alpha}(E, -\cos\Theta) \ , \tag{1.60}$$

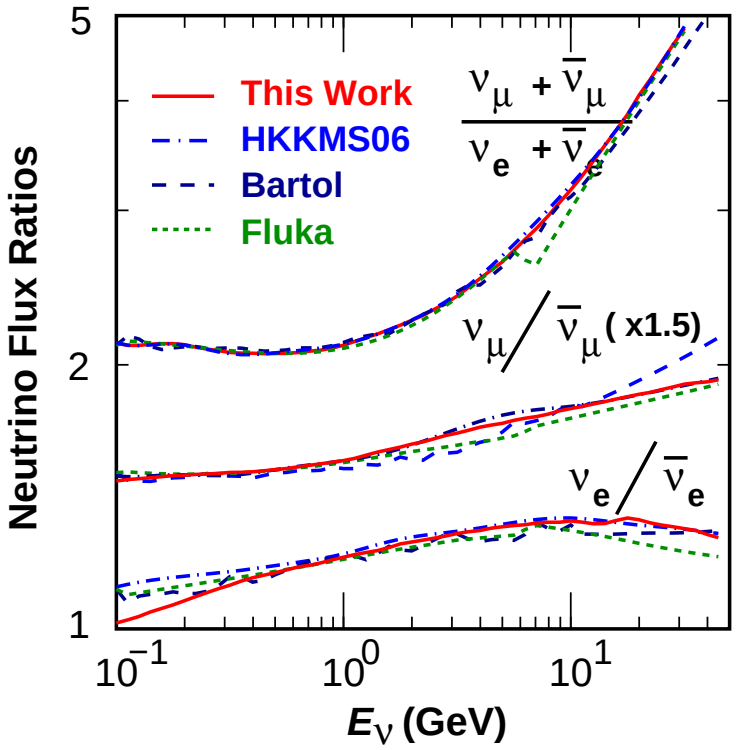

Figure 1.4: Calculated neutrino flux rates. Comparison between different flux calculations [25].

where Θ is the zenith angle of the neutrino direction. This relation however, is not exact due to geo-magnetic effects that affect low energy neutrinos ($E_\nu < 1\,\text{GeV}$) [24]. In Fig. 1.5 it is shown the zenith angle dependence of the atmospheric neutrino flux for different neutrino energies. We can see the up-down symmetry is fulfilled for neutrino energies above $1\,\text{GeV}$.

Historically, the Kamiokande experiment played a big role in the understanding of the atmospheric neutrino deficit discussed below (see Fig. 1.6). It measured atmospheric neutrinos through the light ring produced by the Cherenkov radiation of the charged particle in the water detector, to tag the charged leptons generated in the neutrino interaction with the nucleons in the detector. In the late eighties the Kamiokande collaboration found a deficit of muon neutrinos while a compatible number of electron neutrinos, compared to the theoretical expectations. Without any confirmation from other experiments, the absence of neutrinos was known as the *atmospheric neutrino problem*.

Concerning the flux property described in Eq. (1.60) and Fig. 1.5, also non conclusive studies of the up-down symmetry were carried out in the nineties due to the few statistics.

An experimental upgrade of Kamiokande, increasing the detector size from $3\,\text{kton}$ to $50\,\text{kton}$,

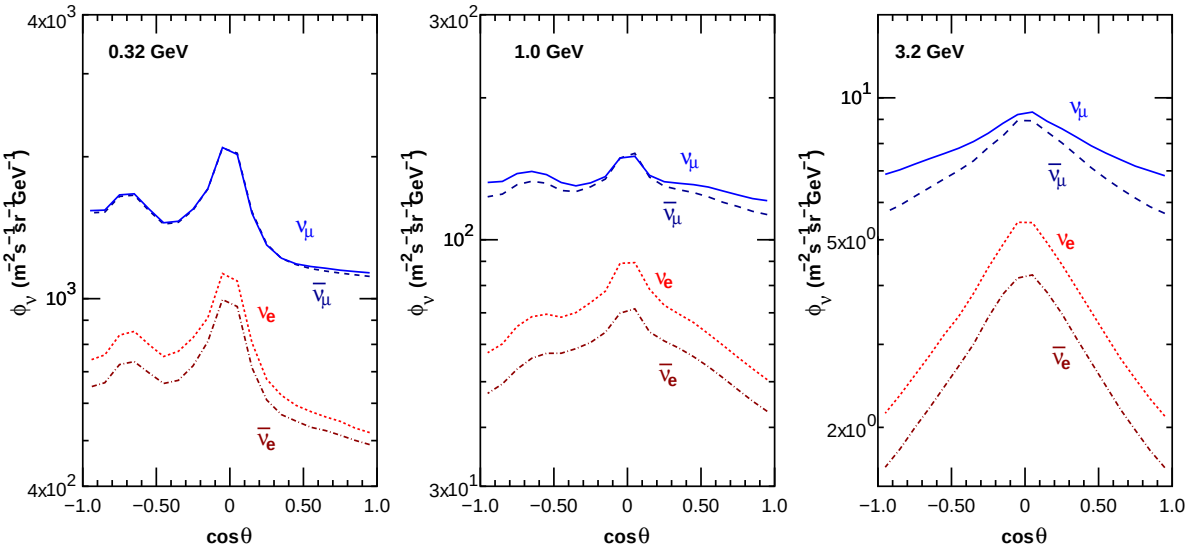

Figure 1.5: Zenith angle dependence of the atmospheric neutrino fluxes averaged over all azimuthal angles calculated for the Kamioka site [25].

gave birth to SK, still running. Because atmospheric neutrino spectrum spans five decades in energy, the observed atmospheric neutrinos in SK are classified as [26]:

- **Fully/partially contained**: At low energies ($100\,\text{MeV} - 10^2\,\text{GeV}$) neutrinos interact via Charged Current (CC) with the inner detector (ID) nucleons. These interactions are *fully-contained* (FC) or *partially contained* (PC) if the muon deposits all the energy in the ID or if the muon deposits the energy in the Outer Detector (or Veto), respectively.

- **Upward going/stopping**: More energetic muons ($E \geq 2\,\text{GeV}$) interact via CC with the rock surrounding the detector. Muons traveling in the upward direction ($\cos\theta < 0$) are a clear signal of ν_μ's. If the muons (cross) stop in the detector those events are classified as (*upward through-going*) *upward stopping* events.

Back into the discussion of the *muon neutrino deficit*, a sample of the latest results of atmospheric neutrino events is shown in Fig. 1.6. When comparing with what is expected from Eq. (1.59) and Eq. (1.60), it is clear that muon neutrinos are disappearing. The disappearance effect strongly depends on the zenith angle and it is more evident for the upward going neutrinos ($\cos\Theta < 0$), since it is correlated with the neutrino flight distance. Data show a zenith asymmetry contrary to the theoretical expectations without oscillations in the gray dashed line in Fig. 1.6. Also in the left panel of Fig. 1.6 the electron neutrino events are shown. These

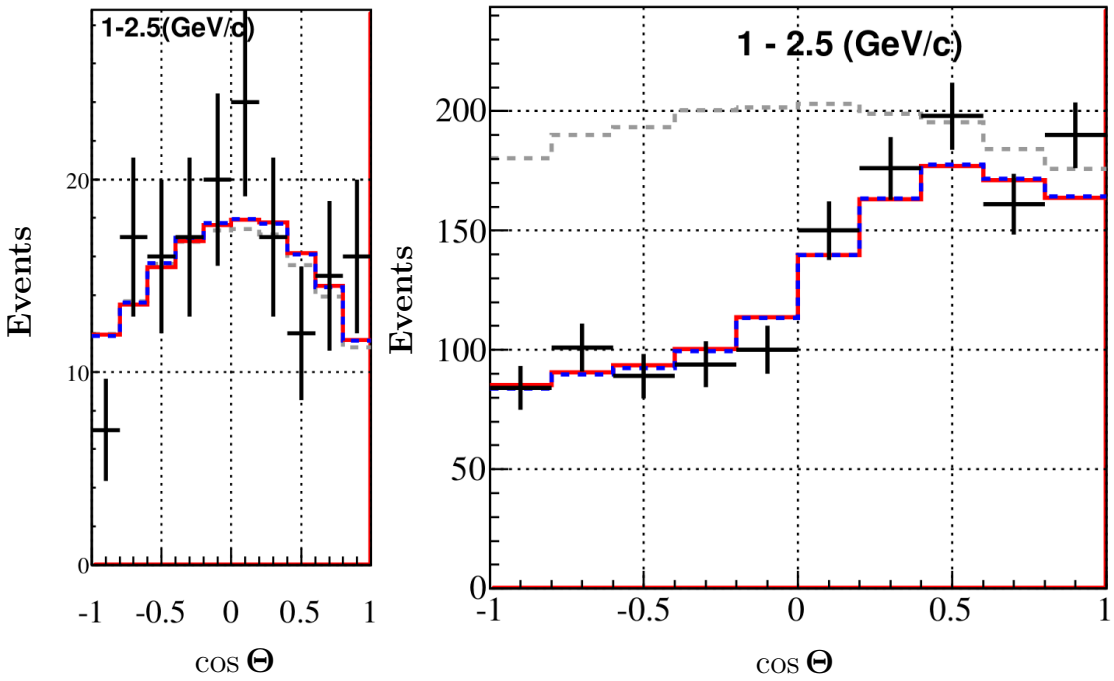

Figure 1.6: Multi-GeV 1-ring SK data set for SK-I to SK-IV zenith angle distributions for FC events for data (line with error bar) and MC assuming no oscillation (gray dashed line), best fit results at normal hierarchy (red solid line) and best fit results at inverted hierarchy (blue dashed line). Left panel e-like events. Right panel μ-like events. [27].

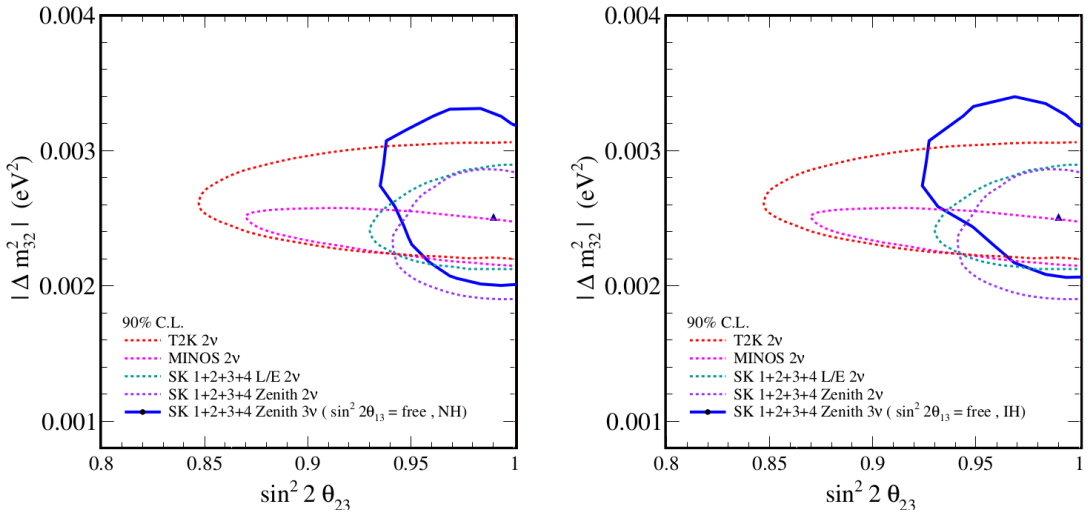

Figure 1.7: Allowed parameter region from the analysis of SK data. Other experiments are included for comparison. Left(Right) panel corresponds to the NH (IH). Figure taken from Ref. [27].

events, however, are symmetric and compatible with the theoretical expectations. Thus, we can conclude that the muon neutrinos are not converting into electron neutrinos.

Neutrino oscillations successfully explain the muon neutrino deficit. The dependence with the zenith angle is related with the neutrino baseline: downward going muon neutrinos travel $\sim 20\,$km while upward going muon neutrinos travel $\sim 13000\,$km (nearly the Earth diameter). In order to estimate the neutrino oscillation parameters from the current data, many experimental details have to be taken into account, as for instance, systematic errors. There are several sources of systematic errors. Just to mention a few: the uncertainty on the flux determination, at least 5% error in the low energy part as deviation among several calculations. Detector systematic errors include the interaction model as well. Due to the wide energy range, several non-quasielastic processes contribute to the number of events but their cross sections are known only in an approximate way. Another set of systematic uncertainties comes from the event reconstruction and event selection. For a detailed description see Ref. [27].

After the inclusion of the systematic errors and fitting the latest data [27] to the model with oscillations, Fig. 1.7 shows the allowed region in the $\Delta m^2_{32} - \sin^2 2\theta$ plane. Finally, to show that neutrino oscillations $\nu_\mu \to \nu_\tau$ indeed describe the data, SK has measured the neutrino oscillation pattern. In Fig. 1.8 the ratio of the observed over expected events without oscillations as a function of the neutrino baseline and energy, L/E, is shown. Thanks to the observation

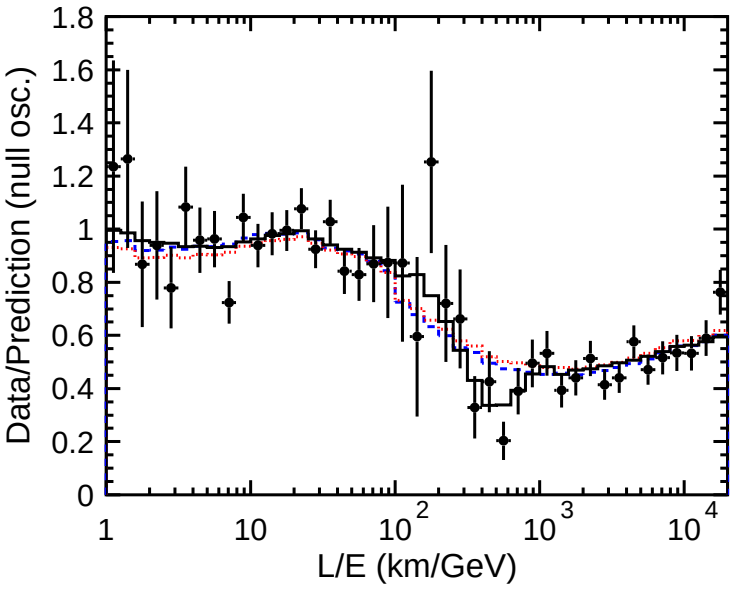

Figure 1.8: Ratio of the data to the MC events without neutrino oscillation (points) as a function of the reconstructed L/E together with the best-fit expectation for 2-flavor $\nu_\mu \to \nu_\tau$ oscillations (solid line). The error bars are statistical only. The best-fit expectation for neutrino decay (dashed line) and neutrino decoherence (dotted line) are also shown [28].

of the oscillation dip, the measurement of the oscillation parameters is accurate, especially for the mass splitting Δm^2_{32} [24].

1.5 Reactor experiments

1.5.1 Reactor event calculation

Reactor antineutrinos are produced by the fission of the isotopes ^{235}U, ^{239}Pu, ^{241}Pu and ^{238}U. Each fissile isotope contributes to the total reactor neutrino flux and fuel content with a certain fission fraction f_k that can be calculated through a detailed simulation of the core evolution. Reactor antineutrinos are detected via inverse β-decay process (IBD), $\bar{\nu}_e + p \to e^+ + n$. The experimental technique used is a delay coincidence between two signals: one coming from the positron annihilation (*prompt* signal) and other coming from the neutron capture in the innermost part of the antineutrino detector (AD), containing gadolinium-doped liquid scintillator. The light created is collected by the photo-multipliers (PMTs) located in the outermost mineral oil-region. The anti-neutrino energy $E_{\bar{\nu}}$ is reconstructed from the positron prompt

energy E_{prompt} following the relation: $E_{\bar{\nu}} = E_{\text{prompt}} + \bar{E}_n + 0.78\,\text{MeV}$, where the $\bar{E}_n$ is the average neutron recoil energy.

For a general reactor experiment, with arbitrary number of detectors and reactors, the expected number of IBD events at the d-th detector coming from a given reactor r-th, without oscillations, can be estimated from:

$$N_{rd} \;=\; \epsilon_d \frac{N_p}{4\pi L_{rd}^2} \frac{P_{th}^r}{\sum_k f_k \langle E_k \rangle} \sum_k f_k \int_0^\infty dE\, \Phi_k(E)\, \sigma_{IBD}(E)\ , \tag{1.61}$$

where N_p is the number of protons in the target volume, P_{th}^r is the reactor thermal power, ϵ_d denotes the efficiency of the detector and $\langle E_k \rangle$ is the energy release per fission for a given isotope k, taken from Ref. [29]. L_{rd} is the distance from reactor r-th to detector d-th. For the antineutrino flux prediction $\Phi_k(E)$ the more recent parametrizations available in the literature are in Ref. [30] and Ref. [31]. We used the second one as well as the new normalization for reactor antineutrino fluxes updated in Ref. [32]. The inverse beta decay cross section $\sigma_{\text{IBD}}(E_\nu)$ is taken from Ref. [33]. To account for the deficit of antineutrinos at the far detector and the distortion of the reactor $\bar{\nu}_e$ spectrum, the oscillation probability $P(E_\nu, L_{rd})$ is included in the theoretical estimate of the number of events. In order to minimize the dependence upon the predicted normalization of the antineutrino spectrum, we take the ratio of far oscillating events T_{rd} over the total far expected events $\sum_r N_{rd}$. Thus, we have:

$$\frac{T_{rd}}{\sum_r N_{rd}} = \omega_r^d \frac{\sum_k f_k \int_0^\infty dE_\nu\, \Phi_k(E_\nu)\, \sigma_{IBD}(E_\nu) P(E_\nu, L_{rd})}{\sum_k f_k \int_0^\infty dE_\nu\, \Phi_k(E_\nu)\, \sigma_{IBD}(E_\nu)} \equiv \omega_r^d \langle P(E_\nu, L_{rd}) \rangle\ , \tag{1.62}$$

where ω_r^d is the fraction of IBD contribution of the r-th reactor to the d-th AD determined from the baselines and reactor thermal powers:

$$\omega_r^d \equiv \frac{w_r / L_{rd}^2}{\sum_r w_r / L_{rd}^2} \quad \text{with} \quad w_r = P_{th}^r / \sum_r P_{th}^r\ . \tag{1.63}$$

Finally, we can estimate the observed number of events in the d-th detector from the expected events using Eq. (1.62) in a straightforward way [34]:

$$T_d = N_d \sum_r \omega_r^d \langle P(E_\nu, L_{rd}) \rangle\ . \tag{1.64}$$

This way, our statistical analysis is free of correlations among the different reactor data samples, since the relative measurements do not rely on reactor flux predictions.

1.5.2 Daya Bay as an example

Daya Bay is a reactor neutrino experiment with six ADs, arranged in three experimental halls (EHs). Two ADs are located in EH1, one in EH2 and three in EH3. EH1 and EH2 are considered as near halls while EH3 is the far hall. Electron antineutrinos are generated in six reactor cores, distributed in pairs, with equal thermal power ($P^r_{th} = 2.9\,GW_{th}$) and detected in the EHs. The effective baselines are $512\,$m and $561\,$m for the near halls and $1579\,$m for the far one [35]. At those distances ($\sim$ km), Daya Bay is sensitive to the first dip in the $\bar{\nu}_e$ disappearance probability. With this near-far technology Daya Bay has minimized the systematic errors coming from the ADs providing the most precise determination of the reactor mixing angle so far.

In their last article in Ref. [35], Daya Bay analyzed 217 days of data represented by the observed rates and energy spectra in each AD. Compared to the previous analysis in Ref. [36], there has been an improvement in the statistical errors (due to the increase of data) but not in the systematical uncertainties (already very good in their first analysis). The new analysis is independent of the previous one and the data set used in the determination of the oscillation parameters now includes the spectral information. Basically, three analyses were done: rate only, spectral only and the combination.

We will follow the analysis of the previous Daya Bay paper in Ref. [36] with the latest data in Ref. [35]. Our analysis is based on nuisance-parameter χ^2, with the definition:

$$\begin{aligned}\chi^2 &= \sum_{d=1}^{6} \frac{\left[M_d - T_d\left(1 + a + \sum_r \omega_r^d \alpha_r + \xi_d\right) + \beta_d\right]^2}{M_d + B_d} \\ &+ \sum_{r=1}^{6} \frac{\alpha_r^2}{\sigma_r^2} + \sum_{d=1}^{6}\left(\frac{\xi_d^2}{\sigma_d^2} + \frac{\beta_d^2}{\sigma_B^2}\right) ,\end{aligned} \tag{1.65}$$

where T_d is the theoretical prediction for the expected events in Eq. (1.64) and M_d are the measured events at the d-th AD with its backgrounds (B_d) subtracted. The pull parameters, used to include the systematical errors in the analysis, are given by the set $(\alpha_r, \xi_d, \beta_d)$ representing the reactor, detector and background uncertainties with their corresponding set of errors $(\sigma_r, \sigma_d, \sigma_B)$. Uncertainties in the reactor related quantities are included in σ_r (0.8%) while the uncorrelated combined uncertainties in the ADs are included in σ_d (0.2%). σ_B is the quadratic sum of the background uncertainties taken from Ref. [36]. Finally, the absolute normalization factor a is left *free* to be fitted by the data.

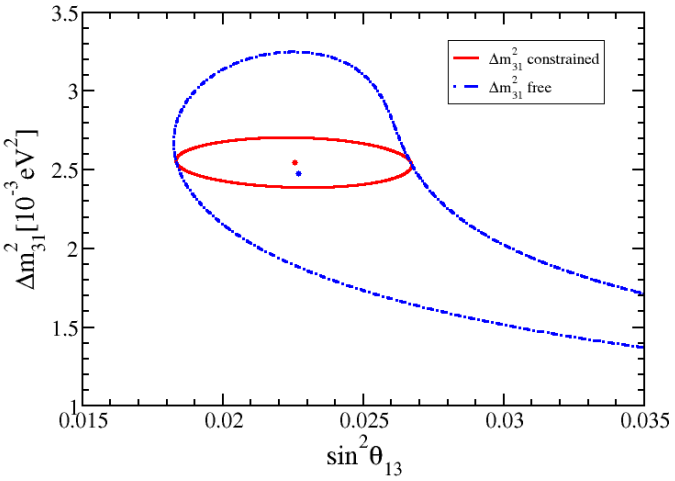

Figure 1.9: Daya Bay allowed regions at 90% of C.L from the rate-only analysis. Not shown parameters are kept fixed to their best fit values from [1]. We have constrained the atmospheric splitting to be within its 1σ error, obtaining a best fit value of $\sin^2\theta_{13} = 0.0226$. A 'free' variation of the atmospheric splitting is shown in blue (dot dashed line).

Using the χ^2 in Eq. (1.65), we obtained the allowed parameter region in Fig. 1.9. The Daya Bay collaboration has performed an spectral data analysis determining the atmospheric mass splitting [35], which is compatible with the MINOS result. In Fig. 1.9 we constrained the atmospheric splitting to be within the 1σ error $\delta(\Delta m^2_{31}) = 0.075 \times 10^{-3}\,\text{eV}^2$ obtaining a best fit value of $\sin^2\theta_{13} = 0.0226$. A 'free' variation of the atmospheric mass splitting produces a value $\sin^2\theta_{13} = 0.0227$, showing the stability over the mass splitting variation. Fixing all neutrino oscillation parameters to their best fit values in Ref. [1], we found the best fit value for the reactor mixing angle in this rate-only analysis:

$$\sin^2\theta_{13} = 0.0226^{+0.0041}_{-0.0039}\ . \tag{1.66}$$

1.6 Accelerator experiments

All neutrino experiments can be considered as a three stage process: production, propagation and detection. Neutrino production in these experiments consists of an *accelerator complex* that provides the neutrinos as decay products of pions and kaons generated from the collision of high-energy protons on a nucleus target. In the first beam line, where pions and kaons are

produced, magnetic horns are used to focus the beam. In the second phase, pions and kaons decay in a volume sometimes filled with gas. Finally, hadrons are stopped or absorbed leaving only neutrinos and sometimes muons that are monitored. A muon (anti) neutrino beam is selected by focusing (negative) positive pions and kaons.

At this point, neutrinos are produced in the same way as atmospheric neutrinos, with the advantage that the neutrino spectrum can be controlled by varying the distance between the target and the focusing horns. Before finishing the production stage, in the *near detector complex* the neutrino beam is characterized. At this phase various measurements are done in order to fit several parameters related to the neutrino flux and cross section. Together with external measurements in the case of the cross section, systematic errors in the far detector measurements will be reduced by the use of the near detector information.

In the second stage, neutrinos propagate several hundreds of kilometers from the source to the *far detector*. Given the distance traveled by the neutrino, neutrino interactions with the Earth matter should be taken into account. A good approximation, the matter potential can be considered constant with the electron density in the Earth crust.

In the last stage, neutrinos are detected in the far detector (FD). The far detector is composed of at least an inner (ID) and an outer detector (OD), which is helpful to reject background events. The neutrino flux is measured in the far detector in order to quantify spectral differences in the FD due to neutrino flavor transformation compared with the expected spectrum via Montecarlo (MC) simulation of the experiment tuned with the near detector information and calibration measurements. When the FD is not a copy of the near detector, new systematic errors will appear that will not totally cancel with the use of the near detector information.

As we mentioned before, the analysis of this kind of experiments consists of a comparison between the far spectrum measurements and the expected spectrum by MC simulation. In order to reconcile the data with the expectations in the FD, the flavor transitions are explained by neutrino oscillations and the parameters in the oscillation mechanism are constrained by the data. Due to the energies involved, in the range of few GeV, and for baselines of a hundred kilometers, accelerator neutrino experiments are sensitive to the atmospheric neutrino oscillation parameters. In fact, accelerator-based neutrino neutrino experiments were designed to be complementary to the atmospheric experiments. Currently, the atmospheric mass splitting and mixing angle are well measured by `MINOS` and `T2K`, respectively. Accelerator-based exper-

	T2K	MINOS $\nu(\bar{\nu})$-mode
Beam source	J-PARC	FERMILAB
POT	6.57×10^{20}	$10.6 \times 10^{20}(3.3 \times 10^{20})$
ND technology	Grid detector+magnetized+TPC+Ecal	Magnetized tracker calorimeters
Peak energy	0.6 GeV	3 GeV
FD location	Kamioka	Soudan Mine (Minessota)
Baseline	295 km	735 km
FD technology	water Cherenkov	Magnetized tracker calorimeters
Fiducial Volume	22.5 ktons	3.8 ktons
Events ν_e app.	28	152(20)
MC Expected	21.6	$33.7 \pm 1.9(3.9 \pm 0.2)$
With osc.	$\sin^2 2\theta_{13} = 0.1$, $\delta_{CP} = 0$ and $\theta_{23} = \pi/4$	
best fit value	$\sin^2 2\theta_{13}$	$2\sin^2(2\theta_{13})\sin^2(\theta_{23})$
NH [IH]	$0.140^{+0.038}_{-0.032}[0.170^{+0.045}_{-0.037}]$	$0.051^{+0.038}_{-0.030}[0.093^{+0.054}_{-0.049}]$
Events ν_μ disapp.	120	2579(312)
MC Expected	446.0 ± 22.5(sys.)	3201(363)
No osc.		
best fit value	$\sin^2\theta_{23}$	$\sin^2 2\theta$ '2ν'
NH [IH]	$0.514^{+0.055}_{-0.056}[0.511 \pm 0.055]$	$0.950^{+0.035}_{-0.036}(0.97^{+0.03}_{-0.08})$
best fit value	$\Delta m^2_{32}[\Delta m^2_{13}] \times 10^{-3}\, eV^2$	$\lvert\Delta m^2\rvert$ '2ν'
NH [IH]	$2.51 \pm 0.10[2.48 \pm 0.10]$	$2.41^{+0.09}_{-0.10}$ $(2.50^{+0.23}_{-0.25})$

Table 1.2: Comparison of the general aspects of T2K [37, 38] and MINOS [39, 40].

iments are not only expected to be complementary to atmospheric experiments but also to provide information about the unknown CP phase and the neutrino mass hierarchy.
angle.
In order to introduce the details on the current accelerator neutrino experiments, in table 1.2 we present some generalities about T2K and MINOS.

1.6.1 T2K as an example

Before the measurement of the reactor mixing angle, the first indication for a non-zero θ_{13} was provided by T2K. This experiment is sensitive not only to the reactor mixing angle but also to the CP phase δ_{CP} through the ν_e appearance channel. The other channel, ν_μ disappearance,

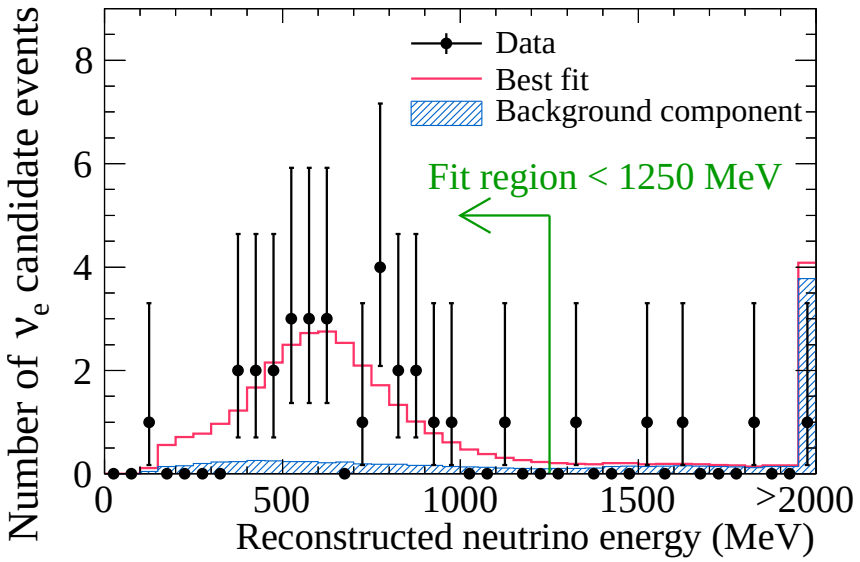

Figure 1.10: Energy spectrum for ν_e events in T2K. Best fit histogram for $\sin^2 2\theta_{13} = 0.144$ and NH [37].

as we said before, is sensitive to the atmospheric parameters. Here as an example we will show how to fit the last T2K results for the ν_e appearance [37].

The neutrino energy, reconstructed from the observed electron energy, for the ν_e events (or the event spectrum) is shown in Fig. 1.10. We calibrate our simulation to the best fit histogram and finally we fit the data allowing a variation of the relevant neutrino oscillation parameters. In order to include information about the systematic errors, we use the pull method and the following definition of the χ^2 function:

$$\chi^2(\vec{\lambda}) = \min_{\{a\}} \left\{ \sum_{i=1}^{n_{bins}} 2 \left[O_i - T_i(1+a) + O_i \log \frac{O_i}{T_i(1+a)} \right] + \left(\frac{a}{\sigma_a} \right)^2 \right\} , \qquad (1.67)$$

where O_i and T_i are the measured and the theoretical expected events for the i-th bin, respectively. The parameter a accounts for the systematic error in the flux normalization and also other systematic errors that affect the global normalization in the event calculation. After the minimization over the nuisance parameters (in our case only the a parameter) we end up with a χ^2 function that depends on the vector of the oscillation parameters $\vec{\lambda}$. In order to calculate the theoretical events T_i we need additional information from table 1.2 as well as the flux, cross section and probability expression for the channel of interest. We take the fluxes from the T2K collaboration paper [38] and use the GLoBES package [41, 42] with its cross section values for the simulation. The probability expression encoded in GLoBES is the exact

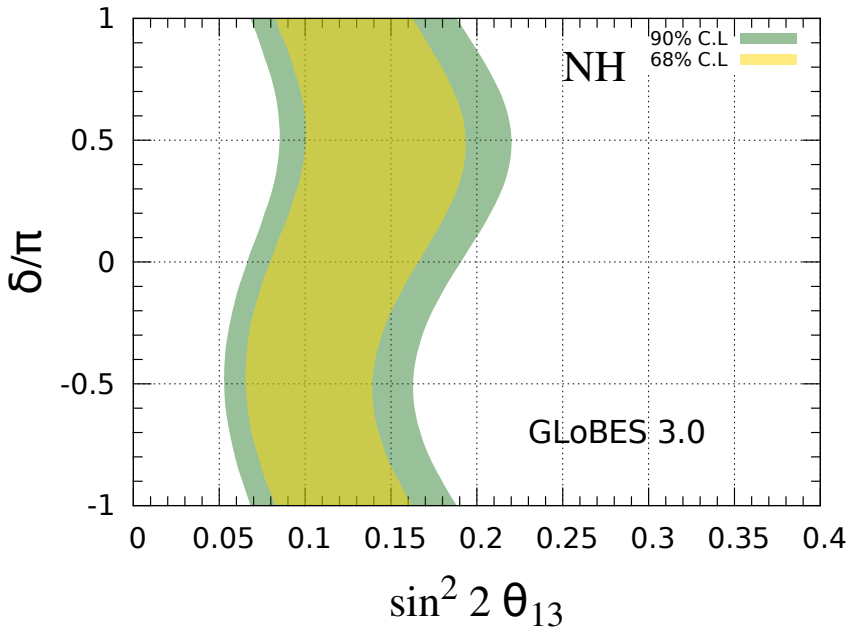

Figure 1.11: Allowed parameter region for the shown oscillation parameters. Not shown oscillation parameters have been fixed to their best fit values from [1].

numerical version of Eq. (1.50), which is calculated for oscillations in constant matter with a density value of $2.6\,\mathrm{g/cm^3}$. Using the value for the normalization error $\sigma_a = 8.8\%$ [37] and minimizing the χ^2 function in Eq. (1.67), we can estimate the allowed parameter region as it is shown in Fig. 1.11. All not shown parameters are fixed to their best fit values from Ref. [1]. We find a best fit point (bfp) $\sin^2(2\theta_{13}) = 0.113$ for NH and $\delta_{CP} = 0$. The value reported by the T2K collaboration is $\sin^2(2\theta_{13}) = 0.144$ [37].

We make a final comment about the detector energy resolution function. A common way to include the smearing due to the difference between the true energy E' and the neutrino reconstructed energy is assuming a Gaussian distribution function centered in the true energy with a standard deviation that is a function of the reconstructed energy. The standard deviation, in GLoBES, is parametrized as:

$$\sigma(E) = \alpha\, E + \beta\, \sqrt{E} + \gamma\ , \tag{1.68}$$

where the coefficients α, β and γ are measured by the experimental collaboration as an energy calibration error. Unfortunately, sometimes the experimental collaboration does not make public the values for the coefficients in Eq. (1.68), as it is the case for T2K. We then use one ob-

servable, for instance the total expected events with no oscillations (or a MC expectation with a given set of parameters), to fit the coefficients. At the end we have to agree not only in that number but also in the spectral shape. In Fig. 1.11 we have used $(\alpha, \beta, \gamma) = (0.20, 0.10, 0.05)$.

1.7 Global analysis

Updated solar neutrino analysis

As in our previous global fit to neutrino oscillations [1], here we consider the most recent results from the solar experiments Homestake [43], Gallex/GNO [44], SAGE [45], Borexino [46], SNO [23, 47] and the first three solar phases of Super-Kamiokande [48–50]. Here we have included the revised results from the third solar phase of Super-Kamiokande, published in December 2012 in the arXiv version of Ref. [50]. This revision corrects the estimated systematic error on the total flux observed in Super-Kamiokande as well as the total ^{8}B flux calculation. We find that the changes are very small and their impact on the determination of solar oscillation parameters is hardly noticeable. We also include the results from the fourth solar phase of Super-Kamiokande, SK-IV [51]. This data release corresponds to 1306.3 live-days and is presented in the form of 23 day and night energy bins. Thanks to several improvements in the hardware and software of Super-Kamiokande, an improved systematic uncertainty as well as a very low energy threshold of 3.5 MeV have been achieved. As we will discuss later, these new data consolidate the previous Super-Kamiokande solar data releases, with a minor impact in the global fit to neutrino oscillations. More detailed information on our simulation and analysis of solar neutrino data can be found in Refs. [1, 52, 53].

New reactor data

For the statistical analysis of reactor data we follow the same strategy explained in section 1.5.1. We define a χ^2 that compares the observed and measured event rates at each anti-neutrino detector. Several pull parameters are introduced in order to account for the different systematical errors associated to the reactor, detector and background uncertainties. An absolute normalization factor is left free in the fit, to be determined from the experimental data. This

technique is also used in the official analyses performed by the Daya Bay and RENO Collaborations [36, 54]. For the analysis of reactor data we take into account the total rate analysis of the latest Double Chooz data in Ref.[55], already discussed in our previous fit, as well as the new reactor data released by Daya Bay and RENO and described below.

RENO

The Reactor Experiment for Neutrino Oscillations (RENO) is a short-baseline reactor neutrino oscillation experiment located in South Korea. RENO consists of six reactor cores with maximum powers ranging from 2.66 GW_{th} to 2.8 GW_{th} and two identical anti-neutrino detectors located at 294 and 1383 m from the center of the reactor array. With both near and far detectors, RENO provided an important confirmation of the first Daya Bay measurement of θ_{13} [54]. We use their updated results presented at the TAUP 2013 conference [56], consisting of 403 days of data-taking, with improved systematic uncertainties, background estimates and energy calibration.

New long–baseline neutrino data

Over the last two years new data on ν_μ disappearance and ν_e appearance have been released by the long-baseline accelerator experiments MINOS and T2K. Below we summarize the most recent data from both experiments included in our global fit. As in our previous analysis, we use the GLoBES software package [42] for the simulation and statistical analysis of accelerator neutrino oscillation data from MINOS and T2K. The expected event numbers for a given channel in a particular detector are determined using the full three-neutrino survival probability with the relevant matter effects. As we will see, these data will play an important role in the global fit, since they provide key contributions to the determination of the atmospheric oscillation parameters and the CP violation phase. We now discuss them separately.

Disappearance channel in MINOS

The latest measurements of the ν_μ disappearance channel in MINOS have been published in Ref. [39]. These results come from the full MINOS data set, collected over a period of nine years and correspond to exposures of 10.71×10^{20} protons on target (POT) in the ν_μ-dominated

beam and 3.36×10^{20} POT in the $\bar{\nu}_\mu$-enhanced beam. One of the key features of these data sample is the preference for a non-maximal value of the atmospheric mixing angle θ_{23}. In fact, from the official MINOS analysis, one obtains that maximal mixing is disfavored at the 86% C.L.

Appearance channel in MINOS

The most recent results for the searches of ν_e appearance in MINOS have been reported in Ref. [40]. These data correspond to exposures of 10.6×10^{20} POT in the neutrino channel and 3.3×10^{20} POT in the anti-neutrino channel. The neutrino sample is the same as in the preliminary results presented in the Neutrino 2012 conference, used in our previous analysis. However, there are some differences in the reconstructed energy distributions. We are now using the full update from Ref. [40].

Disappearance channel in T2K

The latest results for the ν_μ disappearance channel in T2K have been collected from January 2010 to May 2013, during the four runs of the experiment and correspond to a total exposure of 6.57×10^{20} POT [57]. In comparison with the previous T2K results in Ref. [58], sensitivities have been improved thanks to new event selection and reconstruction techniques, as well as higher statistics at the near off-axis detector. A total number of 120 muon neutrino event candidates have been observed at the far detector while $446.0 \pm 22.5(\text{sys.})$ events were expected in absence of oscillations. As we will see in the next section, the T2K disappearance data now provides the most precise measurement of the atmospheric mixing angle θ_{23} with better sensitivity than all other experiments. Moreover, in contrast to the MINOS ν_μ disappearance data, they prefer a best fit θ_{23} value very close to maximal. This point will be crucial for the θ_{23} octant (in)determination from the global neutrino oscillation analysis.

Appearance channel in T2K

As for the disappearance channel, the latest available T2K appearance data correspond to a total exposure of 6.57×10^{20} POT, collected from run 1 to run 4 in the experiment [37]. A total of 4.92 ± 0.55 background events were expected in the absence of oscillations, while a

sample of 28 electron neutrino events have been detected. The observed event distribution is consistent with an appearance signal at $7.3\,\sigma$.

1.8 Results

In addition to the solar, reactor and long-baseline accelerator neutrino data described in the previous section, in our global fit to neutrino oscillations we also include the last results from the KamLAND reactor experiment presented in Ref. [59] as well as the atmospheric neutrino analysis provided by the Super-Kamiokande Collaboration in Ref. [60].

1.8.1 The role of long–baseline neutrino data in atmospheric parameter determination

Long-baseline neutrino data have by now achieved very good precision. In fact, the determination of the atmospheric oscillation parameters has become fully dominated by the combination of T2K and MINOS data. This can be appreciated from Fig. 1.12, where one sees how the latest T2K data places the best constraint on the atmospheric angle θ_{23}, while MINOS still provides the best determination for the atmospheric mass splitting Δm^2_{31}. Atmospheric neutrino data from Super-Kamiokande are in full agreement with the parameter regions determined by long-baseline results, though with less sensitivity. In this figure we confirm the result obtained by the experimental collaborations about the maximality of the atmospheric angle. MINOS data have a mild preference for non maximal θ_{23}, although $\theta_{23} = \pi/4$ is inside the 90% CL region for 2 d.o.f. The absolute best fit point from the analysis of MINOS lies in the first octant, $\theta_{23} < \pi/4$, although values in the second octant are allowed with very small $\Delta\chi^2$. Concerning T2K data, one sees that both for normal (left panel) and inverted mass hierarchy (right panel) the best fit value is very close to maximal: $\sin^2\theta_{23} = 0.52$ in both cases, maximal mixing being allowed with very small $\Delta\chi^2$ with respect to the absolute minimum: 0.03 (0.02) for normal (inverted) mass ordering. The global fit preference for values of θ_{23} in the second octant emerges after the combination with reactor data, as we will discuss in the next

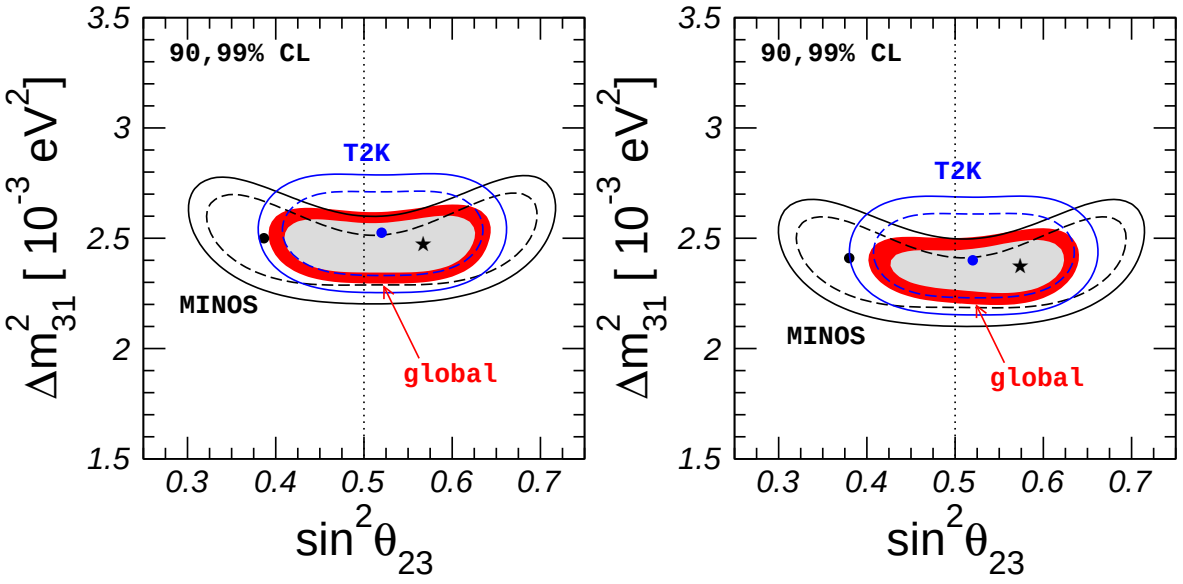

Figure 1.12: 90 and 99% C.L. regions in the $\sin^2\theta_{23}$ - Δm^2_{31} plane from separate analysis of MINOS (black lines), T2K (blue lines) and from the global analysis of all data samples (colored regions). The left (right) panel corresponds to normal (inverted) mass ordering.

subsection. We find the best fit points:

$$\sin^2\theta_{23} = 0.567^{+0.032}_{-0.128} \quad \Delta m^2_{31} = (2.48^{+0.05}_{-0.07}) \times 10^{-3}\text{eV}^2 \quad \text{(normal hierarchy)}\ , \tag{1.69}$$

$$\sin^2\theta_{23} = 0.573^{+0.025}_{-0.043} \quad \Delta m^2_{31} = (2.38^{+0.05}_{-0.06}) \times 10^{-3}\text{eV}^2 \quad \text{(inverted hierarchy)} \tag{1.70}$$

Note that for normal hierarchy a local minimum appears in the first octant ($\sin^2\theta_{23} = 0.467$) with $\Delta\chi^2 = 0.28$ with respect to the global minimum. For the case of inverted hierarchy, solutions with $\sin^2\theta_{23} \leq 0.5$ appear only with $\Delta\chi^2 > 1.7$. Comparing with our previous global fit, we see that best fit values for the atmospheric mixing angle are slightly shifted towards maximal values thanks to the latest T2K data. Likewise, Δm^2_{31} values are also shifted towards lower values due to T2K data, which now prefer smaller values of the atmospheric mass splitting.

1.8.2 The θ_{23} octant and the CP violation phase δ

In this section we will discuss the complementarity between long–baseline accelerator and reactor neutrino data in the determination of the θ_{23} octant as well as the CP phase δ. We will quantify the new sensitivity to the CP violation phase δ as well as the octant of the

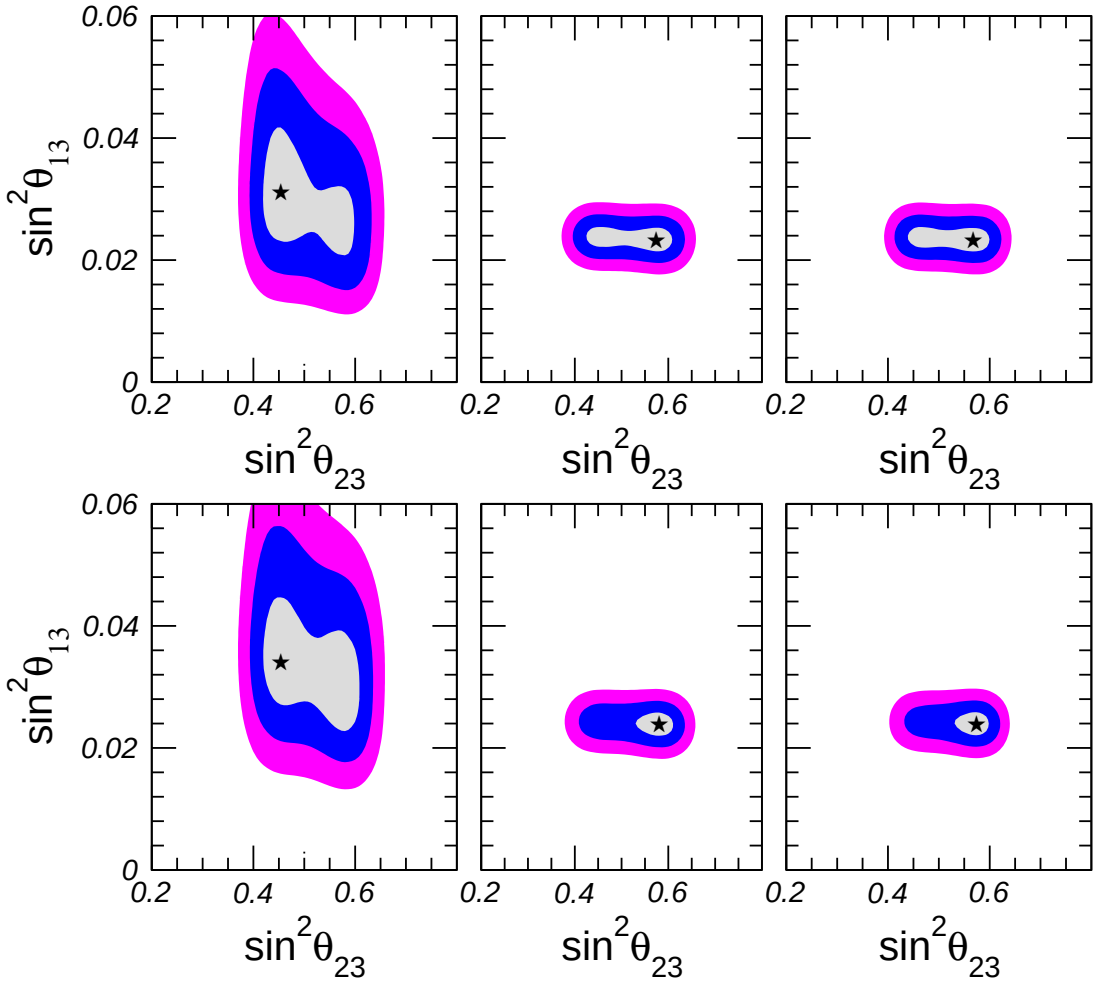

Figure 1.13: Upper panels: contour regions with $\Delta\chi^2 = 1$, 4, 9 in the $\sin^2\theta_{23}$ - $\sin^2\theta_{13}$ plane from the analysis of long–baseline (MINOS and T2K) + solar + KamLAND data (left panel), long-baseline + solar + KamLAND + new Double Chooz, Daya Bay and RENO reactor data (middle panel) and the global combination (right panel) for normal hierarchy. Lower panels, the same but for inverted neutrino mass hierarchy.

atmospheric mixing angle θ_{23}. This emerges by combining the latest accelerator with the latest reactor data.

We start by discussing the effect of the different data samples upon the possible preference for a given octant of θ_{23}. Our results are shown in Fig. 1.13. There we display the allowed regions at $\Delta\chi^2 = 1$, 4, 9 in the $\sin^2\theta_{23}$ - $\sin^2\theta_{13}$ plane for normal (upper panels) and inverted (lower panels) neutrino mass hierarchy. In order to appreciate the effect of the individual data sample combinations on the parameter determinations we have prepared three different panels in this plane. The left panel is obtained by the combination of the long-baseline

data from MINOS and T2K and the results of all solar neutrino experiments plus KamLAND. The accelerator MINOS and T2K data already produce a rather restricted allowed region in parameter space, showing an anti-correlation between θ_{23} and θ_{13} coming essentially from the oscillation probability in the ν_e appearance channel. In this panel solar and KamLAND impose only minor constraints on the reactor mixing angle θ_{13}. In the middle panel of Fig. 1.13, the data samples from Double Chooz, Daya Bay and RENO have been included in the analysis. Here one can see how the very precise determination of θ_{13} at reactor experiments, particularly Daya Bay, considerably reduces the allowed region. On the other hand, the Daya Bay preference for values of $\sin^2\theta_{13}$ around 0.023-0.024 moves the best fit value of θ_{23} to the second octant. This effect is particularly important for the case of inverted hierarchy, because of the slightly larger values of θ_{13} preferred for $\theta_{23} < \pi/4$. As a result, the first octant region is more strongly disfavored so that values of $\sin^2\theta_{23} < \pi/4$ are allowed only with $\Delta\chi^2 > 1.5$. Finally, the right-most panel shows the allowed regions after the inclusion of the Super-Kamiokande atmospheric data [60]. One can see that there is basically no change between middle and right panel. This follows from the fact that the analysis of atmospheric data we adopt does not show a particular preference for any octant of θ_{23}, both of which are allowed at 1σ. This behavior is also confirmed in the preliminary versions of updated Super-Kamiokande analysis in Refs. [61, 62].

Now we turn to the discussion of the sensitivity to the CP violation phase, δ. Our previous global analysis in Ref. [1] showed essentially no dependence on this phase. However the new results on ν_e appearance at long-baseline experiments in combination with the very precise measurement of θ_{13} at reactor experiments provides, for the first time, a substantial sensitivity to the CP phase δ. This new effect is illustrated in Fig. 1.14. Here, left panels show the allowed regions with $\Delta\chi^2 = 1$, 4, 9 in the $\sin^2\theta_{13}$-δ plane from the analysis of long-baseline accelerator data from MINOS and T2K, in both appearance as well as disappearance channels. This is indicated by three different line styles used in the left panels. On the other hand, the colored regions correspond to the results obtained from the global oscillation analysis. As expected the combination with reactor data results in narrower regions for θ_{13}. One can also notice that there is a mismatch between the region of θ_{13} preferred by accelerator data for values of the CP phase δ around 0.5π and the measured value of this mixing angle at reactor experiments such as Daya Bay, which dominates the best fit determination. As a result of

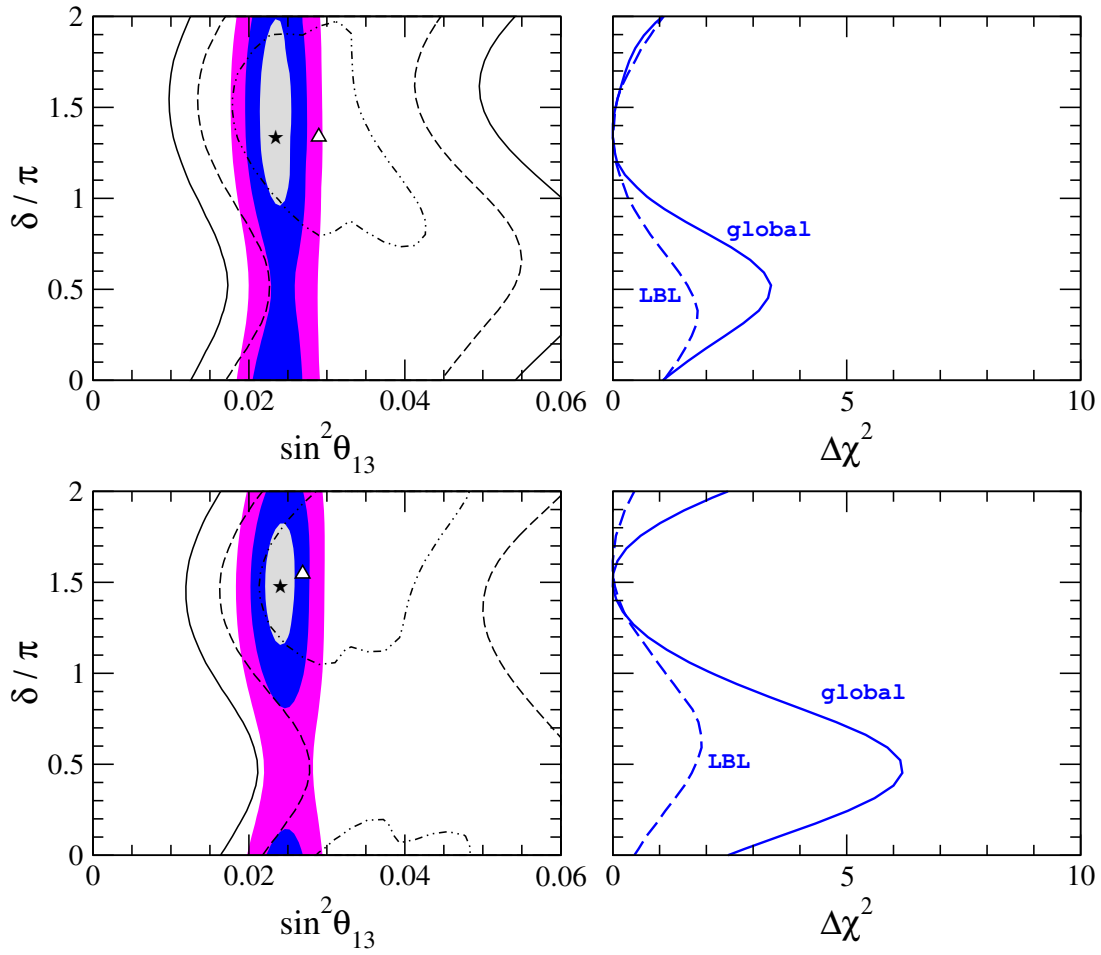

Figure 1.14: Left panels: contour regions with $\Delta\chi^2 = 1$, 4, 9 in the θ_{13}-δ plane from the analysis of LBL data alone (lines) and from the combined global analysis (colored regions). Right panels: $\Delta\chi^2$ as a function of the CP-violating phase δ from the analysis of LBL data (dashed line) as well as from the global analysis (solid line). Upper (lower) figures correspond to NH (IH).

this mismatch one obtains in the global analysis a significant rejection for values of δ phase around 0.5π. This can be seen in the right panels of Fig. 1.14. Here one notices that for normal hierarchy values of $\delta \simeq \pi/2$ are disfavored with $\Delta\chi^2 = 3.4$ (1.8σ), while for inverted hierarchy they are disfavored with $\Delta\chi^2 = 6.2$ (2.5σ). In both cases the preferred δ value is located close to 1.5π. The best fit points and 1σ errors on δ are given by:

$$\delta = (1.34^{+0.64}_{-0.38})\pi \quad \text{(normal hierarchy)} \,, \tag{1.71}$$

$$\delta = (1.48^{+0.34}_{-0.32})\pi \quad \text{(inverted hierarchy)} \,. \tag{1.72}$$

Comparing now with other global neutrino oscillation analyses in the literature we find

that our results on the CP phase qualitatively agree with the ones in the updated version of [63] available in [64]. The agreement holds for their global analysis without atmospheric data. Note, however, that these authors have also included the effect of the δ in the atmospheric data sample, not included in the official Super-Kamiokande analysis we adopt here. As a result, their global fit results show a somewhat stronger rejection against $\delta \simeq \pi/2$ than we find, as expected. Turning now to the results of the analysis given in Ref. [65] we find, in contrast, that their agreement with our results is worse.

1.8.3 Summary of global fit

In this section we summarize the results obtained in our global analysis to neutrino oscillations. In Fig. 1.15 we present the $\Delta\chi^2$ profiles as a function of all neutrino oscillation parameters. In the panels with two lines, the solid one corresponds to normal hierarchy while the dashed one gives the result for inverted mass hierarchy. Best fit values as well as 1, 2 and 3σ allowed ranges for all the neutrino oscillation parameters are reported in Table 1.3.

First we note that solar neutrino parameter determination is basically unchanged with respect to our previous global fit in [1]. We find that the inclusion of the new SK-IV solar data sample leads only to minor modifications in the $\sin^2\theta_{12}$ and Δm^2_{21} best fit values. As we already discussed in the previous section, the atmospheric neutrino parameters are now determined mainly by the new long-baseline data. With the new T2K data, the preferred value for the mass splitting Δm^2_{31} is now somewhat smaller, while the best fit value for the atmospheric angle θ_{23} has been shifted towards values closer to maximal. The status of maximal θ_{23} mixing angles has also been improved thanks to the latest T2K disappearance data. Regarding the reactor mixing angle $\sin^2\theta_{13}$, the more precise reactor data from Daya Bay and RENO have reduced the allowed 1σ range from $\sim$11% to $\sim$8%. The preferred value of θ_{13} has also been shifted to somewhat smaller values. Finally, thanks to the combination of the latest accelerator and reactor neutrino data, we have obtained an enhanced sensitivity to the CP violation phase. We find preferred values for δ around 1.5π for both mass hierarchies. On the other hand, values close to 0.5π are disfavored at 1.8σ (2.5σ) for normal (inverted) mass ordering.

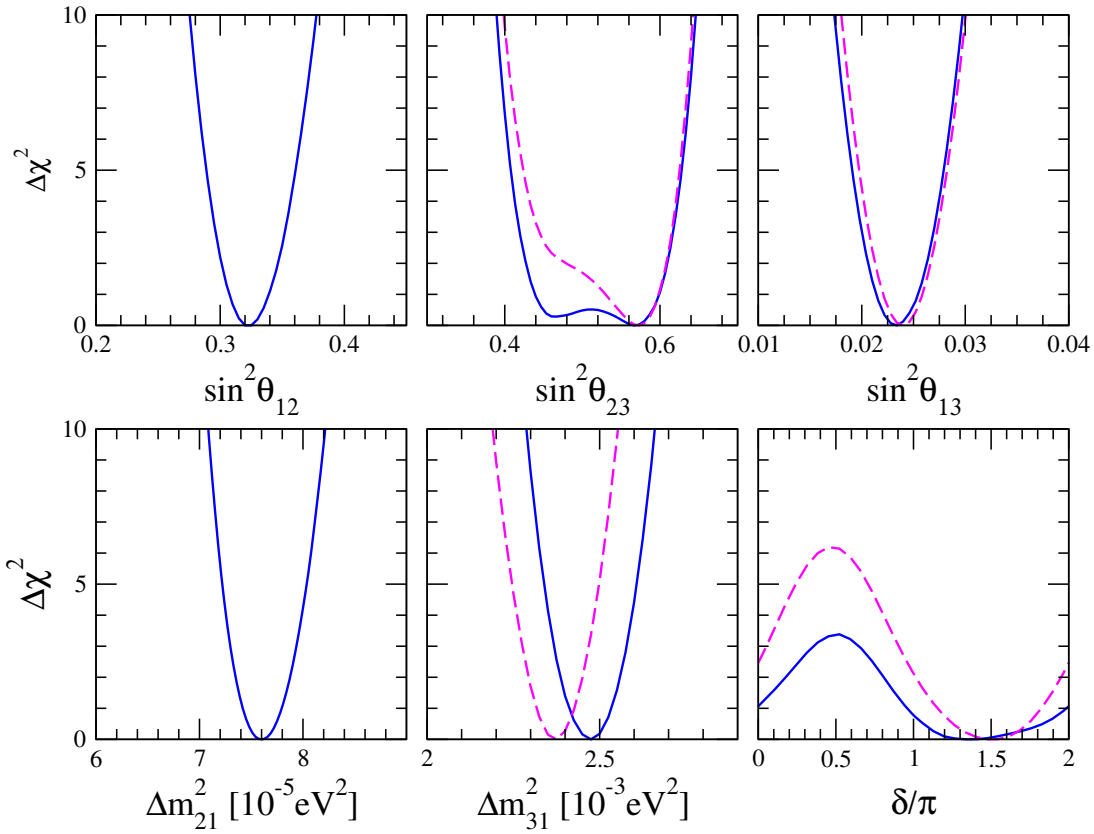

Figure 1.15: $\Delta\chi^2$ profiles as a function of all the neutrino oscillation parameters $\sin^2\theta_{12}$, $\sin^2\theta_{23}$, $\sin^2\theta_{13}$, Δm^2_{21}, Δm^2_{31} and the CP phase δ. For the central and right panels the solid lines correspond to the case of normal mass hierarchy while the dashed ones correspond to inverted mass hierarchy.

parameter	best fit	1σ range	2σ range	3σ range
Δm^2_{21} $[10^{-5}\text{eV}^2]$	7.60	7.42–7.79	7.26–7.99	7.11–8.18
$\lvert\Delta m^2_{31}\rvert$ $[10^{-3}\text{eV}^2]$ (NH)	2.48	2.41–2.53	2.35–2.59	2.30–2.65
$\lvert\Delta m^2_{31}\rvert$ $[10^{-3}\text{eV}^2]$ (IH)	2.38	2.32–2.43	2.26–2.48	2.20-2.54
$\sin^2\theta_{12}/10^{-1}$	3.23	3.07–3.39	2.92–3.57	2.78–3.75
$\sin^2\theta_{23}/10^{-1}$ (NH)	5.67 (4.67)[1]	4.39–5.99	4.13–6.23	3.92 – 6.43
$\sin^2\theta_{23}/10^{-1}$ (IH)	5.73	5.30–5.98	4.32–6.21	4.03–6.40
$\sin^2\theta_{13}/10^{-2}$ (NH)	2.34	2.14–2.54	1.95–2.74	1.77–2.94
$\sin^2\theta_{13}/10^{-2}$ (IH)	2.40	2.21–2.59	2.02–2.78	1.83–2.97
δ/π (NH)	1.34	0.96–1.98	0.0–2.0	0.0–2.0
δ/π (IH)	1.48	1.16–1.82	0.0–0.14 & 0.81-2.0	0.0–2.0

Table 1.3: Neutrino oscillation parameters summary. For Δm^2_{31}, $\sin^2\theta_{23}$, $\sin^2\theta_{13}$, and δ the upper (lower) row corresponds to normal (inverted) neutrino mass hierarchy.

[1] This is a local minimum in the first octant of θ_{23} with $\Delta\chi^2 = 0.28$ with respect to the global minimum

CHAPTER 2

Neutrino mass model with a flavor symmetry

The large mass difference between the SM particles that belong to different families and the number of families itself are not explained in the SM. After the confirmation of the neutrino oscillation mechanism as the explanation for the flavor neutrino transitions, the lepton sector has to be enlarged with neutrino masses and mixing angles in analogy to with the sector of quarks. However, explaining both sectors with a common origin from a unified theory of flavor is challenging due to the different mixing pattern observed for quarks and leptons.

In the case of the lepton sector, two of the mixing angles, atmospheric and solar, are 'large' (compared with the Cabbibo angle) with the former one being compatible with maximal mixing. Assuming the reactor mixing angle is compatible with zero, as it was the case before 2012, and also assuming the mixing pattern is not accidental, one can expect the lepton mixing might come as a consequence of a given flavor symmetry. This has motivated a strong effort towards the formulation of symmetry-based approaches to address the flavor problem, in terms of an underlying flavor symmetry of leptons and/or quarks, separately or jointly. Indeed, these earlier observations were successfully accounted for in terms of an underlying A_4 flavor symmetry [66, 67].

However, as explained in chapter 1, accelerator and especially reactor data excluded a zero

value for the reactor mixing angle. These results open the possibility to explore leptonic CP violation [7, 68] which is one of the ingredients required to explain the baryonic asymmetry in the universe through the leptogenesis mechanism. This finding provides a challenge for many A_4-based schemes [66, 67], specially those leading to the so–called tri-bimaximal (TBM) mixing ansatz proposed by Harrison, Perkins and Scott [69]. This scheme is now ruled out mainly by the Daya Bay measurement of the reactor mixing angle.

In this chapter we focus on the model proposed by Babu, Ma and Valle [66], studied in detail in Ref. [70]. We present a simple extension of this model that introduces an extra scalar singlet flavon field ζ transforming as a $1'$ of A_4 to the Yukawa sector of the model. We show explicitly how this breaks the remnant symmetry present in the charged-lepton sector, so as to induce a nonzero θ_{13} value, hence making the model fully realistic and opening the possibility of CP violation in neutrino oscillations. Both θ_{13} and the CP-violating invariant J_{CP} correlate with the new term added to the model superpotential.

This chapter is based on the work done in Ref. [71], an is organized as follows: in section 2.1 we review the basic A_4 group properties. Then we introduce a non supersymmetric model in section 2.2 that will help us to introduce the model proposed by Babu, Ma and Valle [66] (BMV) in section 2.3. After that, we present a simple extension of the BMV model in section 2.4 that successfully accommodates the current neutrino mixing angles. We close with an analytical discussion of the results, in a specific limit where the neutrino mixing angles can be solved perturbatively, in section 2.5.

2.1 The A_4 group

In this section we introduce the non-abelian discrete group A_4, following the appendix of Ref [72]. All finite groups are completely characterized by means of a set of elements called generators of the group and a set of relations, so that all the elements of the group are given as products of the generators. The group A_4 consists of the even permutations of four objects and contains $4!/2 = 12$ elements. The generators are S and T with the relations $S^2 = T^3 = (ST)^3 = \mathcal{I}$, and then, the elements of the group are:

$$1, S, T, ST, TS, T^2, ST^2, STS, TST, T^2S, TST^2, T^2ST\,.$$

	$C_1 = \{I\}$	$C_2 = \{T\}$	$C_3 = \{T^2\}$	$C_4 = \{S\}$
1	1	1	1	1
$1'$	1	ω	ω^2	1
$1''$	1	ω^2	ω	1
3	3	0	0	-1

Table 2.1: Character table of A_4 where C_i are the different classes and $\omega^3 \equiv 1$.

A_4 has four irreducible representations (see table 2.1), three singlets $1,\ 1'$ and $1''$ and one triplet. One of the main features of A_4 is that it is the smallest discrete group with a triplet representation.

The one-dimensional unitary representations are obtained by:

$$\begin{array}{lll} 1 & S = 1 & T = 1 \\ 1' & S = 1 & T = \omega \\ 1'' & S = 1 & T = \omega^2 \end{array} \tag{2.1}$$

where $\omega^3 = 1$. The product rules for the singlets are:

$$\begin{aligned} & 1 \times 1 = 1' \times 1'' = 1 \\ & 1' \times 1' = 1'' \\ & 1'' \times 1'' = 1' \end{aligned} \tag{2.2}$$

In the basis where S is real and diagonal, the group generators can be expressed as:

$$S = \begin{pmatrix} 1 & 0 & 0 \\ 0 & -1 & 0 \\ 0 & 0 & -1 \end{pmatrix} ; \quad T = \begin{pmatrix} 0 & 1 & 0 \\ 0 & 0 & 1 \\ 1 & 0 & 0 \end{pmatrix} ; \tag{2.3}$$

one has the following triplet multiplication rules,

$$\begin{aligned} (ab)_1 &= a_1 b_1 + a_2 b_2 + a_3 b_3 \, ; \\ (ab)_{1'} &= a_1 b_1 + \omega a_2 b_2 + \omega^2 a_3 b_3 \, ; \\ (ab)_{1''} &= a_1 b_1 + \omega^2 a_2 b_2 + \omega a_3 b_3 \, ; \\ (ab)_{3_1} &= (a_2 b_3, a_3 b_1, a_1 b_2) \, ; \\ (ab)_{3_2} &= (a_3 b_2, a_1 b_3, a_2 b_1) \, , \end{aligned} \tag{2.4}$$

	$(\nu_i, l_i)_L$	l_{1R}	l_{2R}	l_{3R}	N_{iR}	$\Phi_i = (\phi_i^+, \phi_i^0)$	$\eta = (\eta^+, \eta^0)$
A_4	3	1	$1'$	$1''$	3	3	1
LN	1	1	1	1	0	0	-1

Table 2.2: Flavor assignments of the particle content of the model. The second row labeled as LN corresponds to the lepton number.

where $a = (a_1, a_2, a_3)$ and $b = (b_1, b_2, b_3)$.

The decomposition property of the product is given by:

$$\underline{3} \times \underline{3} = \underline{1} + \underline{1}' + \underline{1}'' + \underline{3} + \underline{3}\,. \tag{2.5}$$

The relations in Eqs. (2.2) and (2.4) are often used to write the A_4 invariants terms in the Lagrangian in matrix form in a specific basis.

2.2 A model with degenerate neutrino masses

As starting point we will review a previous A_4 model without supersymmetry, from Ref [73], with the particle content in table 2.2.

The SM leptons, $SU(2)$ singlets and doublets, have been assigned to the three A_4 singlets and triplet representations. As we will see later on, this will provide a particular structure for the charged leptons. From table 2.2 we can see that, in addition to the SM leptons, three right-handed singlet fermions N_{iR} and four Higgs doublets, Φ_i and η, were added, with $i = 1, 2, 3$.

With the field assignments in table 2.2, the Lagrangian with the invariant terms is given by [73]:

$$\frac{1}{2} M N_{iR}^2 + f \bar{N}_{iR}(\nu_{iL}\eta^0 - l_{iL}\eta^+) + h_{ijk}\overline{(\nu_i, l_i)}_L l_{jR}\Phi_k + h.c., \tag{2.6}$$

where the first term is a Majorana fermion mass while the second one, after η takes a vev, is a Dirac neutrino mass term. The third term in Eq. (2.6), after Higgs vevs, will produce the charged lepton masses.

The structure for the charged-lepton mass matrix is dictated by the A_4 symmetry due to the assignment in table 2.2, which then will fix the structure of the diagonalization matrix and finally the neutrino mixing matrix structure. In order to elucidate these structures, first for charged leptons, we notice that the right-handed leptons are singlets of A_4. Then from Eq. (2.2), in order to have an invariant term under A_4, the product of triplet should produce the corresponding singlet using Eq. (2.4). The charged-lepton mass term can be written symbolically as:

$$\tilde{h}_1 \left(3 \times 3\right)_1 \times 1 + \tilde{h}_2 \left(3 \times 3\right)_{1'} \times 1' + \tilde{h}_3 \left(3 \times 3\right)_{1''} \times 1''$$

Since in the triplet products in Eq. (2.4) are not mixing terms of the form $a_i b_j = 0$, then it is useful to define the following diagonal matrices [73]:

$$h_{i1k} = h_1 \begin{bmatrix} 1 & 0 & 0 \\ 0 & 1 & 0 \\ 0 & 0 & 1 \end{bmatrix}, \quad h_{i2k} = h_2 \begin{bmatrix} 1 & 0 & 0 \\ 0 & \omega & 0 \\ 0 & 0 & \omega^2 \end{bmatrix}, \quad h_{i3k} = h_3 \begin{bmatrix} 1 & 0 & 0 \\ 0 & \omega^2 & 0 \\ 0 & 0 & \omega \end{bmatrix}. \tag{2.7}$$

We can rearrange the charged lepton mass matrix as :

$$\bar{l}_{iL}(h_{\mathbf{i}\mathbf{j}k}v_k)l_{\mathbf{j}R} = \bar{l}_{iL}(h_{\mathbf{i}\mathbf{j}i}v_i)l_{\mathbf{j}R} = \bar{l}_{iL}\left(\mathcal{M}_l\right)_{\mathbf{i}\mathbf{j}} l_{\mathbf{j}R} \tag{2.8}$$

where $\langle \Phi_k \rangle \equiv v_k$. Finally, the charged-lepton mass matrix is given by:

$$\mathcal{M}_l = \begin{bmatrix} h_1 v_1 & h_2 v_1 & h_3 v_1 \\ h_1 v_2 & h_2 \omega v_2 & h_3 \omega^2 v_2 \\ h_1 v_3 & h_2 \omega^2 v_3 & h_3 \omega v_3 \end{bmatrix}. \tag{2.9}$$

The minimization of the Higgs potential requires the condition:

$$v_1 = v_2 = v_3 \equiv v\,.$$

The charged lepton mass matrix in Eq. (2.9) can be written as:

$$\mathcal{M}_l = U_L \cdot \mathrm{diag}\{\sqrt{3}h_i v\}\,, \tag{2.10}$$

and the matrices that diagonalize the charged-lepton matrix $U_L^\dagger \mathcal{M}_l U_R = \mathrm{diag}\{m_i\}$ are, by inspection, given by:

$$U_L = \frac{1}{\sqrt{3}} \begin{bmatrix} 1 & 1 & 1 \\ 1 & \omega & \omega^2 \\ 1 & \omega^2 & \omega \end{bmatrix}, \quad U_R = \begin{bmatrix} 1 & 0 & 0 \\ 0 & 1 & 0 \\ 0 & 0 & 1 \end{bmatrix}. \tag{2.11}$$

We can then rotate the left-handed fields in the Lagrangian in Eq. (2.6) by U_L, leading to the basis were charged-leptons are diagonal, and where the Majorana mass matrix in the basis (ν, N) is then given by [73]:

$$\mathcal{M}_{(\nu,N)} = \begin{bmatrix} 0 & U_L^\dagger f u \\ U_L^* f u & M \end{bmatrix}. \tag{2.12}$$

Finally, from block diagonalization, the effective 3×3 mass matrix for neutrinos has the form [73]:

$$\mathcal{M}_\nu = \frac{f^2 u^2}{M} U_L^T U_L = \frac{f^2 u^2}{M} \begin{bmatrix} 1 & 0 & 0 \\ 0 & 0 & 1 \\ 0 & 1 & 0 \end{bmatrix}. \tag{2.13}$$

This matrix has degenerate eigenvalues, and therefore it does not properly describe the current neutrino phenomenology, where we have two squared mass differences, solar and atmospheric. In addition, the matrix has a $\mu - \tau$ symmetry what will produce a zero value for the reactor mixing angle, in disagreement with current data.

In the next section we will introduce a model that preserves some features of the model explained in this section, but solves the problem of the degenerate neutrino masses. Finally we will confront the second problem of generating a non-zero reactor mixing angle.

2.3 Babu Ma and Valle (BMV) Model

The BMV model [66] is the improved version of the model described in section 2.2. The main changes with respect to the previous model are the following:

- A_4 is broken at very high scale.
- Supersymmetry is added with explicit soft-breaking terms which also break A_4. At the electroweak scale the model is then a specific version of the Minimal Supersymmetric SM (MSSM).

	$\hat{Q}$	$\hat{L}$	$\hat{u}^c_1, \hat{d}^c_1, \hat{e}^c_1$	$\hat{u}^c_2, \hat{d}^c_2, \hat{e}^c_2$	$\hat{u}^c_3, \hat{d}^c_3, \hat{e}^c_3$	$\hat{\phi}_{1,2}$
A_4	3	3	1	$1'$	$1''$	1
Z_3	1	1	ω^2	ω^2	ω^2	1

Table 2.3: Flavor assignments of the MSSM fields, with $\omega = \exp i2\pi/3$.

	$\hat{U}$	$\hat{U}^c$	$\hat{D}$	$\hat{D}^c$	$\hat{E}$	$\hat{E}^c$	$\hat{N}^c$	$\hat{\chi}$
A_4	3	3	3	3	3	3	3	3
Z_3	1	1	1	1	1	1	1	ω

Table 2.4: Mirror quark, lepton and Higgs superfield assignments, with $\omega = \exp i2\pi/3$.

The particle content of the model is collected in Tables 2.3 and 2.4. The model implements an A_4 flavor symmetry within a supersymmetric context. The usual quark $\hat{Q}_i = (\hat{u}_i, \hat{d}_i)$, lepton $\hat{L}_i = (\hat{\nu}_i, \hat{e}_i)$, and Higgs $\hat{\phi}_i$ fields transform under A_4 as given in table 2.3. In addition, the heavy quark, lepton, and Higgs superfields indicated in table 2.4 are added. These are all $SU(2)$ singlets. The superpotential of the BMV model is then given by:

$$\begin{aligned}
\hat{W} = & M_U \hat{U}_i \hat{U}^c_i + f_u \hat{Q}_i \hat{U}^c_i \hat{\phi}_2 + h^u_{ijk} \hat{U}_i \hat{u}^c_i \hat{\chi}_k \\
& + M_D \hat{D}_i \hat{D}^c_i + f_d \hat{Q}_i \hat{D}^c_i \hat{\phi}_2 + h^d_{ijk} \hat{D}_i \hat{d}^c_i \hat{\chi}_k \\
& + M_E \hat{E}_i \hat{E}^c_i + f_e \hat{L}_i \hat{E}^c_i \hat{\phi}_1 + h^e_{ijk} \hat{E}_i \hat{e}^c_j \hat{\chi}_k \\
& + \frac{1}{2} M_N \hat{N}^c_i \hat{N}^c_i + f_N \hat{L}_i \hat{N}^c_i \hat{\phi}_2 + \mu \hat{\phi}_1 \hat{\phi}_2 \\
& + \frac{1}{2} M_\chi \hat{\chi}_i \hat{\chi}_i + h_\chi \hat{\chi}_1 \hat{\chi}_2 \hat{\chi}_3 \, .
\end{aligned} \tag{2.14}$$

The scalar potential involving χ_i is given by:

$$V = |M_\chi \chi_1 + h_\chi \chi_2 \chi_3|^2 + |M_\chi \chi_2 + h_\chi \chi_3 \chi_1|^2 + |M_\chi \chi_3 + h_\chi \chi_1 \chi_2|^2, \tag{2.15}$$

which has the supersymmetric solution $(V = 0)$

$$\langle \chi_1 \rangle = \langle \chi_2 \rangle = \langle \chi_3 \rangle = u \ . \tag{2.16}$$

We assume that the A_4 flavor symmetry is broken softly at some high scale [66].

The Dirac mass matrix linking (e_i, E_i) to (e_j^c, E_j^c) can be written as:

$$\mathcal{M}_{eE} = \begin{bmatrix} 0 & 0 & 0 & f_e v_1 & 0 & 0 \\ 0 & 0 & 0 & 0 & f_e v_1 & 0 \\ 0 & 0 & 0 & 0 & 0 & f_e v_1 \\ h_1^e\, u & h_2^e\, u & h_3^e\, u & M_E & 0 & 0 \\ h_1^e\, u & h_2^e\, u\, \omega & h_3^e\, u\, \omega^2 & 0 & M_E & 0 \\ h_1^e\, u & h_2^e\, u\, \omega^2 & h_3^e\, u\, \omega & 0 & 0 & M_E \end{bmatrix} \equiv \begin{bmatrix} 0 & X_1^I \\ X_2 & Y^I \end{bmatrix} , \tag{2.17}$$

where $v_1 = \langle \phi_1^0 \rangle$ [1], with similar forms also for the corresponding quark mass matrices. Notice that the structure of the lower left block of matrix in Eq. (2.17) is the same that the one for the charged leptons in the non supersymmetric model (see Eq. (2.10)).

In order to find the charged-lepton left mixing matrix we have to diagonalize the following matrix:

$$\begin{aligned} \mathcal{M}_{eE}(\mathcal{M}_{eE})^\dagger &= \begin{bmatrix} X_1^I (X_1^I)^\dagger & X_1^I (Y^I)^\dagger \\ Y^I\, (X_1^I)^\dagger & X_2\, X_2 + Y^I\, (Y^I)^\dagger \end{bmatrix} \\ &= \begin{bmatrix} (f_e v_1)^2\, I & M_E\, f_e v_1\, I \\ M_E\, f_e v_1\, I & U_\omega(\mathrm{diag}\{3(h_i^e u)^2\}) U_\omega^\dagger + M_E^2\, I \end{bmatrix} . \end{aligned} \tag{2.18}$$

Using the procedure described in the appendix C, one finds (using Eq. (C.10)) the reduced 3×3 Dirac mass matrix for the charged leptons is diagonalized by the magic matrix U_ω:

$$U_\omega = \frac{1}{\sqrt{3}} \begin{bmatrix} 1 & 1 & 1 \\ 1 & \omega & \omega^2 \\ 1 & \omega^2 & \omega \end{bmatrix} , \tag{2.19}$$

which is exactly the U_L matrix in Eq. (2.11). For future reference, the S matrix is given by:

$$\begin{aligned} i\, S &\approx -X_1^I (Y^I)^\dagger \left(X_1^I (X_1^I)^\dagger - X_2\, X_2 - Y^I\, (Y^I)^\dagger \right)^{-1} \\ &= U_\omega\, \mathrm{diag}\{-M_E\, f_e v_1 [(f_e v_1)^2 - 3(h_i^e u)^2 - M_E^2]^{-1}\}\, U_\omega^\dagger . \end{aligned} \tag{2.20}$$

For $f_e v_1 \ll h_i\, u \ll M_E$ the charged lepton masses are given by:

$$\tilde{m}_i^2 \simeq \frac{3 f_e^2 v_1^2}{M_E^2} \frac{h_i^{e\,2} u^2}{1 + 3(h_i^e u)^2 / M_E^2} . \tag{2.21}$$

[1] Here $\phi_{1,2}$ are the usual two Higgs fields of supersymmetry.

Turning to the neutral sector, the Majorana mass matrix in the basis (ν_i, N_i^c) and in the basis where charged leptons are diagonal, is given by:

$$\mathcal{M}_{\nu N} = \begin{bmatrix} 0 & f_N v_2 \, U_\omega \\ f_N v_2 \, U_\omega^T & M_N \end{bmatrix} , \tag{2.22}$$

where $v_2 = \langle \phi_2^0 \rangle$. Hence, the reduced light neutrino mass matrix after the seesaw becomes:

$$\mathcal{M}_\nu = \frac{f_N^2 \, v_2^2}{M_N} U_\omega^T U_\omega = m_0 \begin{bmatrix} 1 & 0 & 0 \\ 0 & 0 & 1 \\ 0 & 1 & 0 \end{bmatrix} = m_0 \, \lambda^{\mathbf{0}} \ , \tag{2.23}$$

leading to degenerate neutrino masses at this stage, as it was the case in the non-supersymmetric model (see Eq. (2.13)). However, because the BMV model is supersymmetric, Eq. (2.23) is corrected by the wave function renormalizations of ν_i, as well as the corresponding vertex renormalizations [66].

The structure of the one-loop corrections to the Majorana neutrino mass matrix can be written as [70]:

$$\lambda = \lambda^0 \, \tilde{\delta} + (\tilde{\delta})^T \, \lambda^0 \, , \tag{2.24}$$

where the matrix with the one-loop corrections $\tilde{\delta}$ is a general hermitian matrix.

Given the structure of the λ_{ij} elements at high scale (Eq. (2.23)), their expressions at low scale is fixed to first order as:

$$\lambda = \begin{bmatrix} 1 + 2\delta_{ee} & \delta_{e\mu} + \delta_{e\tau} & \delta_{e\mu} + \delta_{e\tau} \\ \delta_{e\mu} + \delta_{e\tau} & 2\delta_{\mu\tau} & 1 + \delta_{\mu\mu} + \delta_{\tau\tau} \\ \delta_{e\mu} + \delta_{e\tau} & 1 + \delta_{\mu\mu} + \delta_{\tau\tau} & 2\delta_{\mu\tau} \end{bmatrix} , \tag{2.25}$$

where all parameters are assumed to be real [66]. Rewriting Eq. (2.23) with $\delta_0 \equiv \delta_{\mu\mu} + \delta_{\tau\tau} - 2\delta_{\mu\tau}$, $\delta \equiv 2\delta_{\mu\tau}$, $\delta' \equiv \delta_{ee} - \delta_{\mu\mu}/2 - \delta_{\tau\tau}/2$ and $\delta'' \equiv \delta_{e\mu} + \delta_{e\tau}$ one has

$$\begin{bmatrix} 1 + \delta_0 + 2\delta + 2\delta' & \delta'' & \delta'' \\ \delta'' & \delta & 1 + \delta_0 + \delta \\ \delta'' & 1 + \delta_0 + \delta & \delta \end{bmatrix} , \tag{2.26}$$

so that the eigenvectors and eigenvalues can be determined *exactly*. The effective neutrino mixing matrix is given by

$$U_\nu(\theta) = \begin{bmatrix} \cos\theta & -\sin\theta & 0 \\ \sin\theta/\sqrt{2} & \cos\theta/\sqrt{2} & -1/\sqrt{2} \\ \sin\theta/\sqrt{2} & \cos\theta/\sqrt{2} & 1/\sqrt{2} \end{bmatrix} , \tag{2.27}$$

while the three light neutrino mass eigenvalues are:

$$\begin{aligned} \lambda_1 &= 1 + \delta_0 + 2\delta + \delta' - \sqrt{\delta'^2 + 2\delta''^2} \ , \\ \lambda_2 &= 1 + \delta_0 + 2\delta + \delta' + \sqrt{\delta'^2 + 2\delta''^2} \ , \\ \lambda_3 &= -1 - \delta_0 \ , \end{aligned} \tag{2.28}$$

so that one finds the BMV model predictions for the neutrino mixing angles, given by:

$$\begin{aligned} \tan^2\theta_{12} &= \frac{\delta''^2}{\delta''^2 + \delta'^2 - \delta'\sqrt{\delta'^2 + 2\delta''^2}} \ , \\ \sin^2\theta_{13} &= 0 \ , \\ \tan^2\theta_{23} &= 1 \Rightarrow \text{maximal} \ . \end{aligned} \tag{2.29}$$

For the remaining oscillation parameters, namely the mass squared differences, assuming $\delta', \delta'' \ll \delta$, one has

$$\begin{aligned} \Delta m^2_{21} &\simeq 4\sqrt{\delta'^2 + 2\delta''^2}\, m_0^2 \ , \\ \Delta m^2_{31} &\simeq \Delta m^2_{32} \simeq 4\delta \ m_0^2 \ . \end{aligned} \tag{2.30}$$

One sees that the mixing matrix in the neutrino sector in Eq. (2.29) has just one free parameter, θ, which corresponds to the unpredicted solar mixing angle, θ_{12}. The plot in Fig. 2.1 shows the solar mixing angle as a function of the loop corrections given by Eq. (2.29). The measured range for the solar mixing angle constrains the rate δ''/δ'.

We now assume that radiative corrections lift the neutrino mass degeneracy, as required by the solar neutrino oscillation data. Using the solar angle in Eq. (2.29) and the squared mass differences in Eq. (2.30), one can estimate the size of some of the wave function and vertex corrections required in order to fit the observed oscillation parameters. One finds the following relations

$$\begin{aligned} \frac{\delta}{|\delta'|} &= \xi \frac{\Delta m^2_{31}}{\Delta m^2_{21}} \left(\frac{1}{2\,\sin^2\theta - 1} \right) \approx 92.96\,\xi, \\ \frac{|\delta''|}{|\delta'|} &= \sqrt{\frac{1}{2}\left[\left(\frac{1}{2\,\sin^2\theta - 1} \right)^2 - 1 \right]} \approx 1.83, \end{aligned} \tag{2.31}$$

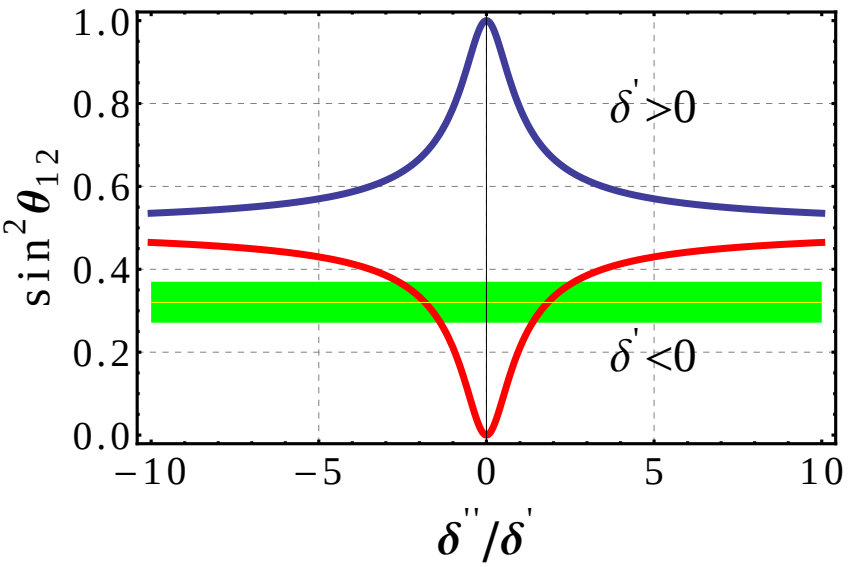

Figure 2.1: Solar mixing angle in the BMV model from Eq. (2.29). The horizontal band represents the solar mixing angle range at 3σ of C.L.

where $\xi = 1(-1)$ corresponds to the case of $\delta' > 0\,(\delta' < 0)$. In order to fit the neutrino oscillation data, the threshold parameter δ' must be of the same order as δ'' and also $\delta', \delta'' \ll \delta$. With $\delta' < 0$ and $|\delta''/\delta'| = 1.8$, the predicted neutrino mixing pattern is indeed consistent with the oscillation data before the latest `T2K`, `Daya Bay` and `RENO` results for θ_{13}.

2.4 Modifying the BMV model

The main goal of this work is to accommodate the current neutrino data [1] within a minimally extended A_4-based BMV scenario. In general, the effective mixing in the leptonic sector is given by:

$$K = U_\nu(\theta), \tag{2.32}$$

where we have gone to the basis where the charged leptons are diagonal, by rotating with the magic matrix U_ω. The idea is now to generate modifications of the mixing in the leptonic sector, $U'_\omega = U_\omega\, U_\delta$, in such a way that the modified lepton mixing matrix is given by

$$K' = U_\delta^\dagger\, U_\nu(\theta)\,. \tag{2.33}$$

Here U_δ denotes a correction which may yield a nonvanishing θ_{13} while keeping good predictions for the other neutrino oscillation parameters, in particular, the atmospheric mixing angle θ_{23}.

2.4.1 Charged lepton corrections to lepton mixing

As a first attempt we relax the condition we used to obtain the charged-lepton masses in Eq. (2.21), by allowing the scale M_E (see Eq. (2.17)) to lie at the TeV scale [2]. This results in unitarity violation corrections to the lepton mixing matrix. With M_E in Eq. (2.17) at the TeV scale, one must take into account not only the first order terms in the block diagonalization of the charged lepton mass matrix as in Eq. (2.21) but also the next-to-leading (NLO) order effects.

In order to calculate the NLO terms, one expands the exponential, as in Eq. (C.5) in the appendix, in a power series in S. The NLO terms are combinations of the identity and products of $S\ S^\dagger$ and S (see appendix C). Given the structure of the S matrix in Eq. (2.20) it is clear that even if we go to higher orders in the expansion, the effective charged lepton mass will always be diagonalized by the magic matrix U_ω. In other words: $U_\delta \equiv 1$.

The origin of the structure of the S matrix in Eq. (2.20) comes from the fact that in the BMV model, the matrices in the upper right corner and the lower right corner in Eq. (2.17) are proportional to the identity:

$$i\,S \approx -X_1^I (Y^I)^\dagger \left(X_1^I (X_1^I)^\dagger - X_2\,X_2 - Y^I\,(Y^I)^\dagger\right)^{-1} \approx -X_1^I (Y^I)^\dagger \left(-X_2\,X_2 - Y^I\,(Y^I)^\dagger\right)^{-1}\ , \tag{2.34}$$

as defined with the superindex in Eq. (2.17). In particular, in the perturbative regime, the charged-lepton mixing matrix conserves its structure because the $Y^I \sim I$. This fact suggests that an additional term in the superpotential in Eq. (2.14) proportional to $\hat{E}_i \hat{E}_i^c$ might modify the charged-lepton mixing matrix. The net effect is that, even allowing for unitarity violation in the charged sector, the structure of the lepton mixing matrix is unchanged. Somehow, a remnant symmetry of A_4 leads to $\theta_{13} = 0$.

2.4.2 Minimal flavon extension of the original A_4 model

In order to break the unwanted remnant symmetry present in the charged-lepton sector of the model, we now add a scalar singlet flavon field ζ to the superpotential in Eq. (2.14). The flavon scalar field ζ transforms as $1'$ under the A_4 flavor symmetry, leading to a new

[2] This would lead to the existence of flavor-changing neutral currents at the tree level. These would induce sizeable lepton flavor violating processes.

superpotential term of the form:

$$\zeta(E\,E^c)_{1''} \tag{2.35}$$

where we will parametrize the flavon scale as $\langle\zeta\rangle = \beta\, M_E$. This results in a new mass matrix for the lower right corner of Eq. (2.17) that now has the structure:

$$Y^I \to Y_D = M_E \times I + \beta M_E \times \mathrm{diag}\{1, \omega, \omega^2\}, \tag{2.36}$$

modifying the S matrix in Eq. (2.34). The corresponding charged lepton matrix in Eq. (2.18) is now given by

$$\mathcal{M}_{eE}(\mathcal{M}_{eE})^\dagger = \begin{bmatrix} (f_e v_1)^2\, I & f_e v_1\, Y_D^\dagger \\ f_e v_1\, Y_D & U_\omega(\mathrm{Diag}\{3(h_i^e u)^2\})U_\omega^\dagger + Y_D Y_D^\dagger \end{bmatrix}\,, \tag{2.37}$$

where Y_D is no longer diagonalized by the magic matrix. This changes the structure of the S matrix in Eq. (2.20) and breaks the unwanted remnant symmetry which leads to $\theta_{13} \equiv 0$. As a consequence, one obtains a corrected matrix U_ω^c that leads to a U_δ matrix of the form

$$U'_\omega = U_\omega\, U_\delta, \tag{2.38}$$

from which the effective lepton mixing matrix in Eq. (2.32) can be calculated. The modified lepton mixing K' is a complex non-unitary 3x3 matrix from which one must extract the three angles and three CP phases that characterize the simplest neutrino mixing parameter set. One finds that, indeed, the proposed flavon extension of the original A_4 model scheme can engender a nonzero value for the reactor mixing angle, as required by the recent neutrino oscillation data.

2.4.3 Neutrino predictions

Using the modifications to the BMV model explained above (e.g. Eq. (2.37)), we have obtained quantitative results by the numerical diagonalization of the charged-lepton mixing matrix in Eq. (2.17) with the modification in Eq. (2.37). The three mixing angles are obtained directly as:

$$\begin{aligned} \tan\theta_{12} &= |K'_{1,2}(\theta)|/|K'_{1,1}(\theta)|, \\ \sin\theta_{13} &= |K'_{1,3}(\theta)|, \\ \tan\theta_{23} &= |K'_{2,3}(\theta)|/|K'_{3,3}(\theta)|, \end{aligned} \tag{2.39}$$

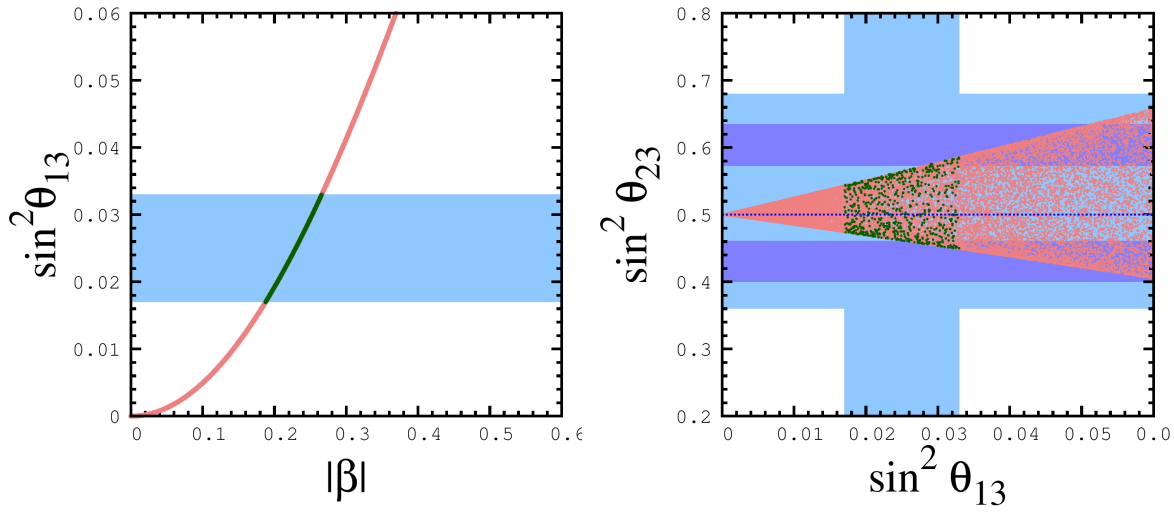

Figure 2.2: (Left) Correlation between the reactor angle $\sin^2\theta_{13}$ and the magnitude of the flavon coupling parameter $|\beta|$. (Right) Correlation between atmospheric and reactor angles for different β parameter choices. The broad vertical (horizontal) bands are the current allowed values for $\sin^2\theta_{13}$ ($\sin^2\theta_{23}$) at 3σ. In both panels the flavon phase ϕ_β has been varied continuously in the range $-\pi/2 \leq \phi_\beta \leq \pi/2$. All points in the "triangle" are allowed by the solar mixing angle θ_{12} at 3σ range, but only the green (dark) points are consistent with θ_{13} as well. Finally the two thin horizontal bands correspond to the 1σ preferred regions in the global oscillation fit of Ref. [1].

where the θ parameter has been varied randomly in the range $0 \leq \sin^2\theta \leq 1$. The scales $f_e v_1$ and M_E have also been varied randomly in the range $1 \leq f_e v_1 \leq 10^2$ GeV and $10^4 \leq M_E \leq 10^5$ GeV, leading to the results presented in Fig. 2.2. As we will see, for such values, the mixing matrix K' is well described by a unitary approximation.

As one can see from the left plot of Fig. 2.2, in order to generate a non vanishing reactor angle θ_{13}, the magnitude of the flavon coupling $|\beta|$ must be nonzero. In principle this result is independent of the phase ϕ_β. On the other hand, from the right panel of Fig. 2.2, one sees how the new coupling engenders not only a nonzero θ_{13} value, but also a restricted range for the atmospheric angle θ_{23}. If one takes at face value the hints for non-maximal θ_{23} at $1\,\sigma$ which follow from global oscillation fits [1] then one finds that the allowed regions for θ_{23} in each octant would be very narrow indeed. However, currently maximal atmospheric mixing remains perfectly consistent [38]. As one sees in Fig. 2.3, for maximal atmospheric mixing,

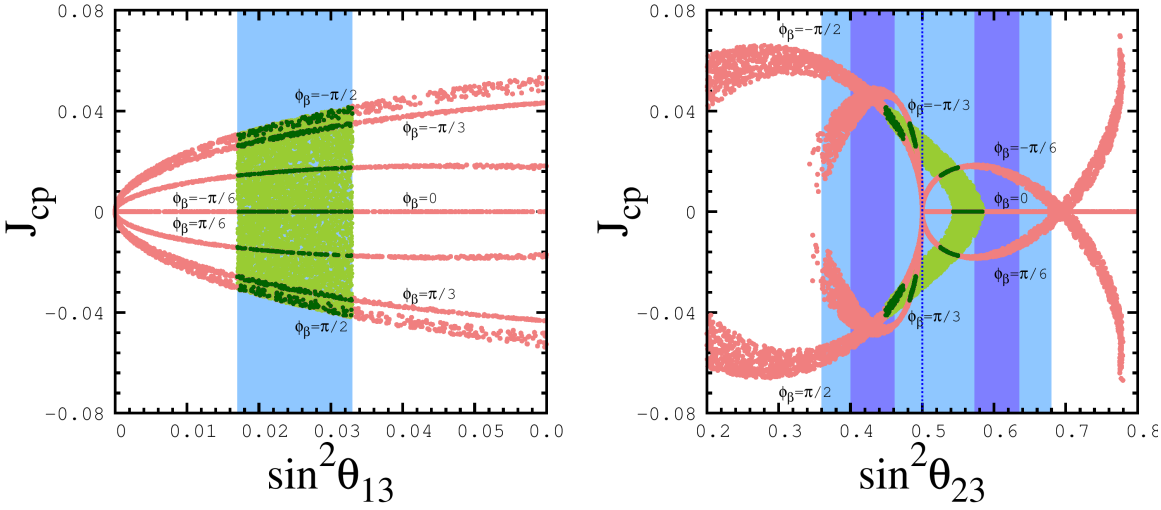

Figure 2.3: Correlation between the magnitude of the CP violation invariant J_{CP} and the two mixing angles, θ_{13} and θ_{23}, in left and right panels, respectively. Discrete set of phase values have been used in the range $-\pi/2 \leq \phi_\beta \leq \pi/2$ in steps of $\pi/6$. Random points in pink are compatible with the current 3σ range of the solar angle θ_{12}, but only the green points are compatible with the θ_{13} and θ_{23} range at $3\,\sigma$.

the flavon phase must have a non zero value, as seen in the right panel of Fig. 2.3. Note that the allowed region is modulated by the value of the β phase, ϕ_β. In other words, as one varies the value of the phase in $-\pi/2 \leq \phi_\beta \leq \pi/2$, one sweeps the triangle–shaped region indicated in the right panel of Fig. 2.2. One finds a linear correlation between the "opening angle" of the triangle and the magnitude of the continuous phase angle ϕ_β. Intermediate ϕ_β values cover the indicated shaded sub-region of the vertical strip. While all current neutrino mixing angles, including the reactor angle θ_{13}, are consistent with a real flavon coupling, allowing the latter to be complex results in a determination of the octant for θ_{23} as shown in the right panel of Fig. 2.3. A measurement of the CP violating phase would imply a determination of the octant, or vice versa. Again, continuous phase values in between the extremes lead to the half-moon-like region indicated in the right panel in Fig. 2.3.

In other to further clarify the issue of leptonic CP violation within this model, we now turn to the Dirac phase δ_{CP} associated to CP violation in neutrino oscillations. Rather than trying to extract this phase directly, we have calculated the associated Jarlskog parameter J_{CP}

$$J_{CP} = \mathcal{I}\{K^*_{e1} K^*_{\mu 3} K_{e3}\, K_{\mu 1}\}, \tag{2.40}$$

which is invariant under any conceivable phase redefinitions. Our numerical result is shown in Fig. 2.3, in which we have evaluated Eq. (2.40) for discrete values of the phase in $-\pi/2 \leq \phi_\beta \leq \pi/2$ in steps of $\pi/6$. One can see that, for $|\beta| > 0$, the invariant J_{CP} is non zero in correlation with the non zero value of the phase ϕ_β. By allowing the flavon coupling β to be complex one not only introduces CP violation in neutrino oscillations, but also selects the allowed octant of the atmospheric mixing angle θ_{23} in correspondence with the assumed values of the phase ϕ_β, which is clearly seen from right panel of Fig. 2.3. This constitutes an important prediction of the model which may be tested in the future neutrino oscillation experiments. In contrast, the Majorana phases can hardly be probed within this model since the mass spectrum is almost degenerate, so that there can never be an important destructive interference between different $0\nu\beta\beta$ amplitudes. As a result, the $0\nu\beta\beta$ decay rate is expected to be large and should be probed in current and future experiments.

2.5 Analytical understanding

In order to gain a better understanding of the proposed scheme, we now turn to an analytic approach. We have fixed the M_E scale to be 10^2 times bigger than the TeV scale and we have obtained the correlations already displayed in Fig. 2.2. The result in the left panel suggests a simple theoretical relation. Indeed, assuming K' to be nearly unitary, we are within a perturbative limit where we can solve the problem analytically, by diagonalizing the effective charged lepton mass matrix at the leading order and keeping only the terms until second order in $|\beta|$. This way we find a simple approximate result for the reactor angle given as

$$\sin^2\theta_{13} = |\beta|^2 \frac{h_1^8 - 2h_1^6\,h_3^2 + 2h_1^4\,h_3^4 - 2h_1^2\,h_2^2\,h_3^4 + h_2^4\,h_3^4 - 2h_1^2\,h_3^2(h_1^2 - h_2^2)(h_1^2 - h_3^2)\cos 2\,\phi_\beta}{2[(h_1^2 - h_2^2)(h_1^2 - h_3^2)]^2} \tag{2.41}$$

in terms of the Yukawa parameters h_i that determine the charged lepton masses through Eq. (2.21). In this way one can explain analytically the right panel of Fig. 2.2 and conclude that $\sin\theta_{13}$ can be non vanishing even if the value of the β phase is zero. In a completely

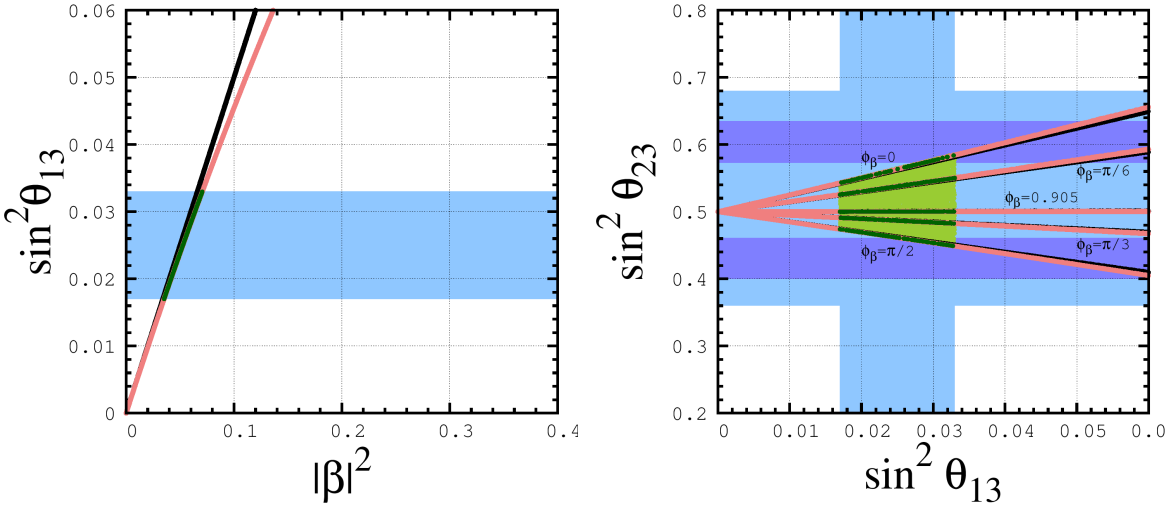

Figure 2.4: Numerical predictions for the reactor and atmospheric mixing parameters θ_{13} and θ_{23} in terms of β and its phase ϕ_β varied in steps of $\pi/6$. Approximate results are also given. Numerical results are in pink while analytical ones are in black. There is rather good agreement within the currently allowed 3σ range of the neutrino mixing angles: θ_{12}, θ_{13} and θ_{23} indicated by the blue bands. Notice that the negative values of the flavon phase corresponds to the same correlation, which is more clear from Eqs. (2.41),(2.42).

analogous procedure, we have also obtained an approximate relation for the atmospheric angle:

$$\begin{aligned}\sin^2\theta_{23} = \frac{1}{2} &+ |\beta|\frac{h_2^2}{h_2^2-h_3^2}\cos\phi_\beta \\ &+ |\beta|^2\frac{(-h_1^8+2h_1^6\,h_3^2+h_2^4\,h_3^4)(h_2^2-h_3^2)+2h_1^2(h_2^2\,h_3^6-h_2^4\,h_3^4)}{4[(h_1^2-h_2^2)(h_1^2-h_3^2)]^2(h_2^2-h_3^2)} \\ &+ |\beta|^2\frac{2h_3^2(h_1^2-h_2^2)(h_1^2-h_3^2)[h_1^2(h_2^2+h_3^2)-2h_2^2\,h_3^2]\cos 2\phi_\beta}{4[(h_1^2-h_2^2)(h_1^2-h_3^2)]^2(h_2^2-h_3^2)}\,.\end{aligned} \tag{2.42}$$

Numerically we have checked that the expansions in $|\beta|$ leading to the expressions in Eq. (2.41) and Eq. (2.42) reproduce very well the numerical results for the correlations such as, for instance, those given by the curve in the left panel of Fig. 2.2 within the current allowed range indicated by global neutrino oscillation fits and summarized by the blue bands displayed in Fig. 2.4. As we have already noted, for special values of ϕ_β the octant of θ_{23} gets determined as shown in Fig. 2.2 and Fig. 2.4.

Before concluding let us make one last comment on the size of the corrections in the neutrino sector. Within the revamped BMV model we have now introduced, the mixing

predictions have been recalculated while the squared mass splittings are given by Eq. (2.30). As we have already mentioned, the free parameter θ in the mixing corresponds to the solar angle θ_{12} for a given value of the underlying radiative corrections. In the modified BMV model, the correspondence between the free parameter and the solar angle, as a function of the radiative corrections from the soft symmetry breaking sector, is no longer the same as in the original flavon-less BMV model in Eq. (2.29). In any case, we can use the freedom in the radiative corrections to fit the solar mixing angle value within the current allowed range.

CHAPTER 3

Neutrino mass and low energy observables

One of the biggest challenges in particle physics is to unravel the nature of the dimension five operator [74]:

$$\mathcal{O}_{\text{dim}=5} = \frac{\lambda}{\Lambda} LLHH\,, \tag{3.1}$$

which is responsible for generating the observed pattern of neutrino masses. Within the see-saw mechanism [75–78] this operator arises from the tree-level exchange of heavy messenger particles. For example, in the so-called type-I see-saw these messengers are three $SU(3)_c \otimes SU(2)_L \otimes U(1)_Y$ singlet right-handed neutrinos, which must be heavy in order to account for the observed smallness of neutrino masses. Since singlets carry no gauge-anomaly, their number is theoretically unrestricted. The inverse [79] and the linear [80] see-saw schemes are both capable of realize the type-I see-saw mechanism at the TeV scale and, as a result, these schemes open the possibility for novel phenomena such as

1. lepton flavor and/or CP violating processes unsuppressed by neutrino masses [81–84],

2. effectively non-unitary lepton mixing matrix [85–87] leading to non-standard effects in neutrino propagation [88–90].

Both features arise from the non-trivial structure of the electroweak currents in see-saw schemes [1] [6, 92]. While their expected magnitude is negligible within the standard type-I see-saw, it can be sizeable in low-scale see-saw mechanisms.

In this chapter we analyze quantitatively the interplay between these two classes of processes. More precisely, we define reference parameters describing the typical magnitude of non-standard neutrino propagation effects and compare them with the constraints which arise from the searches for lepton flavor violating (LFV) processes [93–95]. For definiteness we focus on two simple realizations of the low-scale see-saw, namely the inverse and linear see-saw schemes. Non-unitarity effects may also arise from the charged lepton sector [96], leading also to lepton flavor violation. We find that unitarity violation effects in neutrino propagation at the percent level are consistent with the current bounds from lepton flavor violation searches. Therefore, their search at upcoming neutrino oscillation facilities [97] opens a window of opportunity to probe for new effects beyond the standard model.

This chapter is based on Ref. [98], and it is organized as follows: first we introduce some basic concepts in section 3.1, then we review the type-I see-saw mechanism in section 3.2.1. The low-scale inverse and linear see-saw realizations are introduced in section 3.3. General expressions for the lepton mixing unitarity violating parameters in the context of the inverse and linear see-saw schemes are defined in section 3.4. The link with the analytical expressions relating LFV decay branching ratios with the non-standard pieces of the general see-saw lepton mixing matrix is given in section 3.5. In section 3.6 we describe the parameters used in our numerical analysis, and finally in section 3.7 we present our numerical results, both for normal and inverse neutrino mass hierarchies.

3.1 Preliminaries

Based on the property that the Lorentz group, $SO(3,1)$, is locally isomorphic to $SU(2) \times SU(2)$, each representation of $SU(2)$ can be labeled by 'spin'. Thus, the Lorentz group can be labeled by (a,b), where $a,b = 1/2, 1, 3/2, \ldots$ [99, 100]. The simplest fermion representation, $(1/2, 0)$ corresponds to a Weyl spinor χ. We can construct a Lorentz invariant mass term for

[1] They are generic in electroweak gauge models that mix fermions of different isospin in the weak currents [91].

the Weyl spinor:

$$\mathcal{L} = \frac{1}{2} M(\chi^T \, i\sigma_2 \, \chi + h.c.) \tag{3.2}$$

with the Pauli matrices σ_i. To show the invariance of the mass term in Eq. (3.2), we apply a Lorentz transformation $\mathcal{T} = e^{-\frac{i}{2}\sigma\cdot\theta}$ over the spinor χ and recalculate the mass term:

$$\chi^T \, i\sigma_2 \, \chi \to \chi^T \mathcal{T}^T \, i\sigma_2 \, \mathcal{T}\chi \; ,$$

Expanding the indexes in the last expression we can show that:

$$\mathcal{T}^T \, i\sigma_2 \, \mathcal{T} = i\sigma_2$$

where $\det\mathcal{T} = 1$ has been used. Therefore, the mass term in Eq. (3.2) is Lorentz invariant. Finally, we want to apply a unitary transformation U over the Weyl spinor. This transformation represents another symmetry different from Lorentz, under which the mass term in Eq. (3.2) will transform as:

$$\chi^T \, i\sigma_2 \, \chi \to \chi^T U^T \, i\sigma_2 \, U\chi = \chi^T \, i\sigma_2 \, U^T U\chi \; . \tag{3.3}$$

This term is invariant provided that $U^T U = 1$, which implies that U is real. Then we have shown that χ cannot carry a global or local $U(1)$ charge (it cannot transform under a complex or pseudoreal representation [99, 100]). Therefore, the χ spinor can not represent an electrically charged fermion. In the case of neutrinos, the *Majorana mass term* in Eq. (3.2) is allowed but it necessarily violates lepton number.

In the case of the Dirac mass term:

$$\mathcal{L} = -m\bar{\psi}\psi \, , \tag{3.4}$$

where ψ corresponds to the Dirac spinor, we can write the four-component Dirac spinor in terms of two Weyl spinors χ, ξ as [6]:

$$\psi = \begin{pmatrix} \chi \\ i\sigma_2 \xi^* \end{pmatrix} \; . \tag{3.5}$$

Defining the Dirac gamma matrices in the Weyl basis:

$$\gamma^0 = \begin{pmatrix} 0 & 1 \\ 1 & 0 \end{pmatrix} \quad \gamma^i = \begin{pmatrix} 0 & \sigma^i \\ -\sigma^i & 0 \end{pmatrix} \quad \gamma_5 = \begin{pmatrix} -1 & 0 \\ 0 & 1 \end{pmatrix} \quad , \tag{3.6}$$

we can write the Dirac mass term as:

$$\mathcal{L} = m(\xi^T\, i\sigma_2\, \chi - \chi^\dagger\, i\sigma_2\, \xi^*), \tag{3.7}$$

where the definition $\bar{\psi} = \psi^\dagger\gamma^0$ was used.

Using a single Weyl spinor, we can write the Majorana four-component spinor as:

$$\psi_M = \begin{pmatrix} \chi \\ \epsilon\chi^* \end{pmatrix}\,, \tag{3.8}$$

implying somehow that Weyl spinors are the most economical way to describe the neutrino masses.

The charged conjugation operator in the Weyl representation of the Dirac matrices is given by:

$$C = \begin{pmatrix} -i\sigma_2 & 0 \\ 0 & i\sigma_2 \end{pmatrix}\,, \tag{3.9}$$

what allows us to define the conjugate Dirac spinor as:

$$\psi^c \equiv C\gamma^0\psi^* = \begin{pmatrix} \xi \\ \epsilon\chi^* \end{pmatrix}\,. \tag{3.10}$$

Comparing the right hand side of Eq. (3.10) with Eq. (3.5) we can notice that the charged conjugation operator interchanges the two Weyl components. In the case of the Majorana four-component spinor in Eq. (3.8) we can notice that $\psi^c_M = \psi_M$, what is known as the Majorana condition [100].

For future reference, it is useful to write the Majorana mass term in Eq. (3.2) in terms of the usual Dirac spinor ψ. To obtain the two separate Weyl spinor components we can use the chiral projection operators $P_{L,R} = (1 \mp \gamma^5)/2$ such that:

$$P_L\psi \equiv \psi_L = \begin{pmatrix} \chi \\ 0 \end{pmatrix}\,. \tag{3.11}$$

Thus we can finally write:

$$\mathcal{L} = -\frac{1}{2}m(\psi_L^T C\psi_L + h.c.)\,. \tag{3.12}$$

It is also useful to write the Dirac Lagrangian for a free-particle:

$$\mathcal{L} = \bar{\psi}(i\gamma^\mu \partial_\mu - m)\psi \,, \tag{3.13}$$

using the two component spinors. Because the mass term was already introduced in Eq. (3.7), we can write the kinetic part as:

$$\begin{aligned}
&\begin{pmatrix} \chi^\dagger & 0 \end{pmatrix} \begin{pmatrix} i\bar{\sigma}^\mu \partial_\mu & 0 \\ 0 & i\sigma^\mu \partial_\mu \end{pmatrix} \begin{pmatrix} \chi \\ 0 \end{pmatrix} + \begin{pmatrix} 0 & -\xi^T i\sigma_2 \end{pmatrix} \begin{pmatrix} i\bar{\sigma}^\mu \partial_\mu & 0 \\ 0 & i\sigma^\mu \partial_\mu \end{pmatrix} \begin{pmatrix} 0 \\ i\sigma_2 \xi^* \end{pmatrix} \\
&= \chi^\dagger i\bar{\sigma}^\mu \partial_\mu \chi - \xi^T (i\sigma_2)(i\sigma^\mu)(i\sigma_2)\partial_\mu \xi^* \\
&= \chi^\dagger i\bar{\sigma}^\mu \partial_\mu \chi + \xi^\dagger i\bar{\sigma}^\mu \partial_\mu \xi \,.
\end{aligned}$$

Here we used the Peskin notation: $\sigma^\mu = (1, \vec{\sigma})$, $\bar{\sigma}^\mu = (1, -\vec{\sigma})$. In the last expression, the properties of the σ_i matrices and some spinor algebra [101] were used. Finally, the Dirac free-particle Lagrangian in two component notation is given by:

$$\mathcal{L} = \chi^\dagger i\bar{\sigma}^\mu \partial_\mu \chi + \xi^\dagger i\bar{\sigma}^\mu \partial_\mu \xi - m(\chi^\dagger i\sigma_2 \xi^* + \text{h.c}) \,. \tag{3.14}$$

After a unitary change of variables [6]:

$$\begin{aligned}
\chi &= \frac{1}{\sqrt{2}}(\rho_2 + i\rho_1), \\
\xi &= \frac{1}{\sqrt{2}}(\rho_2 - i\rho_1),
\end{aligned}$$

the Dirac Lagrangian gets separated in two pieces:

$$\mathcal{L} = \sum_a^2 \left[\rho_a^\dagger i\bar{\sigma}^\mu \partial_\mu \rho_a - \left(\frac{m}{2} \rho_a^T i\sigma_2 \rho_a + \text{h.c} \right) \right] \,, \tag{3.15}$$

what allow us to identify a Dirac particle as a sum of two Majorana particles with the same mass.

3.2 Neutrino mass in the Electroweak theory

In order to generate neutrino masses, a summary of possible modifications of the SM are [6, 102]:

- Higgs sector extension.

- lepton sector extension.
- both Higgs and lepton sector extensions.

Nowadays, extensions with singlet fermions under the SM gauge group are known as type-I see-saw, while extensions with a Higgs triplet are known as type-II see-saw. Another popular extension with lepton triplets is possible and it is known as type-III see-saw [103] (see below).

Here we will mainly focus on the popular type-I see-saw and, as mentioned before we are mainly interested in the low-scale see-saw mechanism as a generalization of this scheme. This will require a SM extension adding extra singlet fermions. With the addition of $SU(2)_L$-singlet left-handed [2] spinor fields ρ_{La} with hypercharge $Y = 0$, it is possible to write a Majorana mass term as:

$$-\sum_{a,b} g'_{ab}\, \rho_{La}^T\, C\, \rho_{Lb} + \text{h.c}\ . \tag{3.16}$$

Together with the component of the SM field l, a Dirac mass term can be written through the Yukawa term [6]:

$$\sum_{a,b} \tilde{g}_{ab} \bar{l}_a\, i\sigma_2 \phi^* C\, \bar{\rho}_{Lb}^T + \text{h.c.} \tag{3.17}$$

Here, ϕ corresponds to the SM Higgs field. A general theory of massive neutrinos should consider the presence of *both* terms in Eq. (3.16) and Eq. (3.17). In this case the resulting neutrino mass matrix in general is a $N \times N$ matrix with $N > 3$. In the next sections we analyze the structure of this matrix in the high and low-scale type-I see-saw schemes.

In the case of the type-II see-saw, it is necessary to add a complex Higgs triplet h with hypercharge $Y = 2$. The triplet can be written as:

$$h = \begin{pmatrix} h^{(+)} & \sqrt{2}h^{(++)} \\ \sqrt{2}h^{(0)} & -h^{(+)} \end{pmatrix}\ , \tag{3.18}$$

and the Yukawa terms in the weak Lagrangian are given by [6]:

$$-\frac{1}{2}\sum_{a,b} g_{ab}\, l_a^T C\, i\sigma_2\, h\, l_b + \text{h.c}\,, \tag{3.19}$$

[2] It is equivalent to add new right handed singlet neutrinos that will generate a Dirac mass term as the other fermions of the SM and also a Majorana mass term $-M/2(\psi_R^T C \psi_R)$ that is exactly the one in Eq. (3.2) but with the ξ Weyl spinor.

where l corresponds to the SM lepton doublet. After the triplet gets a vev, it will generate a Majorana mass term of the same kind as in Eq. (3.12). The new triplet h will modify the SM gauge boson masses and therefore the ρ parameter. Some conditions should be fulfilled by the Higgs triplet, in particular:

$$\langle h^{(0)} \rangle = -\mu_h \frac{\langle \phi^{(0)} \rangle^2}{M_h^2} \tag{3.20}$$

that comes from the minimization of the scalar potential [104]. Thus, neutrino masses are proportional to the Higgs triplet vev $\langle h^{(0)} \rangle$ and are small if the Higgs triplet mass is high enough, which implies a new large scale in the scalar sector [104].

Finally, in the type-III see-saw a $SU(2)$ triplet fermion T_F with hypercharge $Y = 0$ is introduced. We can write the Yukawa interaction as [105]:

$$\Delta\mathcal{L}(T_F) = y_T \, l^T \, C\sigma_2 \, \vec{\sigma} \cdot \vec{T}_F \phi + M_T \vec{T}_F \, C \, \vec{T}_F \, , \tag{3.21}$$

where the first term is a Dirac mass term, equivalent to the one in Eq. (3.17). For simplicity, Eq. (3.21) has neither family indexes nor index counting the number of triplets [105]. After the Electroweak Symmetry Breaking (EWSB) the neutrino masses are given by:

$$m_\nu \approx -y_T^T \frac{1}{M_T} y_T \, v^2. \tag{3.22}$$

As we will see for the type-I see-saw case, here the neutrino masses are also small due to the large M_T.

Along this chapter we will focus on the Type-I see-saw and its generalized low scale versions such as the inverse [79] and linear see-saw [80, 106].

3.2.1 The standard type-I see-saw

In general see-saw schemes the neutrino mass matrix M_ν can be decomposed in sub-blocks involving the standard as well as singlet neutrinos as follows [6]:

$$M_\nu = \begin{pmatrix} M_1 & M_D \\ M_D^T & M_2 \end{pmatrix} \, , \tag{3.23}$$

in the basis $\nu,\ \nu^c$, where the blocks $M_1 \equiv M_L$ and $M_2 \equiv M_R$ are symmetric matrices. The M_1 block corresponds to the Majorana mass from the Yukawa term in the Lagrangian that describes the Higgs triplet interaction with the SM neutrinos in Eq. (3.19). The M_2 block corresponds to the Majorana mass in Eq. (3.16) while the M_D block is the Dirac mass from the usual Yukawa interaction between the SM Higgs and the extra states in Eq. (3.17).

Though the number of singlets is arbitrary, here we take an equal number of SU(2) doublets and singlets, and consider the simplest type-I see-saw, where no Higgs triplet is present, so the upper left sub-matrix is $M_1 = 0$ in Eq. (3.23) [6] [3]. Neutrino masses arise by diagonalizing the matrix of Eq. (3.23),

$$\text{diag}\{\tilde{m}_i\} = U^T\, M_\nu\, U = \text{real, diagonal}\ , \tag{3.24}$$

through the transformation U connecting the weak states to the light and heavy mass eigenstates. We adopt a polar decomposition for U as it is shown in appendix C. In the diagonalization of the neutrino mass matrix in Eq. (3.23) we find that the S matrix in Eq. (C.7) is given by:

$$i\, S^* = -M_D\, M_R^{-1}. \tag{3.25}$$

so that, we determine U in Eq. (C.4) as:

$$U = \begin{pmatrix} \left(I - \frac{1}{2} M_D^* (M_R^*)^{-1}\, M_R^{-1} M_D^T\right) V_1 & M_D^* (M_R^*)^{-1}\, V_2 \\ -M_R^{-1}\, M_D^T\, V_1 & \left(I - \frac{1}{2} M_R^{-1}\, M_D^T\, M_D^*\, (M_R^*)^{-1}\right) V_2 \end{pmatrix} + O(\epsilon^3), \tag{3.26}$$

leading to the effective light neutrino mass matrix in Eq. (C.9), here given by:

$$m_\nu \approx -M_D M_R^{-1} M_D^T\ . \tag{3.27}$$

This is the so called type-I see-saw mechanism. The smallness of neutrino masses follows naturally from the heaviness of the $SU(2)_L$ singlet neutrino states ν_i^c.

3.3 Low scale see-saw mechanism

Most see-saw descriptions assume equal number of doublets and singlets, $n = m = 3$. However, since singlets carry no gauge-anomaly, their number is arbitrary [6, 92]. In this chapter

[3] In this case light neutrinos get mass only as a result of the exchange of heavy gauge singlet fermions.

we will consider not only the case $(n, m) = (3, 3)$ just described, but also the inverse and linear see-saw schemes, which belong to the (3,6) class, see below.

3.3.1 Lepton number conserving case

In order to present the link between neutrino masses and the lepton number symmetry, we will introduce a toy model without reference to any gauge group [107]. It introduces three left-handed neutral fermions ν_L, N_L, S_L (with their right handed antiparticles) and two scalars ϕ and χ. The Yukawa couplings are given by:

$$\mathcal{L} = a\,\overline{\nu}_L N_R \phi + b\,\overline{N}_R S_L \chi + \text{h.c}\,. \tag{3.28}$$

Assuming that one of the three global $U(1)$ symmetries, corresponding to the lepton number, is unbroken after the two scalars develop a vev, the mass matrix can be written as [107]:

$$\begin{pmatrix} 0 & a\langle\phi\rangle & 0 \\ a\langle\phi\rangle & 0 & b\langle\chi\rangle \\ 0 & b\langle\chi\rangle & 0 \end{pmatrix}, \tag{3.29}$$

in the Majorana form. After the matrix diagonalization we get:

$$\begin{aligned} m_1 &= 0 \\ m_{2,3} &= \pm\sqrt{b^2\langle\chi\rangle^2 + a^2\langle\phi\rangle^2}\ . \end{aligned} \tag{3.30}$$

In the left-right symmetric model $SU(2)_L \times SU(2)_R \times U(1)_{B-L}$ we can identify $\langle\chi\rangle$ with the breaking scale of $SU(2)_R$, which is typically assumed to be $\langle\chi\rangle \geq \langle\phi\rangle$. In this toy model, from Eq. (3.30), we have found that the left-handed neutrino is massless and we have two Majorana states with a degenerate mass corresponding to one Dirac neutrino. Neutrinos are massless because we have imposed the conservation of lepton number.

The scheme shown here can be realized within a $SO(10)$ framework [107]. From the phenomenological point view, for the neutrino masses we just need to replace $a\langle\phi\rangle$ by m_D and $b\langle\chi\rangle$ by M, representing mass matrices where the equivalent of Eq. (3.30) is given by:

$$\begin{aligned} m_1 &= 0 \\ m_{2,3} &= \pm\left\{\frac{1}{2}\left[m_D^T m_D^* (M^\dagger)^{-1} + \text{T.T}\right] + \frac{1}{2}\left(M + M^T\right)\right\}\ . \end{aligned} \tag{3.31}$$

Here we have three massless Weyl neutrinos while the other six neutral two component leptons combine exactly into three heavy Dirac fermions [108]. The T.T notation in Eq. (3.31) means transposed term. An interesting feature of this scheme is that neutrino masses are zero due to a symmetry. In what follows we will exploit further this idea but within realistic models. We will produce viable low–scale alternatives to the usual type–I see-saw mechanism by breaking the lepton number symmetry conserved in the example above.

3.3.2 Inverse see-saw mechanism

As an alternative to the simplest $SU(3)_c \otimes SU(2)_L \otimes U(1)_Y$ type-I see-saw model, it has long been proposed extending the see-saw lepton content from $(3,3)$ to $(3,6)$, by adding three extra $SU(2)$ singlets [79] [4], S_i, charged under the $U(1)_L$ global lepton number in the same way as the doublet neutrinos ν_i, i.e. $L = +1$. After EWSB one gets the following neutrino mass matrix

$$M_\nu = \begin{pmatrix} 0 & M_D & 0 \\ M_D^T & 0 & M \\ 0 & M^T & \mu \end{pmatrix}, \tag{3.32}$$

in the basis $(\nu,\ \nu^c,\ S)$, where the three ν_i^c have $L = -1$. Note that $U(1)_L$ is broken only by the nonzero $\mu_{ij} S_i S_j$ mass terms. Generalizing the perturbative expansion method in Ref. [92], already used in section 3.2.1, one finds that the mass matrix in Eq. (3.32) can be block diagonalized as

$$\mathcal{U}^T \cdot M_\nu \cdot \mathcal{U} = \text{block diag} \tag{3.33}$$

[4] For simplicity we add the isosinglet pairs sequentially, though two pairs would suffice to account for neutrino oscillations.

with

$$\mathcal{U} \approx \begin{pmatrix} I & 0 & 0 \\ 0 & \frac{1}{\sqrt{2}}I & -\frac{1}{\sqrt{2}}I \\ 0 & \frac{1}{\sqrt{2}}I & \frac{1}{\sqrt{2}}I \end{pmatrix} \times \begin{pmatrix} I - \frac{1}{2}S_1\, S_1^\dagger & 0 & iS_1 \\ 0 & I & 0 \\ iS_1^\dagger & 0 & I - \frac{1}{2}S_1^\dagger\, S_1 \end{pmatrix}$$
$$\times \begin{pmatrix} I - \frac{1}{2}S_2\, S_2^\dagger & iS_2 & 0 \\ iS_2\dagger & I - \frac{1}{2}S_2^\dagger\, S_2 & 0 \\ 0 & 0 & I \end{pmatrix}, \tag{3.34}$$
$$\approx \begin{pmatrix} I & iS_2 & iS_1 \\ -i\frac{1}{\sqrt{2}}\left(S_1^\dagger - S_2^\dagger\right) & \frac{1}{\sqrt{2}}I & -\frac{1}{\sqrt{2}}I \\ i\frac{1}{\sqrt{2}}\left(S_1^\dagger + S_2^\dagger\right) & \frac{1}{\sqrt{2}}I & \frac{1}{\sqrt{2}}I \end{pmatrix} + O(\epsilon^2)\ ,$$

where S_1 and S_2 are 3×3 matrices. In the limit $\mu \to 0$ we have $S_1 = S_2 = S$ with

$$iS^* = -\frac{1}{\sqrt{2}} m_D \left(M^T\right)^{-1} \sim \epsilon. \tag{3.35}$$

With this diagonalization matrix the light neutrino mass obtained from type-I see-saw is

$$m_\nu \approx M_D M^{T^{-1}} \mu M^{-1} M_D^T. \tag{3.36}$$

Note that, in the limit $\mu \to 0$, the lepton number symmetry is recovered, making the three light neutrinos strictly massless. Thus, the smallness of neutrino masses follows in a natural way, in the 't Hooft sense [109], as it is protected by $U(1)_L$. For completeness, the heavy masses are given by:

$$m_{2,3} = \frac{1}{2}\mu \pm \left\{ \frac{1}{2}\left[m_D^T m_D^* (M^\dagger)^{-1} + \text{T.T} \right] + \frac{1}{2}\left(M + M^T\right) \right\}, \tag{3.37}$$

where we have neglected terms proportional to m_ν. Notice that we recover the expression in Eq. (3.31) when $\mu \to 0$. One sees also that $\mathcal{U}$ consists of a maximal block rotation, corresponding to the Dirac nature of the three heavy leptons made-up of ν^c and S in the limit as $\mu \to 0$, and two rotations similar to Eq. (C.4) for the minimal type-I see-saw case considered in the previous section. Note also that the idea behind the so-called *inverse see-saw* model can also be realized for other extended gauge groups see for instance Refs. [106, 107, 110]. Moreover, in specific models, the smallness of μ may be dynamically generated [111].

3.3.3 Linear see-saw mechanism

An alternative see-saw scheme that can also be realized at low-scale is called *linear see-saw*, and it has been suggested as arising from a particular $SO(10)$ unified model [80] (for other possible constructions see [106, 112]). Once the extended gauge structure breaks down to the standard $SU(3)_c \otimes SU(2)_L \otimes U(1)_Y$ one gets a mass matrix of the type

$$M_\nu = \begin{pmatrix} 0 & M_D & M_L \\ M_D^T & 0 & M \\ M_L^T & M^T & 0 \end{pmatrix}, \tag{3.38}$$

in the same basis (ν, ν^c, S) used in Sec. 3.3.2. Although theoretical consistency of the model requires extra ingredients, such as Higgs scalars to generate the M_L and $M \equiv M_R$ entries, here we consider just the simplest phenomenological scheme defined by the effective mass matrix in Eq. (3.38), as it suffices to describe the processes we are interested in.

The block-diagonalization proceeds in a similar way as to the inverse see-saw case, in fact, for sufficiently small values of $M_L\, M^{-1}$, the relations in Eq. (3.34) and Eq. (3.35) are the same in both schemes. One finds that the effective light neutrino mass is now given by

$$m_\nu \approx M_D (M_L M^{-1})^T + (M_L M^{-1}) M_D^T. \tag{3.39}$$

One sees that, in contrast to the "usual" see-saw relations for the effective light neutrino mass, Eqs. (3.27) and (3.36), the previous expression is linear in the Dirac neutrino Yukawa couplings, hence the name *linear see-saw*. Notice also that lepton number, defined as in the previous model, is broken only by the terms $M_L\, \nu\, S$. As a result one sees that, in the limit $M_L \to 0$, the lepton number symmetry is recovered, making the three light neutrinos strictly massless. Again, as in the previous case, the smallness of neutrino masses follows in a natural way [109], as it is protected by $U(1)_L$.

3.4 Unitarity deviation of the lepton mixing matrix

The effective lepton mixing matrix $K_{i\alpha}$ characterizing the charged current weak interaction of mass-eigenstate neutrinos in any type of see-saw model has been fully characterized in Ref. [6]. It can be expressed in rectangular form as:

$$\mathcal{L} \supset i \frac{g}{\sqrt{2}} W_\nu \bar{l}_b K_{b\alpha} \gamma_\mu \nu_{\alpha L} + h.c.\ , \tag{3.40}$$

where

$$K_{b\alpha} = \sum_{c=1}^{n} \Omega^{*}_{cb} U_{c\alpha} \,. \tag{3.41}$$

Here, Ω is the 3 by 3 unitary matrix that diagonalizes the charged-lepton mass matrix, while U is the unitary matrix that diagonalizes the (higher-dimensional) neutrino mass matrix characterizing the type-I see-saw mechanism of interest. We may write the K matrix as follows

$$K = (K_L, K_H) \,, \tag{3.42}$$

where K_L is a 3 by 3 matrix and K_H is a 3 by 6 matrix. While the rows of the K matrix are unit vectors, since $K \cdot K^{\dagger} = I$, the blocks K_L and K_H are not unitary. For our purposes we can take the charged lepton mass matrix in its diagonal form [5] so that $\Omega \to 1$. From Eq. (3.26) we obtain:

$$\begin{aligned} K_L &= \left(I - \frac{1}{2} M_D^{*} (M^{*})^{-1} (M)^{-1} M_D^{T} \right) V_1 \,, \\ K_H &= \left(M_D^{*} (M^{*})^{-1} \right) V_2 . \end{aligned} \tag{3.43}$$

In order to establish a simple comparison with recent literature we parametrize the deviation from unitarity as [114]

$$K_L \equiv (1 - \eta) V_1 . \tag{3.44}$$

Then for the simplest high-scale type-I see-saw, the deviation from unitarity characterizing the mixing of light neutrinos, is given by:

$$\eta \sim \frac{1}{2} \epsilon^{*} \epsilon^{T} \approx \frac{1}{2} M_D^{*} (M^{*})^{-1} (M)^{-1} M_D^{T} . \tag{3.45}$$

Barring *ad hoc* fine-tuning, it follows that for this case one expects negligible deviation from unitarity, namely $\epsilon \approx 10^{-10}$ and so $\eta \approx 10^{-20}$.

From now on we will focus on the low-scale type-I see-saw schemes discussed in Secs 3.3.2 and 3.3.3, inverse and linear see-saw, respectively. Generalizing the above discussion to these cases one finds

$$K_L = \left[I - \frac{1}{2} \left(M_D^{*} ((M^{T})^{*})^{-1} (M)^{-1} M_D^{T} \right) \right] V_1 \,. \tag{3.46}$$

Hence the parameters characterizing the deviation from unitarity, analogous to Eq. (3.45) are given by [6],

$$\eta^{I,L} \approx \frac{1}{2} \left(M_D^{*} ((M^{T})^{*})^{-1} (M)^{-1} M_D^{T} \right) , \tag{3.47}$$

[5] This may be automatic in the presence of suitable discrete flavor symmetries as in [113].

[6] For a recent study of unitarity violation in see-saw schemes see, for instance, Ref. [114].

mode	upper limit (90% C.L.)	year	Exp./Lab.	Ref.
$\mu^+ \to e^+\gamma$	5.7×10^{-13}	2013	MEG / PSI	[116]
$\mu^+ \to e^+e^+e^-$	1.0×10^{-12}	1988	SINDRUM I / PSI	[117]
μ^- Ti $\to e^-$ Ti	6.1×10^{-13}	1998	SINDRUM II / PSI	[118]
μ^- Au $\to e^-$ Au	7×10^{-13}	2006	SINDRUM II / PSI	[119]
$\tau \to e\gamma$	3.3×10^{-8}	2009	BABAR/SLAC	[120]
$\tau \to \mu\gamma$	4.4×10^{-8}	2009	BABAR/SLAC	[120]
$\tau \to 3e$	2.7×10^{-8}	2010	BELLE/KEK	[121]
$\tau \to 3\mu$	2.1×10^{-8}	2010	BELLE/KEK	[121]

Table 3.1: Present limits on rare μ and τ decays. Summary from Ref. [115] and [122].

which holds for both the type-I inverse and linear see-saw mechanisms. These parameters characterize the corresponding unitarity deviations in the light-active 3×3 sub-block of the lepton mixing matrix.

3.5 Lepton flavor violation

LFV has already been observed in neutrino oscillations but not in any process involving charged leptons so far. In the SM, family flavor is conserved, and therefore an observation of any charged LFV process will be a discovery of new physics. The models we consider in this thesis extend the SM predicting an important enhancement of LFV process and in many cases as large as the current experimental bounds. There has been an experimental effort in measuring these LFV processes, leading to a reduction of the allowed parameter space in many models. The observation of charged LFV processes might also help to discriminate between several extensions of the SM [115].

Charged LFV transitions between e, μ, and τ, can be observed in purely leptonic processes, in nuclei transition processes and in the case of the τ also in semileptonic processes. As shown in table 3.1, charged LFV processes involving muons have the highest experimental sensitivities, although τ decay starts to become competitive as well [115]. From table 3.1

we can see that the most restrictive processes are the ones from muon decay. Theoretical calculations of these process are in general model dependent. In type-I see-saw models, the $l_i \to l_j\gamma$ process is radiatively induced by neutrino interchange as shown in Fig. 3.1. In the case of $\mu - e$ conversion in nuclei, several diagrams contribute to the process and they can be classified by photonic and non-photonic. In the context of the inverse see-saw model, LFV processes get contributions from penguin photon, Z-exchange and box diagrams [123]. Recently in the context of the type-I see-saw, $\mu - e$ conversion has been reviewed [124]. Depending on the model, the $\mu \to 3e$ process receives contributions only from tree level or from several penguin contributions from the photon, Z, Higgs bosons and box diagrams. For instance, in the context of a variation of the type-III see-saw, a variation of the inverse see-saw model has been implemented in such a way that the LFV process $\mu \to 3e$ occurs at tree level [96]. In the context of supersymmetry with right-handed neutrinos, the charged LFV processes already mentioned, have been studied in the seminal paper Ref. [125].

The fact that neutral current couplings of charged leptons are flavor diagonal implies that the decay processes $l_i \to l_j l_k l_r$ are suppressed by a factor of α_{QED} with respect to the radiative processes, hence they are less restrictive. In the case of the $\mu - e$ conversion in nuclei, explicit calculations [123] indicate that, given the nuclear form factors, current $\mu - e$ conversion sensitivities are effectively lower than those of the $\mu \to e\gamma$ decay. However the upcoming generation of nuclear conversion experiments aims at a substantial improvement. In this study of the low scale see-saw we will focus on the radiative leptonic decays.

3.5.1 Radiative leptonic decays

We now turn to the lepton flavor violating processes that would be induced at one loop in type-I see-saw models, as a result of the mixing of $SU(2)$ doublet neutrinos with singlet neutral heavy leptons. The latter breaks the Glashow-Illiopoulos-Maiani cancellation mechanism [126], enhancing the rates for the loop-induced lepton flavor violating process illustrated in Fig. 3.1. The $l_i \to l_j\gamma$ decay process is induced through the exchange of the nine neutral leptons coupled to the charged leptons in the charged current, namely the three light neutrinos as well as the six sub-dominantly coupled heavy states [81, 127–130]. The resulting decay branching ratio is

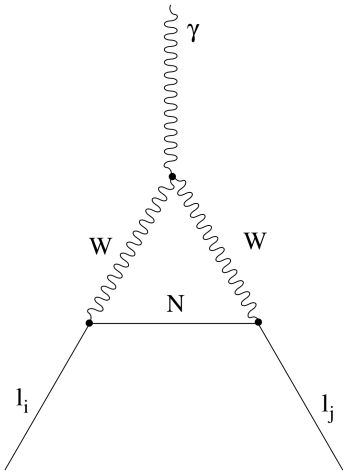

Figure 3.1: Feynman diagram for $\mu \to e\gamma$ decay in see-saw models.

given by

$$Br(l_i \to l_j \gamma) = \frac{\alpha_W^3 s_W^2}{256\pi^2} \frac{m_{l_i}^5}{M_W^4} \frac{1}{\Gamma_{l_i}} |G_{ij}^W|^2 \ , \tag{3.48}$$

where we use the explicit analytic form of the loop-functions [129],

$$\begin{aligned} G_{ij}^W &= \textstyle\sum_{k=1}^{9} K_{ik}^* K_{jk} G_\gamma^W \left(\frac{m_{N_k}^2}{M_W^2} \right) \ , \\ G_\gamma^W(x) &= \frac{1}{12(1-x)^4} (10 - 43x + 78x^2 - 49x^3 + 18x^3 \ln x + 4x^4) \end{aligned} \tag{3.49}$$

and it is presented in Fig. 3.2 for the inverse and linear see-saw. The difference between the two models follows from the different dependence with the lepton number violating parameters that characterize these two low-energy type-I see-saw realizations. One sees that the branching ratios may easily exceed the current limits. This reflects an important feature of low-scale see-saw models, namely, that lepton flavor violation as well as leptonic CP violation proceed even in the limit of massless neutrinos [81–84] . Unsuppressed by the smallness of neutrino mass, the expected rates are sizeable. The corresponding radiative LFV decays $\tau \to e\gamma$ and $\tau \to \mu\gamma$ are not as constraining as $\mu \to e\gamma$.

3.6 Numerical analysis

In order to perform our numerical calculations it is convenient to generalize the Casas-Ibarra parametrization [131] to the inverse and linear type-I see-saw schemes. For simplicity we will assume real lepton Yukawa couplings and mass entries.

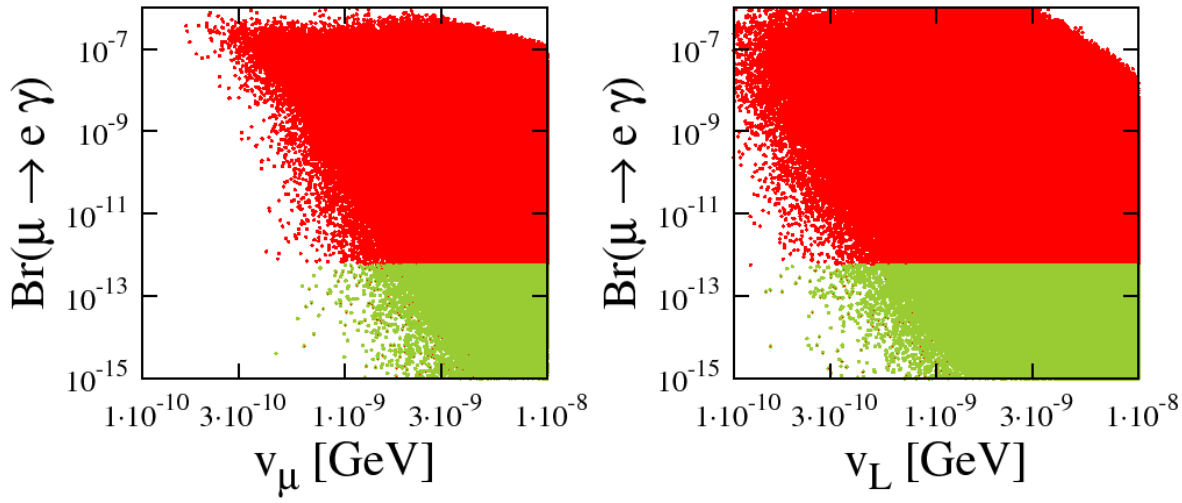

Figure 3.2: $Br(\mu \to e\gamma)$ versus the lepton number violation scale: v_μ for the inverse see-saw (left panel), and v_L for the linear see-saw (right panel). In both cases one assumes normal hierarchy and the parameters are varied as explained in Sec. 3.6. The red (dark) points are excluded by the current limit from MEGA collaboration [116] while the green (light) points are compatible with MEGA limit.

3.6.1 Inverse type-I Seesaw

First note that one has always the freedom to go to the basis where the 3×3 gauge-singlet block M is taken diagonal. For real m_D matrix elements, we have in total 18 parameters, nine characterizing m_D, three characterizing M, plus six from the μ matrix.

The Dirac neutrino mass matrix may be rewritten as

$$m_D = V_1 \,\mathrm{diag}(\sqrt{\tilde{m}_i})\, R^T\, (\sqrt{\mu})^{-1}\, \mathrm{diag}(M_i^T) \tag{3.50}$$

where V_1 is (approximately) the mixing matrix determined in oscillation experiments [52] and $\tilde{m}_i$ are the three light neutrino masses. On the other hand, the arbitrary real orthogonal 3×3 matrix R and the arbitrary 3×3 real matrix M are parameters characterizing the model. This parametrization for the inverse type-I see-saw is similar to the one given in Ref. [128]. In order to further reduce the number of degrees of freedom, we will make the "minimal flavor violation hypothesis" [7] which consists in assuming that flavor is violated only in the "standard"

[7] This simplifying assumption suffices to illustrate the points made in this chapter. For alternative minimal flavor violation definitions see Refs. [132–134].

Dirac Yukawa coupling. Under this simplification the 3×3 matrix μ must be also diagonal, reducing the parameter count from a total of 18 down to 15. These include the three light neutrino masses, and the three neutrino mixing angles contained in V_1, together with the nine model-defining parameters, that may be taken as three parameters from the R matrix, three from the μ matrix, plus three parameters characterizing M.

We have performed a random scan over the 3σ allowed region for the lightest mass and oscillation parameters, the three angles and the three masses in V_1 and $\tilde{m}_i$, respectively. For the scan over oscillation parameters we have used the determinations given in [2], and for the lightest mass parameter we took the cosmological bound on the sum of the neutrino masses from [10]. We parametrize the real orthogonal matrix R as a product of three rotations, marginalizing over the three angles from $0 - 2\pi$ values. We have also fixed the upper value of the Dirac mass matrix to $(m_D)_{ij} < 175\,\text{GeV}$ to be consistent with perturbativity of the theory. The remaining six free parameters, from μ and M matrices, are scanned as a perturbation from the identity matrix in the following way:

$$\begin{aligned} \mu_{ii} &= v_\mu \, (1 + \varepsilon_{ii}) \ , \\ M_{ii} &= v_M \, (1 + \varepsilon'_{ii}) \, , \end{aligned} \tag{3.51}$$

where $|\varepsilon| \sim 5 \times 10^{-1}$. The parameter v_M setting the M-scale was fixed to $1\,\text{TeV}$, while the v_μ scale was scanned in the range $(0.1 - 10)\,\text{eV}$. The two scales $v_{\mu,M}$ are consistent with the observed neutrino masses.

3.6.2 Linear type-I Seesaw

Similarly, for the linear see-saw case we can parametrize the Dirac neutrino mass matrix as follows,

$$m_D = V_1 \text{diag}\{\sqrt{m_i}\}\, A^T \text{diag}\{\sqrt{m_i}\}\, V_1^T \left(M_L^T\right)^{-1} \, M^T, \tag{3.52}$$

where A has the following general form:

$$\begin{pmatrix} \frac{1}{2} & a & b \\ -a & \frac{1}{2} & c \\ -b & -c & \frac{1}{2} \end{pmatrix}, \tag{3.53}$$

with a, b, c real numbers. In this case M_L and $M \equiv M_R$ are general real matrices. One can always go to a basis where one of them is diagonal, for example M_L, reducing the total number

of model parameters to 21. In order to further reduce the number of degrees of freedom, we make a similar "minimal flavor violation hypothesis" to this scheme too, namely, we choose the M matrix also to be diagonal, reducing from 21 to 15 parameters. The most general Dirac mass matrix is parametrized as in Eq. (3.52). Hence we have a model with 15 parameters that may be taken as three parameters from the A matrix, three from the M_L matrix, and three from the matrix M, in addition to the three light neutrino masses and three mixing angles. As for the inverse type-I see-saw case, we do the scan over the light neutrino mass and oscillation parameters and the 9 additional free parameters. The main difference in this case with respect to the inverse, is in the structure of the A matrix in Eq. (3.53). We scan over the A matrix parameters in the form:

$$A_{ij}\ \epsilon\,(0 - 10^{-2})\ . \tag{3.54}$$

Now we define M_{Lii} in analogy to M_{ii} in Eq. (3.51) and we vary v_L in the range $(0.01-10)$ eV.

3.7 Numerical results

Low-scale see-saw schemes lead to sizeable rates for lepton flavor violating processes as well as to non-standard effects in neutrino propagation associated to non-unitary lepton mixing matrix. In this section we will quantify the interplay between these, more precisely, between the branching ratio of Eq. (3.48) in the low-scale type-I see-saw schemes considered here and the magnitude of the unitarity deviation defined in Eq. (3.45), taking into account Eqs. (3.50) and (3.52) and the requirement of acceptable light neutrino masses. For definiteness we assume leptonic CP conservation so that all lepton Yukawa couplings and mass entries are real.

We have computed the branching ratio (Br) for the charged lepton flavor violating radiative processes using Eq. (3.48), accurate to order $O(\epsilon^3)$ in the neutrino diagonalizing matrix, and we have displayed the degree of correlation of these observables with the corresponding unitarity violating parameters $|\eta_{ij}|$. In Fig. 3.3 we show the results for the inverse type-I see-saw scheme for NH and IH for the process $\mu \to e\gamma$, respectively. As explained in the previous section, points result from a scan over the light neutrino mass and mixing parameters at 3σ, together with the scan over the 9 free model parameters defined above.

In Fig. 3.4 we show the corresponding results for the $\tau \to e\gamma$ branching ratio in the inverse

type-I see-saw scheme for NH and IH, respectively. In Fig. 3.5 we show the corresponding results for the process $\tau \to \mu\gamma$ within the inverse type-I see-saw, for NH and IH neutrino spectra, respectively.

Now we turn to the linear type-I see-saw scheme. In Fig. 3.6 we show our results for the branching ratio for the process $\mu \to e\gamma$ in the linear see-saw for NH and IH, respectively. The points are obtained through a scan over the neutrino oscillation parameters, as well as the free model parameters, as already described.

In Fig. 3.7 we show our results for the $\tau \to e\gamma$ branching ratio, for the NH and IH case, respectively. Finally, in Fig. 3.8 we present the corresponding results for the $\tau \to \mu\gamma$ process.

These results are summarized in table 3.2. One sees that the magnitude of the non-unitarity effects in the lepton mixing matrix can reach up to the percent level without any conflict with the constraints that follow from lepton flavor violation searches in the laboratory. Given the large - TeV scale - assumed masses of the singlet "right-handed" neutrinos, there are no direct search constraints [108, 135, 136] on heavy active mixing that can be translated as a constraints in η matrix through the row unitarity of the K matrix. The main factor limiting the magnitude of non-unitarity effects then comes from the weak universality constraints. As expected, there is stronger degree of correlation between $\mu \to e\gamma$ and η_{12} than other η's, or between $\tau \to e\gamma$ and η_{13} than others, etc. As a result, in these cases one obtains the strongest restriction on unitarity violation.

Before closing let us comment on the robustness of our results with respect to the assumptions made in Sec. 3.6. As far as the regions obtained in Figs. (3.3)-(3.8) are concerned, we can state that they remain "allowed" once one departs from our simplifying assumptions. As expected, we have verified that the regions obtained away from the simplifying assumptions may allow for somewhat larger values of the LFV parameters η affecting neutrino propagation. However, on account of weak universality constraints, we prefer to stick to the more conservative values we have presented in Table 3.2.

Process	$\mu \to e\gamma$		$\tau \to e\gamma$		$\tau \to \mu\gamma$	
Hierarchy	NH	IH	NH	IH	NH	IH
$\lvert\eta^I_{12}\rvert <$	1.44×10^{-3}	1.20×10^{-3}	2.20×10^{-2}	2.37×10^{-2}	2.20×10^{-2}	2.37×10^{-2}
$\lvert\eta^I_{13}\rvert <$	1.13×10^{-2}	1.23×10^{-2}	1.02×10^{-2}	1.02×10^{-2}	2.18×10^{-2}	2.19×10^{-2}
$\lvert\eta^I_{23}\rvert <$	2.02×10^{-2}	1.49×10^{-2}	4.83×10^{-2}	3.71×10^{-2}	1.17×10^{-2}	1.18×10^{-2}
$\lvert\eta^L_{12}\rvert <$	9.52×10^{-4}	7.27×10^{-4}	4.28×10^{-2}	4.20×10^{-2}	3.86×10^{-2}	3.88×10^{-2}
$\lvert\eta^L_{13}\rvert <$	3.17×10^{-2}	2.84×10^{-2}	1.05×10^{-2}	1.07×10^{-2}	4.74×10^{-2}	4.28×10^{-2}
$\lvert\eta^L_{23}\rvert <$	2.10×10^{-2}	2.79×10^{-2}	3.90×10^{-2}	4.00×10^{-2}	1.14×10^{-2}	1.11×10^{-2}

Table 3.2: Limits on unitarity violation parameters from lepton flavor violation searches. The numbers given in parenthesis correspond to the improvement obtained with the recent MEG limit on $\mu \to e\gamma$. Other entries in the table are unchanged. These limits express the correlation between lepton non-unitarity and LFV that holds in low-scale see-saw schemes under a "minimal flavor violation hypothesis" defined in the text.

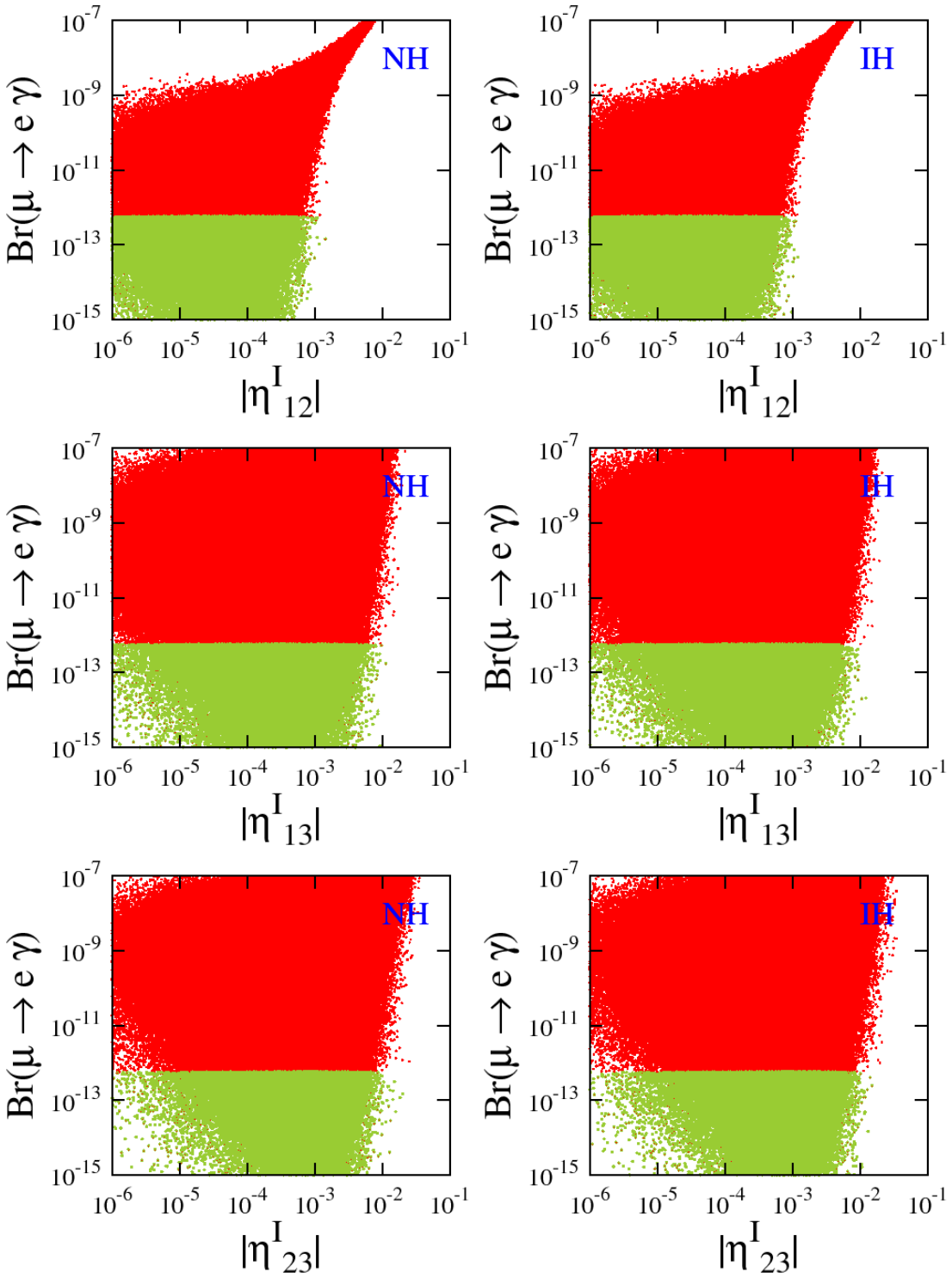

Figure 3.3: Branching ratios for the process $\mu \to e\gamma$ in type-I inverse see-saw scheme with NH and IH. We scan over the light neutrino mass and mixing parameters at 3 σ, and over the model parameters, fixing v_M at 1 TeV and varying the v_μ scale from 1×10^{-10} GeV to 1×10^{-8} GeV. The red (dark) points are excluded by the current limit from MEGA collaboration [116] while the green (light) points are compatible with MEGA limit.

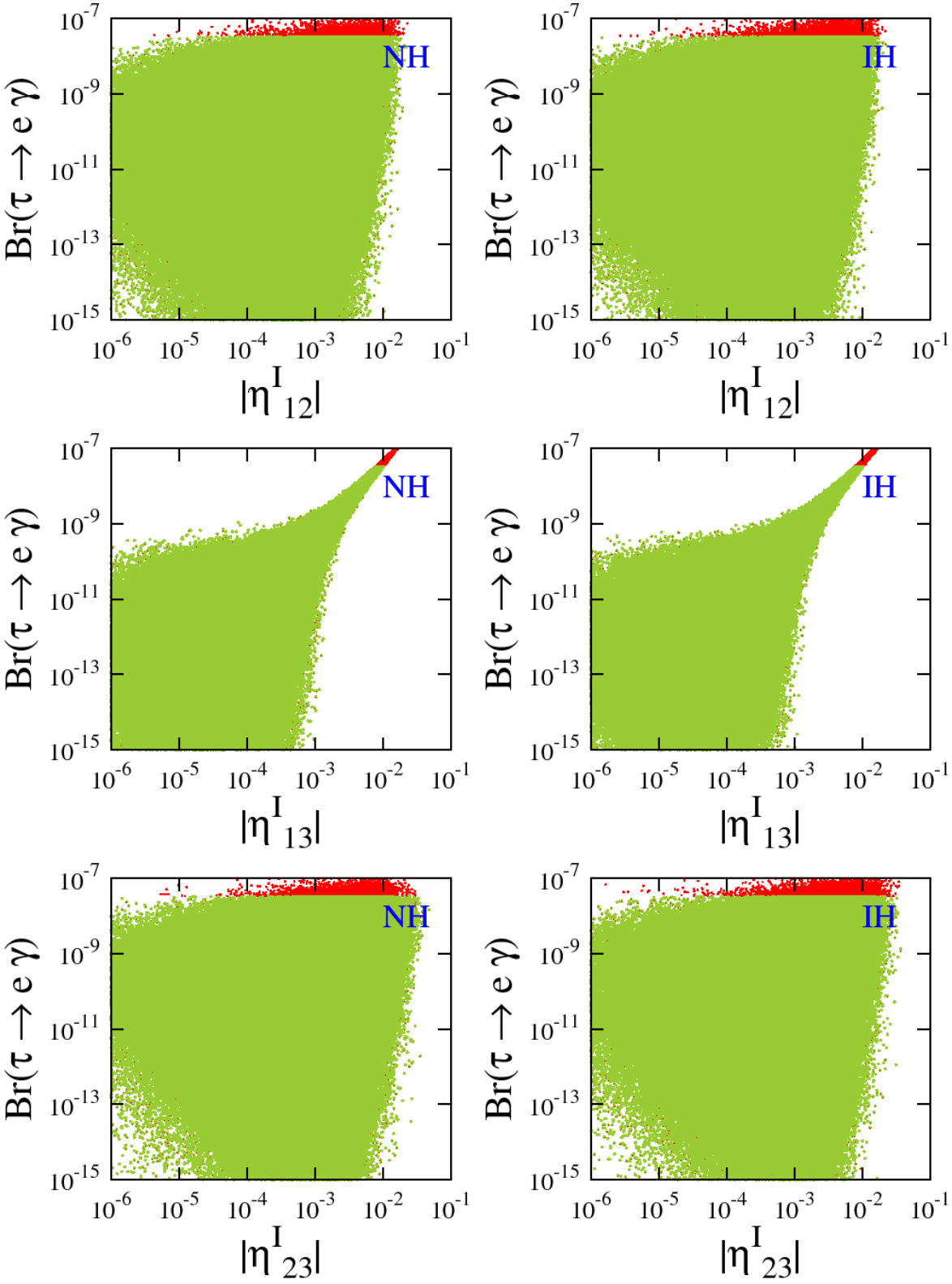

Figure 3.4: $\tau \to e\gamma$ branching ratio in the inverse type-I see-saw with NH and IH. The scan is performed as in Fig. 3.3 and the indicated limit is from the PDG [5].

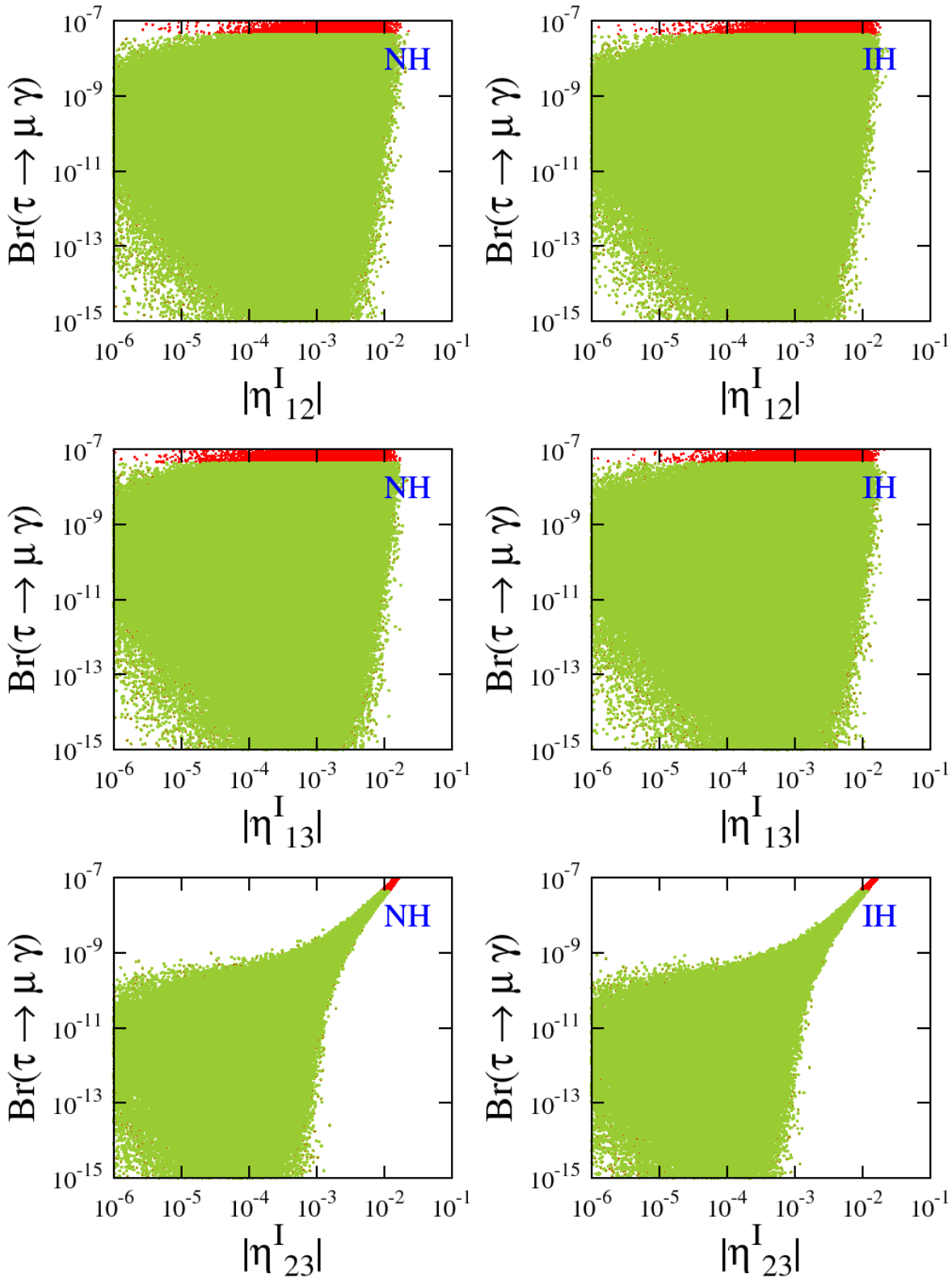

Figure 3.5: $\tau \to \mu\gamma$ branching ratio in the inverse type-I see-saw with NH and IH. The scan is performed as in Fig. 3.3 and the indicated limit is from the PDG [5].

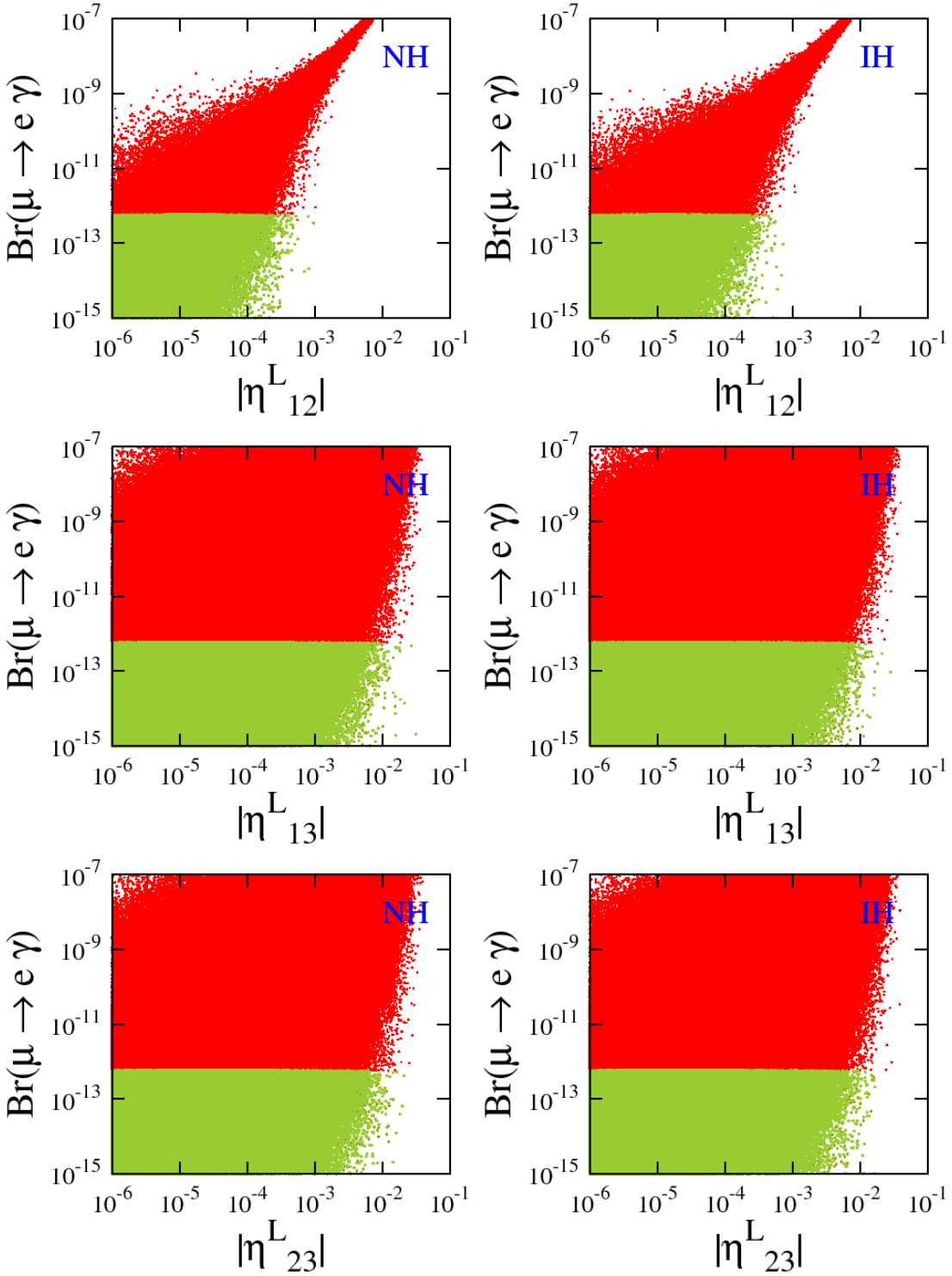

Figure 3.6: Branching for the process $\mu \to e\gamma$ in type-I linear see-saw with NH and IH. We scan over the parameters as in Fig. 3.3. The red (dark) points are excluded by the current limit from MEGA collaboration [116] while the green (light) points are compatible with MEGA limit.

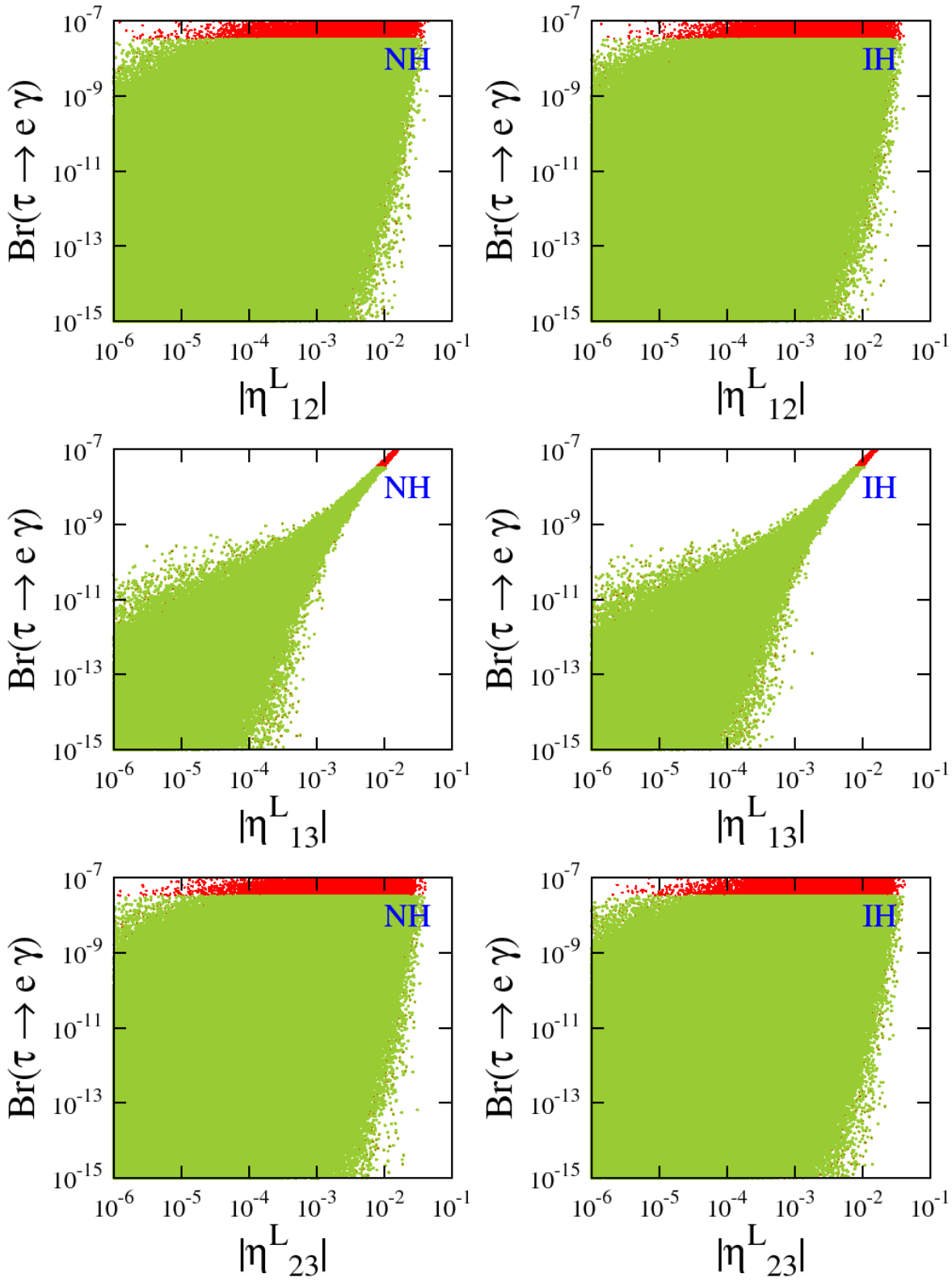

Figure 3.7: $\tau \to e\gamma$ branching ratio, in Linear type-I see-saw for NH and IH. Parameters scanned as in Fig. 3.3 and the indicated limit is from the PDG [5].

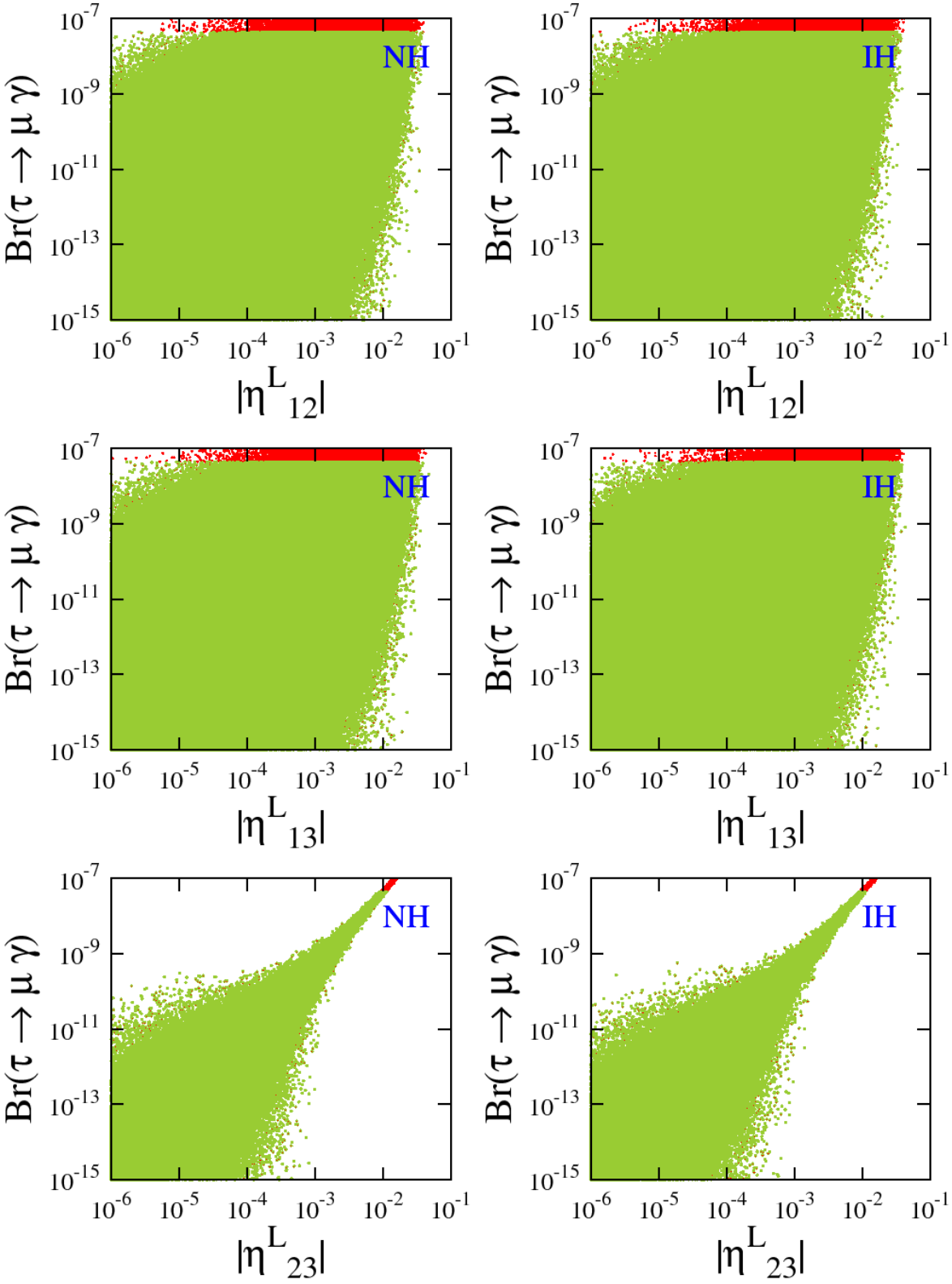

Figure 3.8: $\tau \to \mu\gamma$ branching ratio, in Linear type-I see-saw for NH and IH. Parameters scanned as in Fig. 3.3 and the indicated limit is from the PDG [5].

CHAPTER 4

Non–Standard Interactions at Daya Bay

Neutrino oscillation data imply the presence of at least two massive neutrinos to explain the current values for the atmospheric and solar mass splittings [1]. From the theoretical point of view, one appealing mechanism to explain the smallness of neutrino masses is the type-I see-saw. Other realizations of the dimension five operator can produce values for the neutrino masses consistent with the neutrino phenomenology, namely low scale realizations [79, 106]. New neutrino interactions (NSI) are expected in such SM extensions. The exchange of new heavy particles could leave a low energy 'fingerprint' in the form of NSI.

These new interactions have been studied in the literature in connection with solar and atmospheric neutrino oscillation. In fact, before the confirmation for the LMA solution for the solar neutrino problem by SNO and Kamland, NC NSI were suggested as a possible explanation of the deficit of electron neutrinos coming from the Sun due to an MSW–like effect with massless neutrinos [88, 137, 138].

In order to study the phenomenological impact of NSI on the neutrino oscillation phenomenology, we consider an effective formalism approach to parametrize the new neutrino interactions.

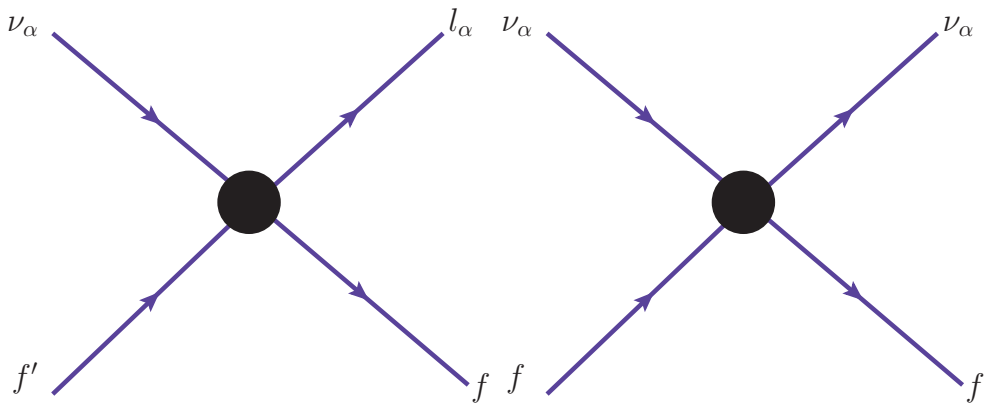

Figure 4.1: Effective four fermion interactions in the SM. Left diagram for the CC neutrino interaction with fermions f. Right diagram for the NC interaction with fermions f. Notice that the flavor is the same for both interactions.

NSI parametrization

Four–fermion neutrino interactions in the SM are given by the following Lagrangians:

$$\begin{aligned}\mathcal{L}_{CC} &= \frac{G_F}{\sqrt{2}}\left[\bar{\nu}_\alpha\gamma^\rho(1-\gamma^5)\ell_\alpha\right]\left[\bar{f}'\gamma_\rho(1-\gamma^5)f\right]\\ \mathcal{L}_{\rm NC} &= \frac{G_F}{\sqrt{2}}\left[\bar{\nu}_\alpha\gamma^\rho(1-\gamma^5)\nu_\alpha\right]\left[\bar{f}\gamma_\rho(1-\gamma^5)f\right],\end{aligned} \tag{4.1}$$

where the first line accounts for the Charged Current (CC) interaction, while the second one refers to the Neutral Current (NC) interaction. As we can see from Fig. 4.1, the NC interaction is flavor diagonal and involves two neutrino fields.

We can generalize the SM Lagrangian in Eq. (4.1) by including new couplings that allow for a large number of interactions, for instance flavor changing interactions in the NC part. The following Lagrangian is a generalization of the SM effective Lagrangian where the strength of the new physics is given by the Fermi constant G_F times the new dimensionaless couplings ε [139]:

$$\begin{aligned}\mathcal{L}^{NSI}_{V\pm A} = &\frac{G_F}{\sqrt{2}}\sum_{f,f'}\tilde{\varepsilon}^{S(D),f,f',V\pm A}_{\alpha\beta}\left[\bar{\nu}_\beta\gamma^\rho(1-\gamma^5)\ell_\alpha\right]\left[\bar{f}'\gamma_\rho(1\pm\gamma^5)f\right]\\ &+\frac{G_F}{\sqrt{2}}\sum_{f}\tilde{\varepsilon}^{m,f,V\pm A}_{\alpha\beta}\left[\bar{\nu}_\alpha\gamma^\rho(1-\gamma^5)\nu_\beta\right]\left[\bar{f}\gamma_\rho(1\pm\gamma^5)f\right]+\text{h.c.},\end{aligned} \tag{4.2}$$

Notice that in Eq. (4.2) we keep the vector and axial Lorentz structure of the SM. In the NSI Lagrangian in Eq. (4.2) we have parametrized the CC part, in the first line, with the

superscripts 'S' and 'D' corresponding to source and detection, respectively, indicating the NSI origin. In the second line, corresponding to the NC part, we have used the superscript 'm' that refers to neutrino propagation in matter.

The Lagrangian in Eq. (4.2) has been the starting point for many phenomenological studies. In particular, several constraints for the NC NSI-like have been studied in Refs. [140–145].

4.1 NSI at reactor experiments

NSI effects may appear at three different stages in a given neutrino experiment, namely neutrino production, neutrino detection and neutrino propagation from the source to the detector. In a short–baseline reactor experiment, such as Daya Bay, the NSI effects on the neutrino propagation in matter will be negligible since it happens mainly in vacuum. Therefore, we focus on the NSI effect in the production and detection of reactor antineutrinos.

The NSI couplings relevant for short-baseline reactor neutrino experiments are $\varepsilon^{ud}_{e\alpha}$, since they may have an effect over the production and detection processes of reactor neutrinos, occurring through beta and inverse-beta decays. Therefore, neglecting the effect in neutrino propagation, the general Lagrangian in Eq. (4.2) for NSI at $1\,\text{km}$ baseline reactors is given by:

$$\mathcal{L}_{V\pm A} = \frac{G_F}{\sqrt{2}} \sum_{f,f'} \tilde{\varepsilon}^{S(D),f,f',V\pm A}_{\alpha\beta} \left[\bar{\nu}_\beta \gamma^\rho (1-\gamma^5) \ell_\alpha\right] \left[\bar{f}' \gamma_\rho (1 \pm \gamma^5) f\right] \,. \tag{4.3}$$

In order to simplify the notation, will be use the definition $\varepsilon^{S(D)}_{e\beta} \equiv \tilde{\varepsilon}^{S(D),u,d,V\pm A}_{e\beta}$ all along this chapter.

Definition of the neutrino states

Due to NSI at the neutrino source, in the production of a neutrino state $|\nu_\alpha\rangle$ in a CC weak process, a 'new' state $|\nu_\gamma\rangle$ can appear together with the SM lepton l_α. In this example, one can consider the flavor state $|\nu_\alpha\rangle$ has an 'extra' flavor component that we will incorporate into

the neutrino flavor states, as follows [1]:

$$\begin{aligned} |\nu_\alpha^s\rangle &= |\nu_\alpha\rangle + \sum_\gamma \varepsilon_{\alpha\gamma}^s |\nu_\gamma\rangle \\ \langle\nu_\beta^d| &= \langle\nu_\beta| + \sum_\eta \varepsilon_{\eta\beta}^d \langle\nu_\eta| \,. \end{aligned} \tag{4.4}$$

Thus, there is a probability to detect a flavor conversion at zero distance, as we will discuss later on, which comes from the fact that the new flavor basis, defined by Eq. (4.4) is no longer complete [88]. For the SM flavor states we still have the usual relation for the neutrino mixing in terms of mass eigenstates:

$$|\nu_\alpha\rangle = \sum_k U_{\alpha k}^* |\nu_k\rangle \,. \tag{4.5}$$

Analogous relations for antineutrinos can be established from the transposed conjugation of Eq. (4.4):

$$\begin{aligned} |\bar{\nu}_\alpha^s\rangle &= |\bar{\nu}_\alpha\rangle + \sum_\gamma \varepsilon_{\alpha\gamma}^{s*} |\bar{\nu}_\gamma\rangle \;, \\ \langle\bar{\nu}_\beta^d| &= \langle\bar{\nu}_\beta| + \sum_\eta \varepsilon_{\eta\beta}^{d*} \langle\bar{\nu}_\eta| \;. \end{aligned} \tag{4.6}$$

Here again, the usual relation for the SM flavor states in terms of mass eigenstates is the adjoint version of Eq. (4.5) :

$$|\bar{\nu}_\alpha\rangle = \sum_k U_{\alpha k} |\bar{\nu}_k\rangle \,. \tag{4.7}$$

Effective anti-neutrino survival probability

The anti-neutrino transition probability from flavor α to β after traveling a distance L from the source to the detector is defined as:

$$P_{\bar{\nu}_\alpha^s \to \bar{\nu}_\beta^d} = |\langle\bar{\nu}_\beta^d| \exp\left(-i\, H\, L\right) |\bar{\nu}_\alpha^s\rangle|^2. \tag{4.8}$$

After computing the amplitude and writing the transition probability in the usual real and imaginary parts of the mixing matrix products, one gets:

$$\begin{aligned} P_{\bar{\nu}_\alpha^s \to \bar{\nu}_\beta^d} = \sum_{j,k} Y_{\alpha\beta}^j Y_{\alpha\beta}^{k*} - 4 \sum_{j>k} \mathcal{R}\{Y_{\alpha\beta}^j Y_{\alpha\beta}^{k*}\} \, \sin^2\left(\frac{\Delta m_{jk}^2 \, L}{4E}\right) \\ + 2 \sum_{j>k} \mathcal{I}\{Y_{\alpha\beta}^j Y_{\alpha\beta}^{k*}\} \, \sin\left(\frac{\Delta m_{jk}^2 \, L}{2E}\right) \end{aligned} \tag{4.9}$$

[1] Notice that this is an effective definition of the neutrino flavor states in presence of NSI since they are not normalized states. For more details check the appendix B.3

where $Y^j_{\alpha\beta}$ is defined as:

$$Y^j_{\alpha\beta} \equiv U^*_{\beta j}U_{\alpha j} + \sum_\gamma \varepsilon^{s*}_{\alpha\gamma}U^*_{\beta j}U_{\gamma j} + \sum_\eta \varepsilon^{d*}_{\eta\beta}U^*_{\eta j}U_{\alpha j} + \sum_{\gamma,\eta}\varepsilon^{s*}_{\alpha\gamma}\varepsilon^{d*}_{\eta\beta}U^*_{\eta j}U_{\gamma j}\ . \tag{4.10}$$

To get the antineutrino survival probability one needs to expand the general transition probability and replace α and β by e. This probability may be decomposed in the following terms:

$$\begin{aligned} P_{\bar\nu_e^s\to\bar\nu_e^d} &= P^{SM}_{\bar\nu_e\to\bar\nu_e} + P^{\text{NSI}}_{\text{non-osc}} + P^{\text{NSI}}_{\text{osc-atm}} + P^{\text{NSI}}_{\text{osc-solar}} \\ &+ \mathcal{O}\left[\varepsilon^3, s^3_{13}, \varepsilon^2 s_{13}, \varepsilon s_{13}\left(\frac{\Delta m^2_{21}L}{2E}\right), \varepsilon\left(\frac{\Delta m^2_{21}L}{2E}\right)^2, s^2_{13}\left(\frac{\Delta m^2_{21}L}{2E}\right)\right] \end{aligned} \tag{4.11}$$

where the SM survival probability is given by:

$$P^{SM}_{\bar\nu_e\to\bar\nu_e} = 1 - \sin^2(2\theta_{13})\left(c^2_{12}\sin^2\Delta_{31} + s^2_{12}\sin^2\Delta_{32}\right) - c^4_{13}\sin^2(2\theta_{12})\sin^2\Delta_{21}\ , \tag{4.12}$$

with $s_{ij} = \sin\theta_{ij}$, $c_{ij} = \cos\theta_{ij}$ and $\Delta_{ij} = \Delta m^2_{ij}L/4E$. The NSI part of the survival probability is given by [2]:

$$\begin{aligned} P^{\text{NSI}}_{\text{non-osc}} &= 2\left(|\epsilon^d_{ee}|\cos\phi^d_{ee} + |\varepsilon^s_{ee}|\cos\phi^s_{ee}\right) + |\varepsilon^d_{ee}|^2 + |\varepsilon^s_{ee}|^2 + 2|\varepsilon^d_{ee}||\varepsilon^s_{ee}|\cos(\phi^d_{ee} - \phi^s_{ee}) \\ &+ 2|\varepsilon^d_{ee}||\varepsilon^s_{ee}|\cos(\phi^d_{ee} + \phi^s_{ee}) + 2|\varepsilon^s_{e\mu}||\varepsilon^d_{\mu e}|\cos(\phi^s_{e\mu} + \phi^d_{\mu e}) + 2|\varepsilon^s_{e\tau}||\varepsilon^d_{\tau e}|\cos(\phi^s_{e\tau} + \phi^d_{\tau e})\ , \end{aligned} \tag{4.13}$$

$$\begin{aligned} P^{\text{NSI}}_{\text{osc-atm}} &= 2\left\{s_{13}s_{23}\left[|\varepsilon^s_{e\mu}|\sin(\delta - \phi^s_{e\mu}) - |\varepsilon^d_{\mu e}|\sin(\delta + \phi^d_{\mu e})\right]\right. \\ &+ s_{13}c_{23}\left[|\varepsilon^s_{e\tau}|\sin(\delta - \phi^s_{e\tau}) - |\varepsilon^d_{\tau e}|\sin(\delta + \phi^d_{\tau e})\right] \\ &- s_{23}c_{23}\left[|\varepsilon^s_{e\mu}||\varepsilon^d_{\tau e}|\sin(\phi^s_{e\mu} + \phi^d_{\tau e}) + |\varepsilon^s_{e\tau}||\varepsilon^d_{\mu e}|\sin(\phi^s_{e\tau} + \phi^d_{\mu e})\right] \\ &- \left. c^2_{23}|\varepsilon^s_{e\tau}||\varepsilon^d_{\tau e}|\sin(\phi^s_{e\tau} + \phi^d_{\tau e}) - s^2_{23}|\varepsilon^s_{e\mu}||\varepsilon^d_{\mu e}|\sin(\phi^s_{e\mu} + \phi^d_{\mu e})\right\}\sin(2\Delta_{31}) \\ &- 4\left\{s_{13}s_{23}\left[|\varepsilon^s_{e\mu}|\cos(\delta - \phi^s_{e\mu}) + |\varepsilon^d_{\mu e}|\cos(\delta + \phi^d_{\mu e})\right]\right. \\ &+ s_{13}c_{23}\left[|\varepsilon^s_{e\tau}|\cos(\delta - \phi^s_{e\tau}) + |\varepsilon^d_{\tau e}|\cos(\delta + \phi^d_{\tau e})\right] \\ &+ s_{23}c_{23}\left[|\varepsilon^s_{e\mu}||\varepsilon^d_{\tau e}|\cos(\phi^s_{e\mu} + \phi^d_{\tau e}) + |\varepsilon^s_{e\tau}||\varepsilon^d_{\mu e}|\cos(\phi^s_{e\tau} + \phi^d_{\mu e})\right] \\ &+ \left. c^2_{23}|\varepsilon^s_{e\tau}||\varepsilon^d_{\tau e}|\cos(\phi^s_{e\tau} + \phi^d_{\tau e}) + s^2_{23}|\varepsilon^s_{e\mu}||\varepsilon^d_{\mu e}|\cos(\phi^s_{e\mu} + \phi^d_{\mu e})\right\}\sin^2(\Delta_{31}) \end{aligned} \tag{4.14}$$

$$\begin{aligned} P^{\text{NSI}}_{\text{osc-solar}} &= 2\sin 2\theta_{12}\Delta_{21}\left\{-c_{23}(|\varepsilon^s_{e\mu}|\sin\phi^s_{e\mu} + |\varepsilon^d_{\mu e}|\sin\phi^d_{\mu e})\right. \\ &+ \left. s_{23}(|\varepsilon^s_{e\tau}|\sin\phi^s_{e\tau} + |\varepsilon^d_{\tau e}|\sin\phi^d_{\tau e})\right\}\ . \end{aligned} \tag{4.15}$$

[2] Linear coefficients at order ε in Eqs. (4.13, 4.14, 4.15) are the same as in reference [139] and there is a nice agreement between both probabilities.

We have split the NSI terms, as given in Eq. (4.11), in 'oscillating' $P^{\text{NSI}}_{\text{osc}}$ and 'non-oscillating' $P^{\text{NSI}}_{\text{non-osc}}$ terms where the former terms depends on the oscillating phase Δ_{ij} while the latter are not. In the limit $L \to 0$, the 'non-oscillating' term is the only NSI term that contributes to the total probability in Eq. (4.11). It is worth noticing that since the 'non-oscillating' term in Eq. (4.13) might produce positive non-zero values for a given combination of the NSI parameters, the total probability in Eq. (4.11) can be bigger than one. When the states are properly normalized, the probability is less or equal to one. However, the normalization of the states cancels out in the calculation of the number of events and therefore we do not consider it here.

4.2 Specific settings

The coefficients representing the NSI couplings in Eq. (4.11) for detection (d) and production (s) are general Hermitian matrices ε, that can be independent. Antineutrinos in reactors are produced by beta decay processes and detected via the inverse process. In this case one would expect the two matrices will satisfy $\varepsilon^{s}_{e\alpha} = \varepsilon^{d*}_{\alpha e}$. We define this as *case I*. Other possibilities can also be phenomenologically rich although less motivated physically unless we want to study some departures from the CPT theorem [146]. For instance we can have an asymmetry between the detection and production processes, for example with only NSI at source or we can have the same NSI strength at the source and detector with different phases. The probability expressions for both cases were developed and we show them for completeness in appendices B.1 and B.2, respectively.

Case I: $\varepsilon^{s}_{e\alpha} = \varepsilon^{d*}_{\alpha e}$

In this case we parametrize the NSI couplings in polar form, magnitude and phase, related by the expressions:

$$\varepsilon^{s}_{e\alpha} = |\varepsilon_\alpha| \mathrm{e}^{\mathrm{i}\phi_\alpha} \quad \text{and} \quad \varepsilon^{d}_{\alpha e} = |\varepsilon_\alpha| \mathrm{e}^{-\mathrm{i}\phi_\alpha} \ . \tag{4.16}$$

With these assumptions, Eq. (4.11) takes a simple form:

$$\begin{aligned} P_{\bar{\nu}_e^s \to \bar{\nu}_e^d} \simeq & \underbrace{1 - \sin^2 2\theta_{13} \left(c_{12}^2 \sin^2 \Delta_{31} + s_{12}^2 \sin^2 \Delta_{32}\right) - c_{13}^4 \sin^2 2\theta_{12} \sin^2 \Delta_{21}}_{\text{Standard Model terms}} \\ & + \underbrace{4|\varepsilon_e|\cos\phi_e + 4|\varepsilon_e|^2 + 2|\varepsilon_e|^2 \cos 2\phi_e + 2|\varepsilon_\mu|^2 + 2|\varepsilon_\tau|^2}_{\text{non-oscillatory NSI terms}} \\ & - \underbrace{4\{s_{23}^2|\varepsilon_\mu|^2 + c_{23}^2|\varepsilon_\tau|^2 + 2s_{23}c_{23}|\varepsilon_\mu||\varepsilon_\tau|\cos(\phi_\mu - \phi_\tau)\} \sin^2 \Delta_{31}}_{\text{oscillatory NSI terms}} \\ & - \underbrace{4\{2s_{13}[s_{23}|\varepsilon_\mu| \cos(\delta - \phi_\mu) + c_{23}|\varepsilon_\tau| \cos(\delta - \phi_\tau)]\} \sin^2 \Delta_{31}}_{\text{oscillatory NSI terms}}. \end{aligned} \tag{4.17}$$

We fix the atmospheric mass splitting Δm^2_{31} as an external measurement and neglecting the solar contribution: $\Delta m^2_{21} \to 0$, the NSI effect in Eq. (4.17) can be interpreted as a shift in the total event normalization and in the reactor mixing angle [146] given by:

$$\begin{aligned} 1 &\to 1 + 4|\varepsilon_e| \cos\phi_e + 4|\varepsilon_e|^2 + 2|\varepsilon_e|^2 \cos 2\phi_e + 2|\varepsilon_\mu|^2 + 2|\varepsilon_\tau|^2 \\ s_{13}^2 &\to s_{13}^2 + s_{23}^2|\varepsilon_\mu|^2 + c_{23}^2|\varepsilon_\tau|^2 + 2s_{23}c_{23}|\varepsilon_\mu||\varepsilon_\tau| \cos(\phi_\mu - \phi_\tau) \\ &\quad + 2s_{13}\left[s_{23}|\varepsilon_\mu| \cos(\delta - \phi_\mu) + c_{23}|\varepsilon_\tau| \cos(\delta - \phi_\tau)\right] \ . \end{aligned} \tag{4.18}$$

In addition to the usual oscillation parameters here we have six new degrees of freedom, one magnitude and one phase for each neutrino family. In order to systematically extract some information on the NSI parameters, in our analysis we will consider three main cases: i) NSI only with ν_e, ii) NSI only with ν_μ or ν_τ (equivalent for maximal atmospheric mixing) and iii) NSI with all neutrino flavors, with flavor-independent couplings, i.e. $\varepsilon_e = \varepsilon_\mu = \varepsilon_\tau$ (flavor universal case). Therefore, in each case we will have two NSI parameters, one absolute value plus one phase, together with the SM oscillation ones, which are mainly the atmospheric mass splitting, the reactor mixing angle and the Dirac CP phase.

Before statistical analysis of the Daya Bay data, we will study the impact of the NSI at the probability level in the next section. This will be very useful in order to discover some correlations between parameters. In all the plots in this section, wherever the values for the standard oscillation parameters were fixed, we use $\sin^2\theta_{13} = 0.023$ (Daya Bay best fit value), maximal mixing for the atmospheric angle $\theta_{23} = \pi/4$ and the best fit values from Ref. [1] for the solar oscillation parameters.

4.3 NSI effect on the oscillation probability

As mentioned before, we will study the effect separating the parameter region in three parts:

- Only the electron flavor contributes: $\varepsilon_e \neq 0$ and $\varepsilon_{\mu,\tau} = 0$. In this case, Eq. (4.17) takes the form:

$$P^{\text{NSI-e}}_{\bar{\nu}_e^s \to \bar{\nu}_e^d} \simeq P^{SM}_{\bar{\nu}_e \to \bar{\nu}_e} + 4|\varepsilon_e|\text{cos}\phi_e + 4|\varepsilon_e|^2 + 2|\varepsilon_e|^2 \cos 2\phi_e \ , \tag{4.19}$$

  where we see that only the NSI 'non-oscillating' term contributes to the probability.

- Only the muon(or tau) flavor contributes: $\varepsilon_{\mu,\tau} \neq 0$ and $\varepsilon_e = 0$. In this case, Eq. (4.17) is reduced to:

$$P^{\text{NSI-}\mu}_{\bar{\nu}_e^s \to \bar{\nu}_e^d} \simeq P^{SM}_{\bar{\nu}_e \to \bar{\nu}_e} + 2|\varepsilon_\mu|^2 - 4\{s_{23}^2|\varepsilon_\mu|^2 + 2s_{13}s_{23}|\varepsilon_\mu|\cos(\delta - \phi_\mu)\}\sin^2\Delta_{31} \, . \tag{4.20}$$

  Here unlike in the electron case the NSI contribute with an extra oscillating term.

- Flavor Universal (FU) couplings: $\varepsilon_e = \varepsilon_{\mu,\tau} \equiv \varepsilon$. In this case, Eq. (4.17) is given by:

$$\begin{aligned} P^{\text{NSI-}\alpha}_{\bar{\nu}_e^s \to \bar{\nu}_e^d} \simeq\ & P^{SM}_{\bar{\nu}_e \to \bar{\nu}_e} + 4|\varepsilon|\text{cos}\phi + 2|\varepsilon|^2\,(4 + \cos 2\phi) \\ & - 4\{|\varepsilon|^2 + 2s_{23}c_{23}|\varepsilon|^2 + 2s_{13}|\varepsilon|\cos(\delta - \phi)(s_{23} + c_{23})\}\sin^2\Delta_{31} \, . \end{aligned} \tag{4.21}$$

  This case is phenomenologically interesting because the NSI contributes with an oscillatory term and also with a 'non-oscillatory' term, which comes from the electron NSI coupling contribution.

4.3.1 Effective probability in presence of NSI

In the left (right) panel of Fig. 4.2 we have plotted the probability in Eq. (4.19) (Eq. (4.20)), which corresponds to the electron (muon/tau) case. In both cases we see that the NSI contribution produces a shift in the minimum of the SM probability case (full line). This shift can be constrained if the reactor angle is well measured. On the other hand, the NSI does not produce any horizontal shift, showing that the new interactions do not induce a change in the energy of the survival probability. Therefore, a rate analysis might be enough to constrain the presence of NSI at reactors.

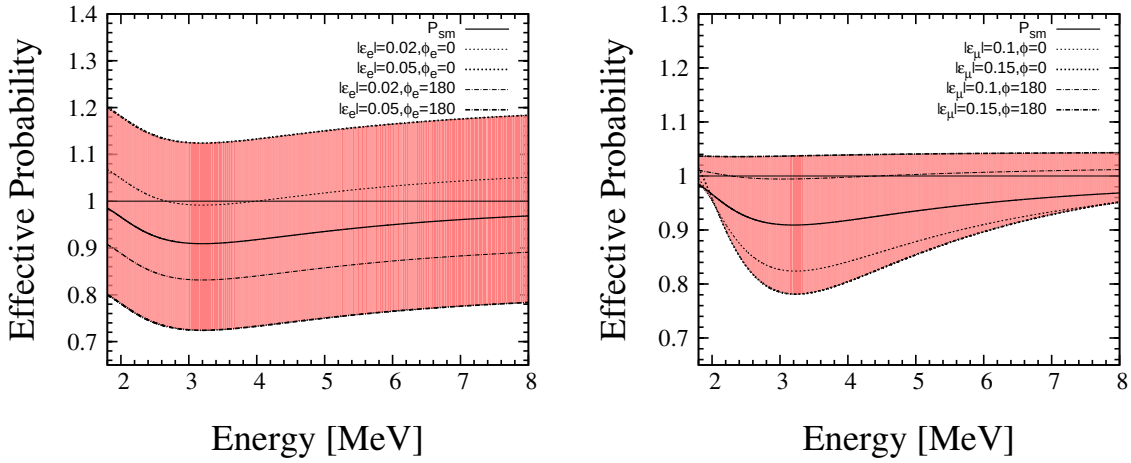

Figure 4.2: Effective $\bar{\nu}_e \to \bar{\nu}_e$ survival probability as a function of neutrino energy in the presence of NSI. Left panel shows the impact of $|\varepsilon_e|$ and ϕ_e. Right panel shows the same for $|\varepsilon_\mu|$, ϕ_μ and $\delta = 0$. In both the panels, the solid black lines correspond to the probability without new physics involved (SM case).

The effect of the 'non-oscillatory' NSI term is also visible in both panels of Fig. 4.2. Notice that, for some values of the NSI couplings, the effective probability is bigger than one, as it was commented before. The effect is more prominent for the electron case in the left panel than for the muon in the right panel. The origin of this difference is that 'non-oscillatory' contribution for the electron case is of first order in ε while for the muon/tau the NSI effect comes at second order in the NSI coupling, as it can be seen in Eqs. 4.19 and 4.20, respectively. Finally, it is clear from both panels of Fig. 4.2 that there is an important effect of the new phases affecting the size of the shift in the reactor angle θ_{13}.

The plot in Fig. 4.3 exhibits some features already commented before for the electron and muon/tau case. This case correspond to the FU case where all the NSI couplings contribute with the same strength to the probability in Eq. (4.21). The difference with the other cases is the functional dependence with the Dirac and the new NSI phase. The new phase ϕ is present in both terms, oscillatory and 'non-oscillatory' while the Dirac phase is only present in the oscillatory term. For the electron case the Dirac phase is not present while for the muon/tau case it is possible to redefine the phases as $\phi' \equiv \delta - \phi$. In the FU case in Eq. (4.21) however, both phases contribute independently. Therefore, the FU case has more free parameters than

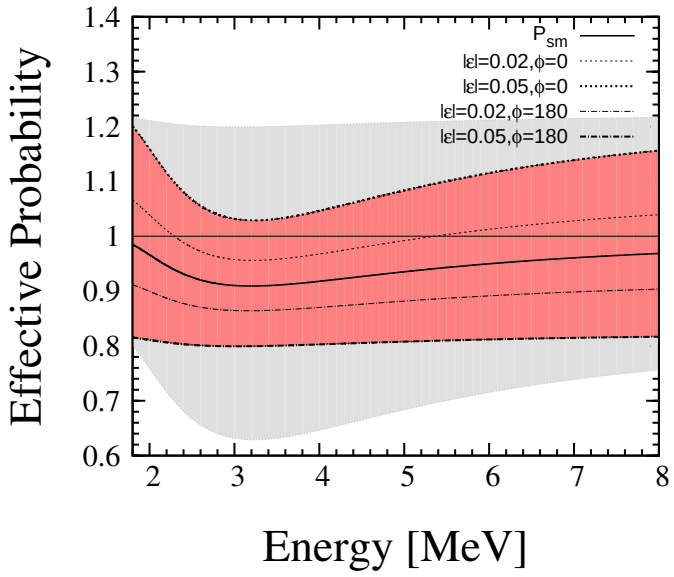

Figure 4.3: Effective neutrino survival probability as a function of neutrino energy for the flavor universal case. The region in red shows the combined effect of the new physics parameters $|\varepsilon|$ and ϕ, while the extended probability band after the variation of the δ phase as is shown in gray.

the other two cases. The effect of a variation in the Dirac phase in the range $[-\pi, \pi]$ is shown as the gray band in Fig. 4.3.

4.3.2 Correlations between NSI parameters and θ_{13}

Based on the probability plots showed in the last section, now we fix the energy to an average value, which is close to a total rate analysis, in order to further explore the correlations between parameters due to the NSI contribution to the probabilities.

We have first defined a standard probability value corresponding to the SM case with $E_{\bar{\nu}} = 4\,\text{MeV}$ and $L = 1579\,\text{m}$. We then consider the NSI probability in Eq. (4.19) to Eq. (4.21) and calculate the iso-contours in the $(\sin^2\theta_{13},\, \varepsilon)$ plane corresponding to this particular value of the probability. These plots are very useful to see the correlations between $\sin^2\theta_{13}$ and the non-standard parameters. To illustrate the results in the plots of Fig. 4.4 and Fig. 4.5, it is useful to consider the shift in the θ_{13} induced by NSI at first order in ε for each case, as follows from Eq. (4.19) to Eq. (4.21) and given by:

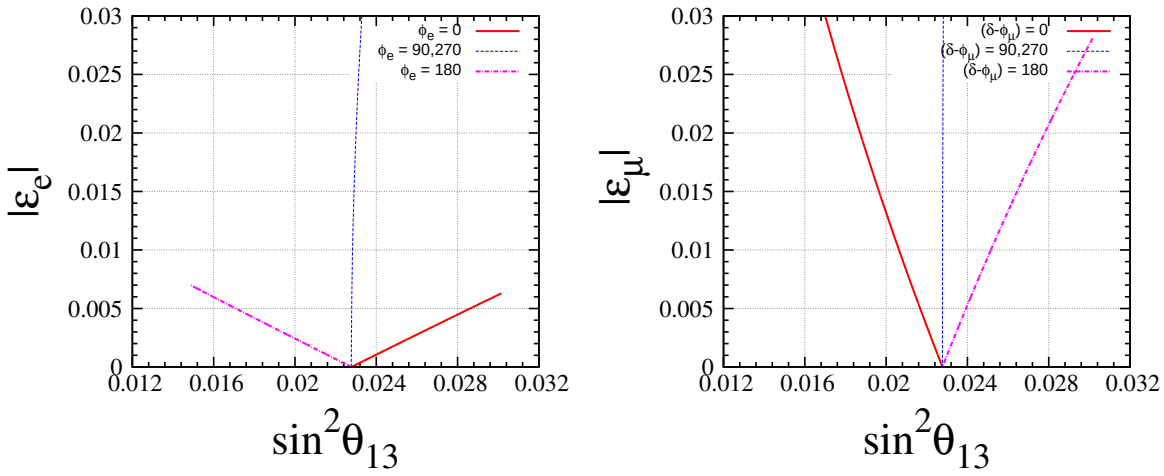

Figure 4.4: Iso-probability contours varying ε_e (left panel) and $\varepsilon_{\mu,\tau}$ (right panel) for different values of ϕ_e and $(\phi_{\mu,\tau} - \delta)$ in degrees, respectively.

- electron flavor case

$$\tilde{s}^2_{13} \approx s^2_{13} - \frac{|\varepsilon_e| \cos\phi_e}{\sin^2 \Delta_{31}} \ . \tag{4.22}$$

- muon/tau flavor case

$$\tilde{s}^2_{13} \approx s^2_{13} + 2 s_{13} s_{23} |\varepsilon_{\mu,\tau}| \cos\left(\delta - \phi_{\mu,\tau}\right) \ . \tag{4.23}$$

- flavor universal (FU) case

$$\tilde{s}^2_{13} \approx s^2_{13} - \frac{|\varepsilon| \cos\phi}{\sin^2 \Delta_{31}} + 4 s_{13} s_{23} |\varepsilon| \cos\left(\delta - \phi\right) \ . \tag{4.24}$$

For the electron case in the left panel of Fig. 4.4 we find correlations (anti-correlations) between the NSI magnitude and the reactor mixing depending if the cosine of the new phase value is positive (negative). This behavior is clear from the shift function in Eq. (4.22). The opposite behavior is shown in the right panel of the same figure. Notice the relative sign in the NSI term in Eq. (4.23) with respect to the equivalent equation for the electron case. Finally, we can see that the muon case allows large values of the NSI couplings compared with the electron case, for the given set of standard oscillation parameters.

The flavor universal case is explored in Fig. 4.5 and can be described with the expression in Eq. (4.24). As we mentioned before, in this case the two phases, δ and ϕ, affect the standard

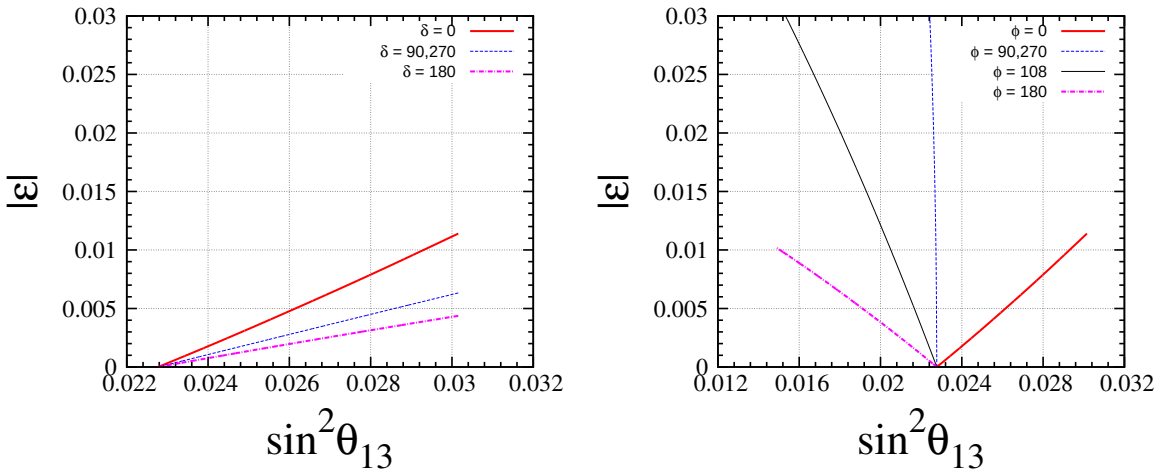

Figure 4.5: Iso-probability plot for the flavor universal case varying δ phase with $\phi_\alpha = 0$ (left panel) and varying ϕ_α with $\delta = 0$ (right panel).

probability in a different way because both enter independently in the probability expression. The effect of the Dirac (new NSI) phase is shown in the left (right) panel. In the left panel, independently of the Dirac phase value, we obtain only positive correlations between the two parameters, implying the relation:

$$\frac{1}{\sin^2 \Delta_{31}} > 4 s_{13} s_{23} \cos\delta \,. \tag{4.25}$$

Since there is no dependence on the NSI parameters, this relation is satisfied in all cases for the given parameters, at least at first order in ε. Furthermore, this result is compatible with the difference in tilts between iso–probability contours for the electron and the muon case in Fig. 4.4. In the case of the right panel in Fig. 4.5, when $\delta = 0$, we have correlation (anti-correlations) when the cosine of the new phase is positive (negative), what is clear from Eqs. 4.24 and 4.25.

In summary, we have obtained correlations between the reactor angle and the NSI couplings in those cases where the 'non-oscillating' NSI term dominates, while anti-correlations were obtained when the NSI oscillating term contributes to the total probability. Those terms were defined in the general probability in Eq. (4.17). Notice that in the flavor universal case, which receives both contributions, we always obtain correlations no matter the Dirac phase value, as shown in the left panel of Fig. 4.5. On the other side, when varying the new phase, we have

both behaviors, correlations and anti-correlations (see right panel of Fig. 4.5). This shows that the results depend strongly on the new phase values, as it will be reflected in the analysis of Daya Bay data.

4.4 Bounds on NSI from Daya Bay data

In this section we use the Daya Bay experiment data as explained in section 1.5.2 to test the sensitivity to NSI at reactors. Initially we will use the χ^2 function defined in Eq. (1.65), fixing the total normalization uncertainty a to zero. In this approximation, we are then assuming the reactor fluxes are known with infinite precision. Later in section 4.5 we will allow for a constrained flux normalization, leading the a parameter to vary freely.

In all our calculation, we have assumed maximal 2-3 mixing. We have initially marginalized over the atmospheric splitting by adding a penalty to the χ^2 function accounting for the current relative error on this parameter: $\Delta m^2_{31}/\delta\left(\Delta m^2_{31}\right) = 3\%$ where $\delta\left(\Delta m^2_{31}\right)$ is the 1σ error in the determination of Δm^2_{31}. We applied this analysis to the simplest case with the Dirac and new phase fixed to zero. Since the atmospheric splitting showed no impact on the analysis, along this chapter we have fixed its value to the best fit point in Ref. [1].

In this section we will present the bounds on the NSI couplings we have obtained using current Daya Bay reactor data Ref. [35]. For definiteness, we will start considering only the couplings relative to electron neutrinos: ($|\varepsilon_e|$,ϕ_e), fixing all the other NSI parameters to zero. Next we will do the same for ($|\varepsilon_\mu|$,ϕ_μ) and ($|\varepsilon_\tau|$,ϕ_τ), equivalent for a maximal θ_{23}. Finally, we will consider the possibility of having all NSI couplings simultaneously with the same magnitude: $\varepsilon_e = \varepsilon_\mu = \varepsilon_\tau$. In all cases we will discuss the bounds arising from Daya Bay data in comparison with existing bounds. We will also consider the robustness of the θ_{13} measurement by Daya Bay in the presence of NSI. Finally we will discuss how the results obtained in our analysis are strongly correlated with the treatment of the total normalization of reactor neutrino events in the statistical analysis of Daya Bay data.

4.4.1 Constraints on electron-NSI couplings

Here we present the constraints on the electron NSI couplings allowed by Daya Bay data. We compare our limits with the existing values in the literature.

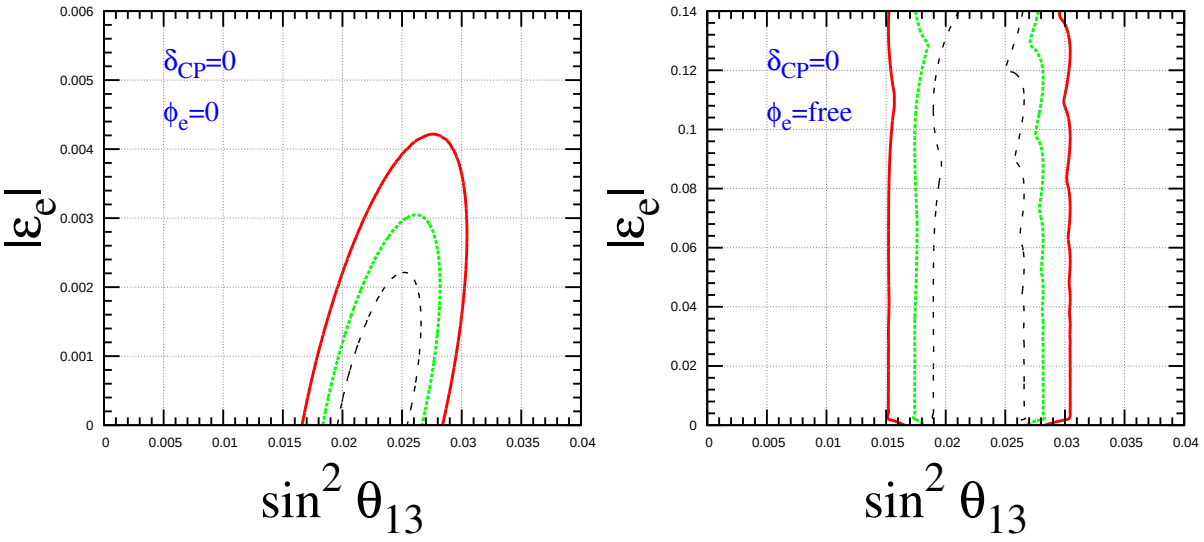

Figure 4.6: Allowed region in the $\sin^2\theta_{13}$ - $|\varepsilon_e|$ plane. Left panel is obtained with $\phi_e = 0$, while in the right panel ϕ_e is marginalized, varying freely between -π and π. The regions correspond to 68% (black dashed line), 90% (green line) and 99% C.L. (red line) for 2 d.o.f.

As discussed before, in this case the value of the phase δ is irrelevant since it does not enter in the probability expression. Then, we have three free parameters, the NSI magnitude $|\varepsilon_e|$ and phase ϕ_e and the reactor mixing angle θ_{13}.

In the left panel of Fig. 4.6 we can see how current Daya Bay data constrain very strongly the magnitude of the NSI coupling ε_e:

$$|\varepsilon_e| < 2.4 \times 10^{-3} \quad (90\%\,\text{C.L.} \quad \text{for 1 d.o.f}) \,, \tag{4.26}$$

improving the current bound [147]:

$$|\varepsilon^{udV}_{e\alpha}| < 0.041 \quad (90\%\,\text{C.L.}) \tag{4.27}$$

in one order of magnitude.

However, as it can be seen in the right panel of Fig. 4.6, this strong bound disappears once the phase ϕ_e is allowed to vary freely. This happens because for $\phi_e = \pi/2$ and $3\pi/2$, the linear term in ε_e in the neutrino survival probability cancels out (see Eq. (4.19)). In this case, the sensitivity to $|\varepsilon_e|$ is drastically reduced and therefore no bound can be obtained from reactor data.

The presence of this NSI coupling results in a slightly wider allowed range for the reactor

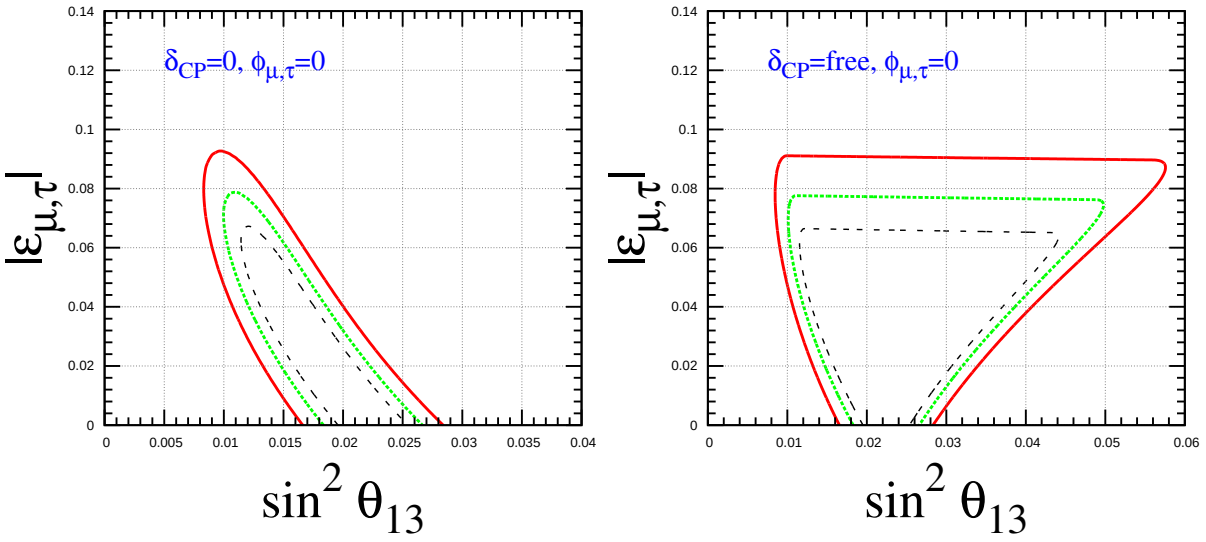

Figure 4.7: Allowed region in the $\sin^2\theta_{13}$ - $|\varepsilon_x|$ plane, with x=μ,τ. Left panel is obtained switching the relevant phase (δ - ϕ_x) to zero, while in the right panel (δ - ϕ_x) is marginalized, varying freely between -π and π. The regions correspond to 68% (black dashed line), 90% C.L (green line) and 99% C.L (red line) for 2 d.o.f.

mixing angle:

$$0.019 \leq \sin^2\theta_{13} \leq 0.027 \quad (90\%\,\text{C.L.} \quad \text{for 1 d.o.f}) \,, \tag{4.28}$$

that is the same for both panels in Fig. 4.6. This range has to be compared with the allowed range in absence of NSI:

$$0.019 \leq \sin^2\theta_{13} \leq 0.026 \quad (90\%\,\text{C.L.} \quad \text{for 1 d.o.f}) \,. \tag{4.29}$$

From the left panel in Fig. 4.6, we can confirm the behaviors shown by the iso-probability curves in section 4.3.2. The larger inner band on θ_{13} appears because the presence of a non-zero ε_e term has to be compensated with a larger value of θ_{13}.

With respect to the iso-probabilities in Fig. 4.4, in the right panel of Fig. 4.6 we find neither correlations nor anti-correlations when the new phase is varying. This is because in the χ^2 marginalization, the phase takes values to reduce the NSI contribution given only by the 'non-oscillatory' term.

4.4.2 Constraints on muon/tau-NSI couplings

Here we present the constraints on the muon/tau NSI couplings allowed by Daya Bay data. We compare our limits with the existing values in the literature.

In this case the phases δ and ϕ_x do not appear separately in the expression of the survival probability in Eq. (4.20). Therefore, it is enough to consider the variation of the effective phase (δ - ϕ_x).

After applying the same procedure as as for the electron case, here we get the bound on the muon/tau NSI coupling fixing the phases to zero:

$$|\varepsilon_{\mu,\tau}| < 7.0 \times 10^{-2} \quad (90\%\,\text{C.L.} \quad \text{for 1 d.o.f}) \ . \tag{4.30}$$

In this case reactor data do not improve present constraints on the NSI couplings [147]:

$$|\varepsilon_{e\mu}^{udL}| < 0.026 \, , |\varepsilon_{e\mu}^{udR}| < 0.037 \quad (90\%\,\text{C.L.}) \tag{4.31}$$

However, either here as well as in the derivation of the existing bounds in Ref [148] some assumptions have been done and then they can be regarded as complementary bounds coming from different data sets.

From the left panel in figure 4.7, we can confirm the behaviors shown by the iso-probability curves in section 4.3.2. The presence of a non-zero ε_μ term requires smaller values of θ_{13} (anti-correlations). The results in the right panel are also in agreement with the iso-probability contours in the right panel of Fig. 4.4 where, due to the variation of the Dirac phase, we find correlations and anti-correlations. From Eq. (4.20) we notice that there is a contribution coming from the 'non-oscillatory' term that can not be canceled out with any value of the phase since it does not depend on the phases. Therefore, we also expect the shown correlations between the reactor angle and the NSI couplings that are usual when the 'non-oscillatory' term is important. Notice that, differently to the electron case, here the variation of the phase δ does not spoil the NSI constraint but instead it requires a larger range for the reactor angle, as shown in table 4.1.

4.4.3 Constraints for the universal-NSI case

As mentioned in section 4.3.2, in the flavor universal case there is one extra free parameter with respect to the electron and muon/tau case, Since in this case the NSI and the Dirac

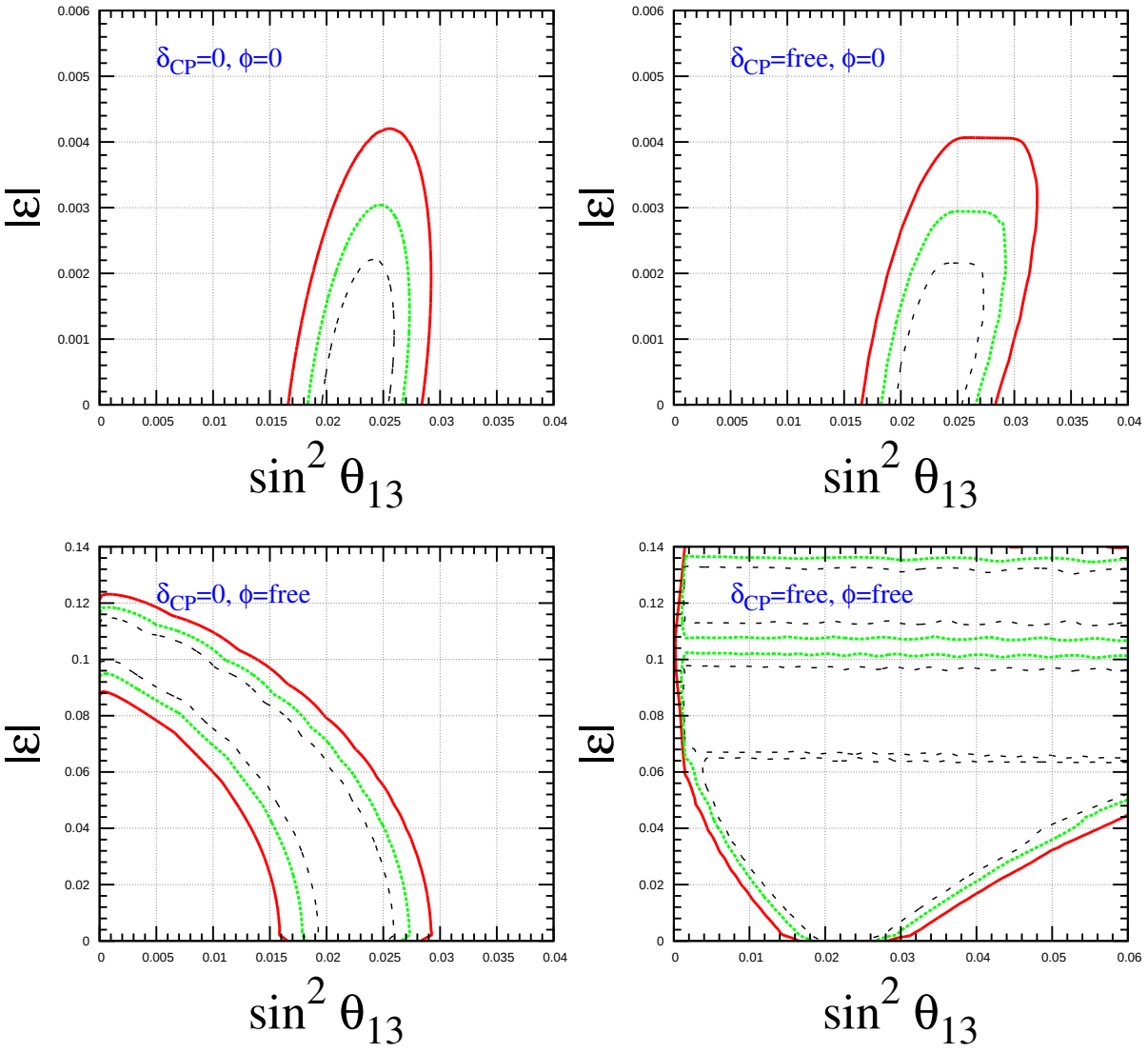

Figure 4.8: Allowed region in the $\sin^2\theta_{13}$ - $|\varepsilon|$ plane for different assumptions concerning the phases δ and ϕ. Upper-left panel is obtained switching all phases to zero, whereas in the upper-right panel $\phi = 0$ and δ is left free. In the lower-left panel δ is taken equal to zero while ϕ has been marginalized. Finally, in the lower-right panel the two phases have been allowed to vary between -π and π. The convention for the lines is the same as in Fig. 4.6

phases are independent. The plots in Fig. 4.8 show the effect of the phases. In the upper left panel we show the real case, which is strongly constrained, as in the case of varying the Dirac phase in the upper right panel. However, when allowing for a variation of the new phase (fixing the Dirac phase to zero), we found a less constrained region in the lower left panel. Finally, when varying both phases, all the parameter region is allowed, and we can not find

any constraint on the NSI coupling.

The upper left panel of Fig. 4.8 is equivalent to the electron case in the left panel of Fig. 4.6, as it should be, because there the NSI effect comes from the 'non-oscillatory' term present in the electron case (see Eq. (4.19)). In the case of the upper right panel, it corresponds to the expected case in the iso-probability plot in the left panel of Fig. 4.5. As commented before, we have only correlations because the main contribution comes from the 'non-oscillatory' term; were the relation in Eq. (4.25) is still valid even in the rate analysis. noticed that here it is even more evident than in the right panel of Fig. 4.7, the variation of the Dirac phase does not spoil the constraint on the NSI coupling.

Keeping in mind that in the flavor universal case the NSI couplings contribute with both terms, oscillatory and 'non-oscillatory', the lower right panel of Fig. 4.8 is not intuitively expected. However, here we have enough freedom in the new phase ϕ to almost cancel out the 'non-oscillatory' term, explaining the anti-correlations between θ_{13} and ε observed here. This behavior is confirmed at the probability level in the right panel of Fig. 4.5 for the value $\phi = 108^\circ$ in the black curve.

In the table 4.1 we summarize the bounds on the NSI parameters for the three cases: electron, muon/tau and flavor universal, discussed along this section. Also, we quoted the reactor mixing angle variation due the NSI coupling values allowed by the Daya Bay data. Before closing this section, we want to stress on the assumptions we have made so far regarding the Daya Bay analysis of data. In particular, we have dropped out the pull parameter that accounts for the free normalization variation in the standard Daya Bay analysis. However, this assumption ignores all the possible sources of systematical errors that contribute to the total normalization uncertainty in the event calculation, mainly the total normalization or the reactor flux.

Reactor neutrino fluxes were recently recalculated [30, 31], obtaining an increase in the average neutrino flux of about 3 percent compared to previous calculations [149]. Considering the new predicted fluxes, there is a discrepancy between the events observed over expected in very short baseline reactors when the rate is calculated with the new flux. This discrepancy is known as the reactor neutrino anomaly [149]. However, large uncertainties in the conversion from the fission beta spectra to the anti-neutrino neutrino spectra that lead to the reactor anomaly might affect the accuracy to infer the anomaly [150]. As a result, the precision int the

phases	$\sin^2\theta_{13}$	ε
electron-type NSI coupling		
$\delta = \phi_e = 0$	$0.019 \leq \sin^2\theta_{13} \leq 0.027$	$\lvert\varepsilon_e\rvert \leq 0.0024$
$\delta = 0$, ϕ_e free	$0.019 \leq \sin^2\theta_{13} \leq 0.027$	$\lvert\varepsilon_e\rvert$ unbound
muon-tau type NSI couplings		
$\delta = \phi_{\mu,\tau} = 0$	$0.011 \leq \sin^2\theta_{13} \leq 0.026$	$\lvert\varepsilon_{\mu,\tau}\rvert \leq 0.070$
$(\delta - \phi_{\mu,\tau})$ free	$0.011 \leq \sin^2\theta_{13} \leq 0.045$	$\lvert\varepsilon_{\mu,\tau}\rvert \leq 0.069$
universal NSI couplings		
$\delta = \phi_\alpha = 0$	$0.019 \leq \sin^2\theta_{13} \leq 0.026$	$\lvert\varepsilon\rvert \leq 0.0024$
δ free, $\phi_\alpha = 0$	$0.019 \leq \sin^2\theta_{13} \leq 0.028$	$\lvert\varepsilon\rvert \leq 0.0023$
$\delta = 0$, ϕ_α free	$\sin^2\theta_{13} \leq 0.026$	$\lvert\varepsilon\rvert \leq 0.116$
δ and ϕ_α free	$\sin^2\theta_{13}$ unbound	$\lvert\varepsilon\rvert$ unbound

Table 4.1: 90% C.L. bounds (1 d.o.f) on $\sin^2\theta_{13}$ and the NSI couplings from Daya Bay data taking fixed normalization in the statistical analysis ($a = 0.$)

anti-neutrino flux determination can not be better than 4%. The uncertainties in the absolute normalization in reactor fluxes are then larger than 4% [149]. We will evaluate the impact of having a total normalization error in the reactor fluxes in the constraints we have found for the NSI.

4.5 Bounds on NSI from Daya Bay data with free normalization

Up to here we have considered fixed normalization in the statistical analysis of Daya Bay reactor data. However, most of the current analysis of reactor data consider a free-normalization factor that may account for the uncertainties in the total event number normalization coming from the reactor neutrino flux prediction, the detection cross section and other systematical errors that contribute to the total event normalization errors.

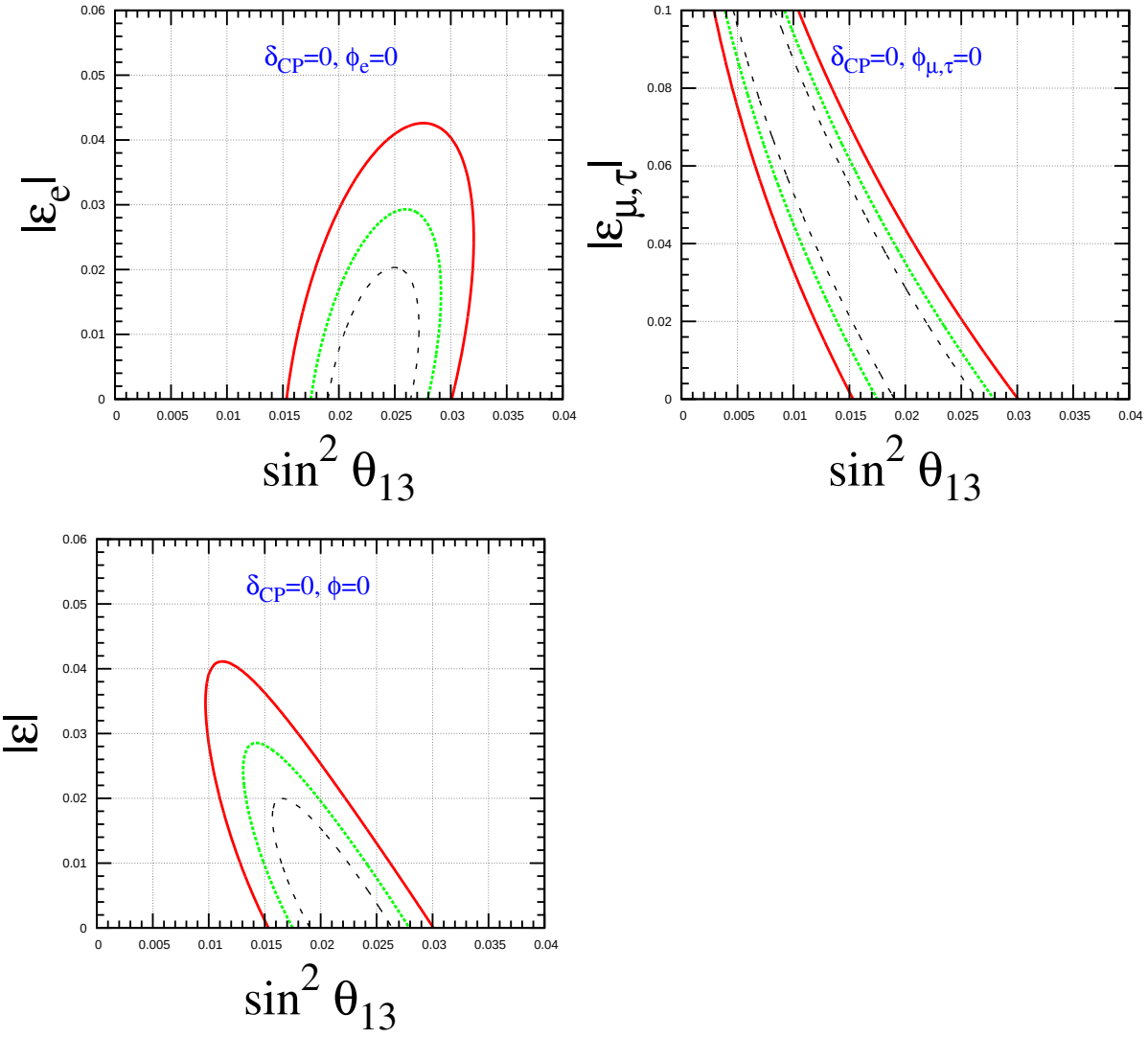

Figure 4.9: Same as Fig. 4.6, Fig. 4.7 and Fig. 4.8 for the three different cases analyzed in the previous section with all phases equal to zero, and 5% uncertainty in the total normalization.

Here we used the following version of the χ^2 function:

$$\begin{aligned}\chi^2 &= \sum_{d=1}^{6} \frac{\left[M_d - T_d\left(1 + a + \sum_r \omega_r^d \alpha_r + \xi_d\right) + \beta_d\right]^2}{M_d + B_d} \\ &+ \sum_{r=1}^{6} \frac{\alpha_r^2}{\sigma_r^2} + \sum_{d=1}^{6}\left(\frac{\xi_d^2}{\sigma_d^2} + \frac{\beta_d^2}{\sigma_B^2}\right) + \left(\frac{a}{\sigma_a}\right)^2 ,\end{aligned}$$

where, differently to the free normalization analysis shown in section 1.5.2 we have added a penalty in the χ^2 in order to account for the already mentioned uncertainty in the absolute normalization that we will conservatively assume of the order of 5%.

In order to see how the constraints we have found in the last section change when we

Case	$\sin^2\theta_{13}$	ε
$\delta = \phi_e = 0$	$0.019 \leq \sin^2\theta_{13} \leq 0.028$	$\lvert\varepsilon_e\rvert \leq 0.022$
$\delta = \phi_{\mu,\tau} = 0$	$\sin^2\theta_{13} \leq 0.027$	$\lvert\varepsilon_{\mu,\tau}\rvert \leq 0.198$
$\delta = \phi_\alpha = 0$	$0.015 \leq \sin^2\theta_{13} \leq 0.027$	$\lvert\varepsilon\rvert \leq 0.022$

Table 4.2: 90% C.L. bounds (1 d.o.f) on $\sin^2\theta_{13}$ and the NSI couplings from Daya Bay data assuming a 5% error in the normalization pull in the statistical analysis.

include the error in the absolute normalization, we repeated the data analysis for the three considered cases with the phases set to zero, because these are the cases that produced the tightest bounds. In Fig. 4.9 we show the three cases: electron, muon/tau and flavor universal in the left, middle and right panels. We can see that the bounds are approximately one order of magnitude less restrictive than the ones in the last section, comparing the bounds in table 4.2 with the ones in table 4.1. In summary, the constraints we have found so far highly depend on the systematic errors over the total normalization, mainly the uncertainty on the total normalization of the reactor neutrino fluxes. A better determination of this normalization will improve the constraints quoted in table 4.2. Still, with the current data and 5% estimated systematic error in the total normalization, we have found that the constraints for the case of electron and FU are at the percent level, competitive with the constraints found in the literature using other data sets [148].

Conclusions

In the first part of the thesis, we have simulated individual short-baseline reactor and long-baseline accelerator experiments in the context of the three neutrino oscillation framework. Here we have updated the global fit of neutrino oscillations given in Ref. [1] by including the recent measurements performed over the last two years. These include the updated measurements of reactor anti-neutrino disappearance reported by Daya Bay and RENO, together with the latest long–baseline appearance and disappearance data from T2K and MINOS. In addition, we have also included the revised data form the third solar phase of Super-Kamiokande, (SK-III), as well as new solar results from the fourth phase of Super-Kamiokande, (SK-IV). We find that for normal mass ordering the global best fit value of the atmospheric angle θ_{23} is consistent with maximal mixing at 1σ, while for the inverted spectrum maximal mixing appears at 1.3σ. We note that the T2K disappearance data now provide the most sensitive measurement of the atmospheric mixing angle θ_{23}. Needless to say, the determination of a sizeable θ_{13} value is crucial towards a new era of CP violation searches in neutrino oscillations [7, 97] and it will also help determining the neutrino mass hierarchy. We also determined the impact of the new data upon all the other neutrino oscillation parameters, with emphasis on the increasing sensitivity to the CP violation phase δ. The latter follows from the complementarity between accelerator and reactor data and leads to preferred values of the CP phase around 1.5π.

In the second chapter, we have proposed a minimal extension of the simplest A_4 flavor model originally presented by Babu, Ma and Valle. Our modified model can induce a nonzero

θ_{13} value, as required by recent neutrino oscillation data coming from reactors and accelerators. We have shown how the predicted correlation between the atmospheric mixing angle θ_{23} and the magnitude of θ_{13} lead to an allowed region that is substantially smaller than indicated by model-independent neutrino oscillation global fits. Moreover, our proposed scheme establishes a correlation between CP violation in neutrino oscillations and the octant of the atmospheric mixing parameter θ_{23}. In particular one finds that, for maximal atmospheric mixing as well as for θ_{23} in the first octant, one necessarily gets CP violation. Currently we find that both cases are consistent at the 1σ level with the global neutrino oscillation analysis of Ref. [1]. We also stress that ours is a quasi-degenerate neutrino scenario. Recent restrictions on the absolute neutrino mass from cosmological measurements, in particular from the Planck collaboration [10] indicate values for the parameter δ characterizing slepton radiative corrections for which lepton flavour violation induced by supersymmetric particle exchanges is expected to lie at the limits. That would provide another complementary way to probe this model.

The physics responsible for neutrino masses could lie at the TeV scale. In this case it is very unlikely that neutrino masses are not accompanied by non-standard neutrino interactions that could reveal novel features in neutrino propagation, production and detection. Similarly, lepton flavor violation can also take place in processes involving the charged leptons. Within low-scale seesaw scenarios, such as the inverse and linear type-I seesaw, we have found that non-unitarity in the lepton mixing matrix up to the percent level in some cases, is consistent with the constraints that follow from lepton flavor violation searches in the laboratory. This conclusion holds even within the simple "minimal flavor violation" assumptions we have made. As a result, the upcoming long–baseline neutrino experiments [97] do provide an important window of opportunity to perform complementary tests of lepton flavor violation in neutrino propagation and to probe the mass scale characterizing the seesaw mechanism.

Finally, in the last chapter, CC-like NSI have been introduced for the case of antineutrino production and detection through normal and inverse β-decay. We used the Daya Bay reactor data to constrain the NSI couplings affecting neutrino detection and production, as well as the deviations in θ_{13} determination induced by the presence of NSI. We found that, for the case of non-standard ν_e couplings, the bounds we obtain are stronger than previous ones in the literature. For the $\nu_{\mu,\tau}$ NSI couplings, though, our limits are of the same order as the current

bounds. In all cases, however, we noticed that the presence of the new NSI phases may relax our constraints dramatically. We also showed that the constraints on the NSI couplings *strongly* depend on the assumptions about the absolute normalization uncertainty adopted in the statistical analysis of data. For a conservative error of 5%, the bounds could relax up to an order of magnitude for the most constrained cases. In this case, we found that the allowed magnitude of the NSI couplings can be as large as $\sim 10^{-2}$.

Appendices

APPENDIX A

$\mu \to e\gamma$ Branching ratio

Here we derive in detail the expression for the loop form factor that enters in the $\mu \to e\gamma$ branching ratio.

Assuming that the half-width of the generic process $l_i \to l_j\gamma$ is given by [127]:

$$\Gamma(l_i \to l_j\gamma) = \frac{\alpha_W^3 s_W^2}{256\pi^2}\frac{m_{l_i}^5}{M_W^4}|G_{ij}^W|^2 \ , \tag{A.1}$$

then, we just rewrite the pre-factor:

$$\begin{aligned}\frac{\alpha_W^3 s_W^2}{256\pi^2}\frac{1}{M_W^4} &= \frac{\alpha^3}{(s_W^2)^3}\frac{s_W^2}{256\pi^2}\frac{1}{M_W^4} = \frac{\alpha^3}{(s_W^2)^2}\frac{1}{256\pi^2}\frac{1}{M_W^4} \\ &= \frac{\alpha^3}{4\cdot 64\,\pi^2}\left(\frac{g^2}{e^2}\right)^2\frac{1}{M_W^4}\end{aligned}$$

where we have used $e = g\,s_W$. Now we used the known relation between the W boson mass and the Fermi constant G_F:

$$\frac{G_F}{\sqrt{2}} = \frac{g^2}{8M_W^2}$$

and we get:

$$\begin{aligned}\frac{\alpha_W^3 s_W^2}{256\pi^2}\frac{1}{M_W^4} &= \frac{\alpha^3}{4\pi^2}\left(\frac{1}{e^2}\right)^2\frac{G_F^2}{2} = \frac{\alpha^3}{4\pi^2}\left(\frac{1}{4\pi\,\alpha}\right)^2\frac{G_F^2}{2} = \frac{\alpha}{2\cdot 4^3\cdot\pi}\frac{G_F^2}{\pi^3} \\ &= \frac{3\alpha}{2\pi}\frac{G_F^2 m_\mu^5}{3\cdot 4^3}\frac{1}{m_\mu^5} = \frac{3\alpha}{2\pi}\frac{\Gamma(\mu\to e\nu\overline{\nu})}{m_\mu^5}.\end{aligned}$$

Together with Eq. (A.1) we can write:

$$Br(\mu \to e\gamma) = \frac{\Gamma(\mu \to e\gamma)}{\Gamma(\mu \to e\nu\overline{\nu})} = \frac{3\,\alpha}{2\pi}|G_{21}^{W}|^2. \tag{A.2}$$

Until now we have just rewritten Eq. (A.1) for comparison with other results from the literature. In order to determine the loop form factor encoded in G_{21}^{W} we follow the Cheng and Li solution [151] for the branching ratio:

$$Br(\mu \to e\gamma) = \frac{\Gamma(\mu \to e\gamma)}{\Gamma(\mu \to e\nu\overline{\nu})} = \frac{3\,\alpha}{32\pi}\left|2\sum_i U_{ei}^{*}U_{\mu i}\, g\left(\frac{m_i^2}{M_W^2}\right)\right|^2 , \tag{A.3}$$

where the form factor $g(x)$ is given by:

$$\begin{aligned} g(x) &= \int_0^1 d\alpha\, \frac{(1-\alpha)}{(1-\alpha)+\alpha\, x}\left[2(1-\alpha)(2-\alpha)+\alpha(1+\alpha)x\right] \\ &= \frac{1}{6(1-x)^4}(10-43x+78x^2-49x^3+18x^3\ln x+4x^4)\,. \end{aligned} \tag{A.4}$$

Note that the sign in front of the logarithmic term was incorrectly written in [151] as mentioned by the authors in a later work [129]. Finally, comparing Eq. (A.2) with Eq. (A.3) we find:

$$G_{21}^{W} = \sum_i U_{ei}^{*}U_{\mu i}\left[\frac{1}{2}g\left(\frac{m_i^2}{M_W^2}\right)\right] \equiv \sum_i U_{ei}^{*}U_{\mu i}G_{\gamma}^{W}\left(\frac{m_i^2}{M_W^2}\right),$$

which allow us to define a form factor according to Eq. (A.2):

$$G_{\gamma}^{W}(x) = \frac{1}{12(1-x)^4}(10-43x+78x^2-49x^3+18x^3\ln x+4x^4). \tag{A.5}$$

The same form factor $G_{\gamma}^{W}(x)$ in Eq. (A.5) was found as a limiting case in a more general study of the process $f_1 \to f_2\gamma$ by Lavoura [130]. We refer the reader to the right-hand-side of Eq. (68) in the published version of this article. Still there might exist an ambiguity with a global constant when computing the branching ratio, but this constant can be verified from the result for SM neutrinos in Eq. (A.7).

A.1 Limiting cases

Comparing the neutrino masses with the W boson mass we can define three regimes:

- Low mass limit $m_i \ll M_W$. In this case the form factor is approximately given by

$$G_{\gamma}(x) \approx \frac{5}{6} - \frac{x}{4} \tag{A.6}$$

and in the case of the unitary mixing, the branching ratio is given by Eq. (A.2):

$$Br(\mu \to e\gamma) \approx \frac{3\,\alpha}{2\pi}\left|\sum_i U_{ei}^* U_{\mu i}\left(-\frac{x}{4}\right)\right|^2 = \frac{3\,\alpha}{32\pi}\left|\sum_i U_{ei}^* U_{\mu i}\left(\frac{m_i}{M_W}\right)^2\right|^2 \tag{A.7}$$

which is a well known result [152, 153]. With only active neutrinos the branching ratio is suppressed by the neutrino masses. In this case $Br(\mu \to e\gamma) < 10^{-40}$ [102]. However, in general the mixing is non unitary so the finite term in the form factor will contribute to the branching ratio as much as the extra heavy neutrinos. In this case it is expected a large lepton flavor violation that will saturate the current bound.

- Intermediate limit: $m_i \approx M_W$, the form factor is given by:

$$G_\gamma(x) \approx \frac{17}{24} + \frac{3(1-x)}{40} \tag{A.8}$$

- Large mass limit: $m_i \gg M_W$. In this case the form factor is approximately given by:

$$G_\gamma(x) \approx \frac{1}{3} + \frac{3\log(x)}{2x}. \tag{A.9}$$

and the branching ratio is given by Eq. (A.2):

$$\begin{aligned} Br(\mu \to e\gamma) &\approx \frac{3\,\alpha}{2\pi}\left|\sum_i K_{ei}^* K_{\mu i}\left(\frac{1}{3} + \frac{3\log(x)}{2x}\right)\right|^2 \\ &\approx \frac{3\,\alpha}{2\pi}\left|\sum_i K_{ei}^* K_{\mu i}\left[\frac{1}{3} + \frac{3M_W^2}{2m_i^2}\log\left(\frac{m_i}{M_W}\right)^2\right]\right|^2 . \end{aligned}$$

This limit is interesting for heavy neutrinos, because it allows us to estimate a constraint on the active-heavy mixing. Assuming that for all neutrinos $m_i \gg M_W$ then we have:

$$\left|\sum_i K_{ei}^* K_{\mu i}\right| \approx \sqrt{\frac{3^2\cdot 2\pi}{3\alpha} Br(\mu \to e\gamma)} \lesssim 4\times 10^{-5}, \tag{A.10}$$

where we have used the latest limit for $Br(\mu \to e\gamma) < 5.7\times 10^{-13}$ from the MEG collaboration [116].

Note that the limit in Eq. (A.10) is just an estimation and, lower limits can be found in low scale seesaw models as shown in section 3.7.

APPENDIX B

Neutrino oscillation probabilities in presence of NSI for other relevant cases

In this appendix we derive other probability expressions not considered in chapter 4. Two additional cases are considered. The first one with only NSI at source and the second case considering the same NSI strength at the source and detector with different phases.

B.1 Case 2 : non-standard interaction at production only

In this case, the effect of NSI is only considered at production what implies:

$$\varepsilon^{d}_{\alpha e} = 0 \quad \text{and} \quad \varepsilon^{s}_{e\alpha} = |\varepsilon_\alpha| \mathrm{e}^{\mathrm{i}\phi_\alpha} \tag{B.1}$$

$$\begin{aligned} P_{\bar{\nu}^s_e \to \bar{\nu}^d_e} \simeq\ & P^{SM}_{\bar{\nu}^s_e \to \bar{\nu}^d_e} + |\varepsilon_e|^2 + 2|\varepsilon_e| \cos\phi_e \\ +\ & 2s_{13}\left[s_{23}|\varepsilon_\mu| \sin(\delta - \phi_\mu) + c_{23}|\varepsilon_\tau| \sin(\delta - \phi_\tau)\right] \sin\left(2\Delta_{31}\right) \\ -\ & 4s_{13}\left[s_{23}|\varepsilon_\mu| \cos(\delta - \phi_\mu) + c_{23}|\varepsilon_\tau| \cos(\delta - \phi_\tau)\right] \sin^2\left(\Delta_{31}\right) \\ +\ & \sin 2\theta_{12}\left[-c_{23}|\varepsilon_\mu| \sin\phi_\mu + s_{23}|\varepsilon_\tau| \sin\phi_\tau\right] \sin\left(2\Delta_{21}\right) \end{aligned} \tag{B.2}$$

B.2 Case 3: Same-size production and detector effect with different phases

In this case, we consider the same NSI strength at the source and detector with different phases, what implies:

$$\varepsilon^s_{e\alpha} = |\varepsilon_\alpha| e^{i\phi^s_\alpha} \quad \text{and} \quad \varepsilon^d_{\alpha e} = |\varepsilon_\alpha| e^{i\phi^d_\alpha} \tag{B.3}$$

$$P_{\bar{\nu}^s_e \to \bar{\nu}^d_e} \simeq P^{SM}_{\bar{\nu}_e \to \bar{\nu}_e} + P^{\text{NSI-IIb}}_{\text{non-osc}} + P^{\text{NSI-IIb}}_{\text{osc-atm}} + P^{\text{NSI-IIb}}_{\text{osc-solar}} \tag{B.4}$$

with:

$$\begin{aligned}
P^{\text{NSI-IIb}}_{\text{non-osc}} &= 2\left\{|\varepsilon_e|\left(\cos\phi^d_e + \cos\phi^s_e\right) + |\varepsilon_e|^2\left[1 + \cos(\phi^d_e - \phi^s_e) + \cos(\phi^d_e + \phi^s_e)\right]\right. \\
&+ \left.|\varepsilon_\mu|^2\cos(\phi^s_\mu + \phi^d_\mu) + |\varepsilon_\tau|^2\cos(\phi^s_\tau + \phi^d_\tau)\right\} \qquad \text{(B.5)} \\
P^{\text{NSI-IIb}}_{\text{osc-atm}} &= 2\left\{s_{13}s_{23}|\varepsilon_\mu|\left[\sin(\delta - \phi^s_\mu) - \sin(\delta + \phi^d_\mu)\right] + s_{13}c_{23}|\varepsilon_\tau|\left[\sin(\delta - \phi^s_\tau) - \sin(\delta + \phi^d_\tau)\right]\right. \\
&- s^2_{23}|\varepsilon_\mu|^2\sin(\phi^s_\mu + \phi^d_\mu) - c^2_{23}|\varepsilon_\tau|^2\sin(\phi^s_\tau + \phi^d_\tau) \\
&- \left.c_{23}s_{23}|\varepsilon_\mu||\varepsilon_\tau|\left[\sin(\phi^s_\tau + \phi^d_\mu) + \sin(\phi^s_\mu + \phi^d_\tau)\right]\right\}\sin(2\Delta_{31}) \\
&- 4\left\{s_{13}s_{23}|\varepsilon_\mu|\left[\cos(\delta - \phi^s_\mu) + \cos(\delta + \phi^d_\mu)\right] + c_{23}s_{13}|\varepsilon_\tau|\left[\cos(\delta - \phi^s_\tau) + \cos(\delta + \phi^d_\tau)\right]\right. \\
&+ s^2_{23}|\varepsilon_\mu|^2\cos(\phi^s_\mu + \phi^d_\mu) + c^2_{23}|\varepsilon_\tau|^2\cos(\phi^s_\tau + \phi^d_\tau) \\
&+ \left.c_{23}s_{23}|\varepsilon_\mu||\varepsilon_\tau|\left[\cos(\phi^s_\tau + \phi^d_\mu) + \cos(\phi^s_\mu + \phi^d_\tau)\right]\right\}\sin^2(\Delta_{31}) \qquad \text{(B.6)} \\
P^{\text{NSI-IIb}}_{\text{osc-solar}} &= \sin 2\theta_{12}\left[-c_{23}|\varepsilon_\mu|(\sin\phi^s_\mu + \sin\phi^d_\mu) + s_{23}|\varepsilon_\tau|(\sin\phi^s_\tau + \sin\phi^d_\tau)\right]\sin(2\Delta_{21}) \qquad \text{(B.7)}
\end{aligned}$$

B.3 Neutrino states with normalization

The new neutrino favor states, in presence of NSI are normalized as:

$$\begin{aligned}
|\nu^s_\alpha\rangle &= \frac{1}{N^s_\alpha}\left(|\nu_\alpha\rangle + \sum_\gamma \varepsilon^s_{\alpha\gamma}|\nu_\gamma\rangle\right) , \\
\langle\nu^d_\beta| &= \frac{1}{N^d_\beta}\left(\langle\nu_\beta| + \sum_\eta \varepsilon^d_{\eta\beta}\langle\nu_\eta|\right) ,
\end{aligned} \tag{B.8}$$

where the normalization factors are given by:

$$\begin{aligned}
N^s_\alpha &= \sqrt{\left[(1+\varepsilon^s)(1+\varepsilon^{s\dagger})\right]_{\alpha\alpha}} , \\
N^d_\beta &= \sqrt{\left[(1+\varepsilon^{d\dagger})(1+\varepsilon^d)\right]_{\beta\beta}} ,
\end{aligned} \tag{B.9}$$

To see the normalization effect in the probability, we can compute the oscillation probability at zero distance:

$$P_{\nu_\alpha^s \to \nu_\beta^d}(L=0) = \left|\langle \nu_\beta^d | \nu_\alpha^s \rangle\right|^2 = \left| \frac{\delta_{\alpha\beta} + \varepsilon^s_{\alpha\beta} + \varepsilon^d_{\alpha\beta} + \sum_\gamma \varepsilon^s_{\alpha\gamma}\varepsilon^d_{\gamma\beta}}{N^s_\alpha N^d_\beta} \right|^2 . \tag{B.10}$$

For the case I where $\varepsilon^s_{\alpha\gamma} = \varepsilon^{d*}_{\gamma\alpha} = |\varepsilon_{\alpha\gamma}| \exp(i\phi_{\alpha\gamma})$ we find the oscillation amplitude is given by:

$$A_{\alpha\beta}(L=0) = \frac{\delta_{\alpha\beta} + 2\mathcal{R}(|\varepsilon_{\alpha\beta}| \exp i\phi_{\alpha\beta}) + \sum_\gamma |\varepsilon_{\alpha\gamma}||\varepsilon_{\beta\gamma}| \exp\left[i(\phi_{\alpha\gamma} - \phi_{\beta\gamma})\right]}{\sqrt{1 + 2\mathcal{R}(|\varepsilon_{\alpha\alpha}| \exp i\phi_{\alpha\alpha}) + \sum_\gamma |\varepsilon_{\alpha\gamma}|^2}\sqrt{1 + 2\mathcal{R}(|\varepsilon_{\beta\beta}| \exp i\phi_{\beta\beta}) + \sum_\gamma |\varepsilon_{\beta\gamma}|^2}}$$
$$\neq 0 \ . \tag{B.11}$$

In the case $\alpha = \beta = e$, the probability is exactly one, which is the effect of normalizing the states in Eq. (B.8).

Finally, we will explain what happens with the normalization terms in Eq. (B.9) that are in the denominator of the probabilities. When dealing with a non-orthonormal neutrino basis, the normalization of neutrino states affects non only the neutrino survival probability but also the calculation of the neutrino fluxes and cross sections. In Ref. [154] it has been shown that when computing the event number, in a convolution of cross section, reactor flux and oscillation probability, the normalization factors in Eq. (B.9) and in the denominator of Eq. (B.10) cancel out. Therefore, in our case one can make use of an effective survival probability given in Eq. (4.17). This effective probability may take values larger than 1 even though the 'true' probability has been properly normalized. This however, does not affect our simulation since the effect of normalization is cancelled with the neutrino fluxes and cross sections factors.

APPENDIX C

Matrix block diagonalization

We want to diagonalize a general Hermitian matrix of the form

$$Z = \begin{bmatrix} Z_1 & Z_2 \\ Z_2^\dagger & Z_3 \end{bmatrix} , \tag{C.1}$$

where Z_1 and Z_3 are hermitian matrices. This hermitian matrix can be approximately block diagonalized using the method of Ref [155]. To this end we introduce the matrices

$$U = e^{iH}\, V, \quad H = \begin{bmatrix} 0 & S \\ S^\dagger & 0 \end{bmatrix}, \quad V = \begin{bmatrix} V_1 & 0 \\ 0 & V_2 \end{bmatrix}, \tag{C.2}$$

We then require that

$$U^\dagger Z U = \begin{bmatrix} m_1 & 0 \\ 0 & m_2 \end{bmatrix} , \tag{C.3}$$

where $m_{1,2}$ are real and diagonal.

We can explicitly expand U in terms of S:

$$U = \begin{bmatrix} \left(I - \frac{1}{2} S\, S^\dagger + \dots\right) V_1 & i\left(S - \frac{1}{3!} S\, S^\dagger S + \dots\right) V_2 \\ i\left(S^\dagger - \frac{1}{3!} S^\dagger S\, S^\dagger + \dots\right) V_1 & \left(I - \frac{1}{2} S^\dagger\, S + \dots\right) V_2 \end{bmatrix} \equiv \begin{bmatrix} U_a & U_b \\ U_c & U_d \end{bmatrix}. \tag{C.4}$$

In general, replacing U from Eq. (C.4) in the diagonalization condition in Eq. (C.3), produces the following system of equations:

$$\begin{aligned} m_1 &= U_a^\dagger Z_1 U_a + U_c^\dagger Z_2^\dagger U_a + U_a^\dagger Z_2 U_c + U_c^\dagger Z_3\, U_c = U_a^\dagger Z_1 U_a + (U_a^\dagger Z_2 U_c + \text{h.c}) + U_c^\dagger M\, U_c \ , \\ 0 &= U_a^\dagger Z_1 U_b + U_c^\dagger Z_2^\dagger U_b + U_a^\dagger Z_2 U_d + U_c^\dagger Z_3\, U_d = U_a^\dagger Z_1 U_b + U_a^\dagger Z_2 U_d + U_c^\dagger Z_3\, U_d + \mathcal{O}(S^2) \ , \\ m_2 &= U_b^\dagger Z_1 U_b + U_d^\dagger Z_2^\dagger U_b + U_b^\dagger Z_2 U_d + U_d^\dagger Z_3\, U_d = U_b^\dagger Z_1 U_b + (U_b^\dagger Z_2 U_d + \text{h.c}) + U_d^\dagger Z_3\, U_d \ , \end{aligned} \tag{C.5}$$

which are exact relations for m_1 and m_2. To determine S, from the requirement that the off-diagonal sub-blocks vanish (second equation of the system in Eq. (C.5)), it is enough to take the approximations until second order in S in Eq. (C.4). The result is:

$$0 = iZ_1\, S + Z_2 - iS\, Z_3, \tag{C.6}$$

assuming $[Z_1, S] = 0$ or $[Z_3, S] = 0$, we find:

$$iS \approx -Z_2(Z_1 - Z_3)^{-1}, \quad iS^\dagger = (Z_1 - Z_3)^{-1} Z_2^\dagger \tag{C.7}$$

where we have used the fact that $Z_{1,3}$ are hermitian matrices. Replacing Eq. (C.7) in the first relation in Eq. (C.5), we get for the 3×3 block:

$$m_1 \approx V_1^\dagger \left[Z_1 + 2Z_2(Z_1 - Z_3)^{-1} Z_2^\dagger + Z_2(Z_1 - Z_3)^{-1} Z_3 (Z_1 - Z_3)^{-1} Z_2^\dagger \right] V_1 \ . \tag{C.8}$$

Notice that this formula reduces in the limit where $Z_1 = 0$ to the usual seesaw formula (for neutrinos the matrix is symmetric and one should replace the hermitian conjugate with the transpose operation),

$$m_1 \approx V_1^\dagger \left[-Z_2 Z_3^{-1} Z_2^\dagger \right] V_1, \tag{C.9}$$

with $Z_3 = M_R$ and $Z_2 = M_D$.

We finally define

$$m_{3\times 3}^{\text{eff}} \approx Z_1 + 2Z_2(Z_1 - Z_3)^{-1} Z_2^\dagger + Z_2(Z_1 - Z_3)^{-1} Z_3 (Z_1 - Z_3)^{-1} Z_2^\dagger \ . \tag{C.10}$$

Bibliography

[1] D. Forero, M. Tortola, and J. Valle, "Global status of neutrino oscillation parameters after Neutrino-2012," *Phys.Rev.* **D86** (2012) 073012, arXiv:1205.4018 [hep-ph].

[2] D. Forero, M. Tortola, and J. Valle, "Neutrino oscillations refitted," arXiv:1405.7540 [hep-ph].

[3] C. Giunti and C. W. Kim, *Fundamentals of Neutrino Physics and Astrophysics*. Oxford University Press, first ed., 2007.

[4] C. Kim and A. Pevsner, *Neutrinos in physics and astrophysics*, vol. 8. Harwood Academic Publishers, first ed., 1993.

[5] **Particle Data Group** Collaboration, J. Beringer *et al.*, "Review of Particle Physics (RPP)," *Phys.Rev.* **D86** (2012) 010001.

[6] J. Schechter and J. Valle, "Neutrino Masses in SU(2) x U(1) Theories," *Phys.Rev.* **D22** (1980) 2227.

[7] H. Nunokawa, S. J. Parke, and J. W. Valle, "CP Violation and Neutrino Oscillations," *Prog.Part.Nucl.Phys.* **60** (2008) 338–402, arXiv:0710.0554 [hep-ph].

[8] W. Rodejohann and J. Valle, "Symmetrical Parametrizations of the Lepton Mixing Matrix," *Phys.Rev.* **D84** (2011) 073011, arXiv:1108.3484 [hep-ph].

[9] **EXO Collaboration** Collaboration, M. Auger *et al.*, "Search for Neutrinoless Double-Beta Decay in ^{136}Xe with EXO-200," *Phys.Rev.Lett.* **109** (2012) 032505, arXiv:1205.5608 [hep-ex].

[10] **Planck Collaboration** Collaboration, P. Ade *et al.*, "Planck 2013 results. XVI. Cosmological parameters," arXiv:1303.5076 [astro-ph.CO].

[11] H. Nunokawa, V. Semikoz, A. Y. Smirnov, and J. Valle, "Neutrino conversions in a polarized medium," *Nucl.Phys.* **B501** (1997) 17–40, arXiv:hep-ph/9701420 [hep-ph].

[12] L. Wolfenstein, "Neutrino Oscillations in Matter," *Phys.Rev.* **D17** (1978) 2369–2374.

[13] S. Mikheev and A. Y. Smirnov, "Resonance Amplification of Oscillations in Matter and Spectroscopy of Solar Neutrinos," *Sov.J.Nucl.Phys.* **42** (1985) 913–917.

[14] S. Mikheev and A. Y. Smirnov, "Resonant amplification of neutrino oscillations in matter and solar neutrino spectroscopy," *Nuovo Cim.* **C9** (1986) 17–26.

[15] R. Mohapatra and P. Pal, *Massive neutrinos in physics and astrophysics*. World Scientific Pub Co, third ed., 2004.

[16] S. J. Parke, "Nonadiabatic Level Crossing in Resonant Neutrino Oscillations," *Phys.Rev.Lett.* **57** (1986) 1275–1278.

[17] E. K. Akhmedov, R. Johansson, M. Lindner, T. Ohlsson, and T. Schwetz, "Series expansions for three flavor neutrino oscillation probabilities in matter," *JHEP* **0404** (2004) 078, arXiv:hep-ph/0402175 [hep-ph].

[18] A. Cervera, A. Donini, M. Gavela, J. Gomez Cadenas, P. Hernandez, *et al.*, "Golden measurements at a neutrino factory," *Nucl.Phys.* **B579** (2000) 17–55, arXiv:hep-ph/0002108 [hep-ph].

[19] M. Gonzalez-Garcia and M. Maltoni, "Phenomenology with Massive Neutrinos," *Phys.Rept.* **460** (2008) 1–129, arXiv:0704.1800 [hep-ph].

[20] **SNO Collaboration** Collaboration, B. Aharmim *et al.*, "Electron energy spectra, fluxes, and day-night asymmetries of B-8 solar neutrinos from measurements with NaCl dissolved in the heavy-water detector at the Sudbury Neutrino Observatory," *Phys.Rev.* **C72** (2005) 055502, arXiv:nucl-ex/0502021 [nucl-ex].

[21] J. N. Bahcall, A. M. Serenelli, and S. Basu, "New solar opacities, abundances, helioseismology, and neutrino fluxes," *Astrophys.J.* **621** (2005) L85–L88, arXiv:astro-ph/0412440 [astro-ph].

[22] **Super-Kamiokande Collaboration** Collaboration, A. Renshaw *et al.*, "First Indication of Terrestrial Matter Effects on Solar Neutrino Oscillation," *Phys.Rev.Lett.* **112** (2014) 091805, arXiv:1312.5176 [hep-ex].

[23] **SNO Collaboration** Collaboration, B. Aharmim *et al.*, "Low Energy Threshold Analysis of the Phase I and Phase II Data Sets of the Sudbury Neutrino Observatory," *Phys.Rev.* **C81** (2010) 055504, arXiv:0910.2984 [nucl-ex].

[24] T. Kajita, "Atmospheric neutrinos," *Adv.High Energy Phys.* **2012** (2012) 504715.

[25] M. Honda, T. Kajita, K. Kasahara, and S. Midorikawa, "Improvement of low energy atmospheric neutrino flux calculation using the JAM nuclear interaction model," *Phys.Rev.* **D83** (2011) 123001, arXiv:1102.2688 [astro-ph.HE].

[26] **Super-Kamiokande Collaboration** Collaboration, Y. Ashie *et al.*, "A Measurement of atmospheric neutrino oscillation parameters by SUPER-KAMIOKANDE I," *Phys.Rev.* **D71** (2005) 112005, arXiv:hep-ex/0501064 [hep-ex].

[27] L. K. Pik, *Study of the neutrino mass hierarchy with the atmospheric neutrino data observed in Super-Kamiokande*. PhD thesis, University of Tokyo, October, 2012. http://www-sk.icrr.u-tokyo.ac.jp/sk/pub/index.html#dthesis.

[28] **Super-Kamiokande Collaboration** Collaboration, Y. Ashie *et al.*, "Evidence for an oscillatory signature in atmospheric neutrino oscillation," *Phys.Rev.Lett.* **93** (2004) 101801, arXiv:hep-ex/0404034 [hep-ex].

[29] V. Kopeikin, L. Mikaelyan, and V. Sinev, "Reactor as a source of antineutrinos: Thermal fission energy," *Phys.Atom.Nucl.* **67** (2004) 1892–1899, arXiv:hep-ph/0410100 [hep-ph].

[30] P. Huber, "On the determination of anti-neutrino spectra from nuclear reactors," *Phys.Rev.* **C84** (2011) 024617, arXiv:1106.0687 [hep-ph].

[31] T. Mueller, D. Lhuillier, M. Fallot, A. Letourneau, S. Cormon, *et al.*, "Improved Predictions of Reactor Antineutrino Spectra," *Phys.Rev.* **C83** (2011) 054615, arXiv:1101.2663 [hep-ex].

[32] K. Abazajian, M. Acero, S. Agarwalla, A. Aguilar-Arevalo, C. Albright, *et al.*, "Light Sterile Neutrinos: A White Paper," arXiv:1204.5379 [hep-ph].

[33] P. Vogel and J. F. Beacom, "Angular distribution of neutron inverse beta decay, $\bar{\nu}_e + p \to e^+ + n$," *Phys.Rev.* **D60** (1999) 053003, arXiv:hep-ph/9903554 [hep-ph].

[34] A. Palazzo, "Constraints on very light sterile neutrinos from θ_{13}-sensitive reactor experiments," *JHEP* **1310** (2013) 172, arXiv:1308.5880 [hep-ph].

[35] **Daya Bay Collaboration** Collaboration, F. An *et al.*, "Spectral measurement of electron antineutrino oscillation amplitude and frequency at Daya Bay," arXiv:1310.6732 [hep-ex].

[36] **Daya Bay Collaboration** Collaboration, F. An *et al.*, "Improved Measurement of Electron Antineutrino Disappearance at Daya Bay," *Chin.Phys.* **C37** (2013) 011001, arXiv:1210.6327 [hep-ex].

[37] **T2K Collaboration** Collaboration, K. Abe *et al.*, "Observation of Electron Neutrino Appearance in a Muon Neutrino Beam," *Phys.Rev.Lett.* **112** (2014) 061802, arXiv:1311.4750 [hep-ex].

[38] **T2K Collaboration** Collaboration, K. Abe *et al.*, "Evidence of Electron Neutrino Appearance in a Muon Neutrino Beam," *Phys.Rev.* **D88** no. 3, (2013) 032002, arXiv:1304.0841 [hep-ex].

[39] **MINOS Collaboration** Collaboration, P. Adamson *et al.*, "Measurement of Neutrino and Antineutrino Oscillations Using Beam and Atmospheric Data in MINOS," *Phys.Rev.Lett.* **110** (2013) 251801, arXiv:1304.6335 [hep-ex].

[40] **MINOS Collaboration** Collaboration, P. Adamson *et al.*, "Electron neutrino and antineutrino appearance in the full MINOS data sample," *Phys.Rev.Lett.* **110** no. 17, (2013) 171801, arXiv:1301.4581 [hep-ex].

[41] P. Huber, M. Lindner, and W. Winter, "Simulation of long-baseline neutrino oscillation experiments with GLoBES (General Long Baseline Experiment Simulator)," *Comput.Phys.Commun.* **167** (2005) 195, arXiv:hep-ph/0407333 [hep-ph].

[42] P. Huber, J. Kopp, M. Lindner, M. Rolinec, and W. Winter, "New features in the simulation of neutrino oscillation experiments with GLoBES 3.0: General Long Baseline Experiment Simulator," *Comput.Phys.Commun.* **177** (2007) 432–438, arXiv:hep-ph/0701187 [hep-ph].

[43] B. Cleveland, T. Daily, J. Davis, Raymond, J. R. Distel, K. Lande, *et al.*, "Measurement of the solar electron neutrino flux with the Homestake chlorine detector," *Astrophys.J.* **496** (1998) 505–526.

[44] F. Kaether, W. Hampel, G. Heusser, J. Kiko, and T. Kirsten, "Reanalysis of the GALLEX solar neutrino flux and source experiments," *Phys.Lett.* **B685** (2010) 47–54, arXiv:1001.2731 [hep-ex].

[45] **SAGE Collaboration** Collaboration, J. Abdurashitov *et al.*, "Measurement of the solar neutrino capture rate with gallium metal. III: Results for the 2002–2007 data-taking period," *Phys.Rev.* **C80** (2009) 015807, arXiv:0901.2200 [nucl-ex].

[46] G. Bellini, J. Benziger, D. Bick, S. Bonetti, G. Bonfini, *et al.*, "Precision measurement of the 7Be solar neutrino interaction rate in Borexino," *Phys.Rev.Lett.* **107** (2011) 141302, arXiv:1104.1816 [hep-ex].

[47] **SNO Collaboration** Collaboration, B. Aharmim *et al.*, "An Independent Measurement of the Total Active B-8 Solar Neutrino Flux Using an Array of He-3 Proportional

Counters at the Sudbury Neutrino Observatory," *Phys.Rev.Lett.* **101** (2008) 111301, arXiv:0806.0989 [nucl-ex].

[48] **Super-Kamiokande Collaboration** Collaboration, J. Hosaka *et al.*, "Solar neutrino measurements in super-Kamiokande-I," *Phys.Rev.* **D73** (2006) 112001, arXiv:hep-ex/0508053 [hep-ex].

[49] **Super-Kamiokande Collaboration** Collaboration, J. Cravens *et al.*, "Solar neutrino measurements in Super-Kamiokande-II," *Phys.Rev.* **D78** (2008) 032002, arXiv:0803.4312 [hep-ex].

[50] **Super-Kamiokande Collaboration** Collaboration, K. Abe *et al.*, "Solar neutrino results in Super-Kamiokande-III," *Phys.Rev.* **D83** (2011) 052010, arXiv:1010.0118 [hep-ex].

[51] **Super-Kamiokande Collaboration** Collaboration, A. Renshaw, "Solar Neutrino Results from Super-Kamiokande," arXiv:1403.4575 [hep-ex].

[52] T. Schwetz, M. Tortola, and J. Valle, "Global neutrino data and recent reactor fluxes: status of three-flavour oscillation parameters," *New J.Phys.* **13** (2011) 063004, arXiv:1103.0734 [hep-ph].

[53] T. Schwetz, M. Tortola, and J. Valle, "Where we are on θ_{13}: addendum to 'Global neutrino data and recent reactor fluxes: status of three-flavour oscillation parameters'," *New J.Phys.* **13** (2011) 109401, arXiv:1108.1376 [hep-ph].

[54] **RENO collaboration** Collaboration, J. Ahn *et al.*, "Observation of Reactor Electron Antineutrino Disappearance in the RENO Experiment," *Phys.Rev.Lett.* **108** (2012) 191802, arXiv:1204.0626 [hep-ex].

[55] **Double Chooz Collaboration** Collaboration, Y. Abe *et al.*, "Reactor electron antineutrino disappearance in the Double Chooz experiment," *Phys.Rev.* **D86** (2012) 052008, arXiv:1207.6632 [hep-ex].

[56] S. Seon-Hee, "Recent Results from RENO." https://conferences.lbl.gov/contributionDisplay.py?contribId=121&sessionId=36&confId=36, Sep, 2013.

[57] **T2K Collaboration** Collaboration, K. Abe *et al.*, "Precise Measurement of the Neutrino Mixing Parameter θ_{23} from Muon Neutrino Disappearance in an Off-axis Beam," *Phys.Rev.Lett.* **112** (2014) 181801, arXiv:1403.1532 [hep-ex].

[58] **T2K Collaboration** Collaboration, K. Abe *et al.*, "Measurement of Neutrino Oscillation Parameters from Muon Neutrino Disappearance with an Off-axis Beam," *Phys.Rev.Lett.* **111** no. 21, (2013) 211803, arXiv:1308.0465 [hep-ex].

[59] **KamLAND Collaboration** Collaboration, A. Gando *et al.*, "Constraints on θ_{13} from A Three-Flavor Oscillation Analysis of Reactor Antineutrinos at KamLAND," *Phys.Rev.* **D83** (2011) 052002, arXiv:1009.4771 [hep-ex].

[60] **Super-Kamiokande Collaboration** Collaboration, R. Wendell *et al.*, "Atmospheric neutrino oscillation analysis with sub-leading effects in Super-Kamiokande I, II, and III," *Phys.Rev.* **D81** (2010) 092004, arXiv:1002.3471 [hep-ex].

[61] Y. Itow, "Recent results in atmospheric neutrino oscillations in the light of large Θ_{13}," *Nucl.Phys.Proc.Suppl.* **235-236** (2013) 79–86.

[62] **Collaboration for the Super-Kamiokande** Collaboration, A. Himmel, "Recent Atmospheric Neutrino Results from Super-Kamiokande," arXiv:1310.6677 [hep-ex].

[63] M. Gonzalez-Garcia, M. Maltoni, J. Salvado, and T. Schwetz, "Global fit to three neutrino mixing: critical look at present precision," *JHEP* **1212** (2012) 123, arXiv:1209.3023 [hep-ph].

[64] M. Gonzalez-Garcia, M. Maltoni, J. Salvado, and T. Schwetz. http://www.nu-fit.org/.

[65] F. Capozzi, G. Fogli, E. Lisi, A. Marrone, D. Montanino, *et al.*, "Status of three-neutrino oscillation parameters, circa 2013," *Phys.Rev.* **D89** (2014) 093018, arXiv:1312.2878 [hep-ph].

[66] K. Babu, E. Ma, and J. Valle, "Underlying A(4) symmetry for the neutrino mass matrix and the quark mixing matrix," *Phys.Lett.* **B552** (2003) 207–213, arXiv:hep-ph/0206292 [hep-ph].

[67] G. Altarelli and F. Feruglio, "Tri-bimaximal neutrino mixing from discrete symmetry in extra dimensions," *Nucl.Phys.* **B720** (2005) 64–88, arXiv:hep-ph/0504165 [hep-ph].

[68] G. Branco, R. G. Felipe, and F. Joaquim, "Leptonic CP Violation," *Rev.Mod.Phys.* **84** (2012) 515–565, arXiv:1111.5332 [hep-ph].

[69] P. Harrison, D. Perkins, and W. Scott, "Tri-bimaximal mixing and the neutrino oscillation data," *Phys.Lett.* **B530** (2002) 167, arXiv:hep-ph/0202074 [hep-ph].

[70] M. Hirsch, J. Romao, S. Skadhauge, J. Valle, and A. Villanova del Moral, "Phenomenological tests of supersymmetric A(4) family symmetry model of neutrino mass," *Phys.Rev.* **D69** (2004) 093006, arXiv:hep-ph/0312265 [hep-ph].

[71] S. Morisi, D. Forero, J. Romão, and J. Valle, "Neutrino mixing with revamped A_4 flavor symmetry," *Phys.Rev.* **D88** no. 1, (2013) 016003, arXiv:1305.6774 [hep-ph].

[72] M. Boucenna, M. Hirsch, S. Morisi, E. Peinado, M. Taoso, *et al.*, "Phenomenology of Dark Matter from A_4 Flavor Symmetry," *JHEP* **1105** (2011) 037, arXiv:1101.2874 [hep-ph].

[73] E. Ma and G. Rajasekaran, "Softly broken A(4) symmetry for nearly degenerate neutrino masses," *Phys.Rev.* **D64** (2001) 113012, arXiv:hep-ph/0106291 [hep-ph].

[74] S. Weinberg, "Varieties of Baryon and Lepton Nonconservation," *Phys.Rev.* **D22** (1980) 1694.

[75] P. Minkowski, "$\mu \to e\gamma$ at a Rate of One Out of 1-Billion Muon Decays?," *Phys.Lett.* **B67** (1977) 421.

[76] M. Gell-Mann, P. Ramond, and R. Slansky, "Complex Spinors and Unified Theories," *Conf.Proc.* **C790927** (1979) 315–321, arXiv:1306.4669 [hep-th].

[77] T. Yanagida, "Horizontal Symmetry and Masses of Neutrinos," *Conf.Proc.* **C7902131** (1979) 95–99.

[78] R. N. Mohapatra and G. Senjanovic, "Neutrino Mass and Spontaneous Parity Violation," *Phys.Rev.Lett.* **44** (1980) 912.

[79] R. Mohapatra and J. Valle, "Neutrino Mass and Baryon Number Nonconservation in Superstring Models," *Phys.Rev.* **D34** (1986) 1642.

[80] M. Malinsky, J. Romao, and J. Valle, "Novel supersymmetric SO(10) seesaw mechanism," *Phys.Rev.Lett.* **95** (2005) 161801, arXiv:hep-ph/0506296 [hep-ph].

[81] J. Bernabeu, A. Santamaria, J. Vidal, A. Mendez, and J. Valle, "Lepton Flavor Nonconservation at High-Energies in a Superstring Inspired Standard Model," *Phys.Lett.* **B187** (1987) 303.

[82] M. Gonzalez-Garcia and J. Valle, "Enhanced lepton flavor violation with massless neutrinos: A Study of muon and tau decays," *Mod.Phys.Lett.* **A7** (1992) 477–488.

[83] G. Branco, M. Rebelo, and J. Valle, "Leptonic CP Violation With Massless Neutrinos," *Phys.Lett.* **B225** (1989) 385.

[84] N. Rius and J. Valle, "Leptonic CP Violating Asymmetries in Z^0 Decays," *Phys.Lett.* **B246** (1990) 249–255.

[85] S. Antusch, J. P. Baumann, and E. Fernandez-Martinez, "Non-Standard Neutrino Interactions with Matter from Physics Beyond the Standard Model," *Nucl.Phys.* **B810** (2009) 369–388, arXiv:0807.1003 [hep-ph].

[86] M. Malinsky, T. Ohlsson, and H. Zhang, "Non-unitarity effects in a realistic low-scale seesaw model," *Phys.Rev.* **D79** (2009) 073009, arXiv:0903.1961 [hep-ph].

[87] P. B. Dev and R. Mohapatra, "TeV Scale Inverse Seesaw in SO(10) and Leptonic Non-Unitarity Effects," *Phys.Rev.* **D81** (2010) 013001, arXiv:0910.3924 [hep-ph].

[88] J. Valle, "Resonant Oscillations of Massless Neutrinos in Matter," *Phys.Lett.* **B199** (1987) 432.

[89] H. Nunokawa, Y. Qian, A. Rossi, and J. Valle, "Resonant conversion of massless neutrinos in supernovae," *Phys.Rev.* **D54** (1996) 4356–4363, arXiv:hep-ph/9605301 [hep-ph].

[90] O. Miranda, M. Tortola, and J. Valle, "Are solar neutrino oscillations robust?," *JHEP* **0610** (2006) 008, arXiv:hep-ph/0406280 [hep-ph].

[91] B. W. Lee and R. E. Shrock, "Natural Suppression of Symmetry Violation in Gauge Theories: Muon - Lepton and Electron Lepton Number Nonconservation," *Phys.Rev.* **D16** (1977) 1444.

[92] J. Schechter and J. Valle, "Neutrino Decay and Spontaneous Violation of Lepton Number," *Phys.Rev.* **D25** (1982) 774.

[93] **Particle Data Group** Collaboration, K. Nakamura *et al.*, "Review of particle physics," *J.Phys.* **G37** (2010) 075021.

[94] **MEG collaboration** Collaboration, J. Adam *et al.*, "New limit on the lepton-flavour violating decay $\mu^+ \to e^+\gamma$," *Phys.Rev.Lett.* **107** (2011) 171801, arXiv:1107.5547 [hep-ex].

[95] **MEGA Collaboration** Collaboration, M. Ahmed *et al.*, "Search for the lepton family-number-nonconserving decay $\mu \to e + \gamma$," *Phys.Rev.* **D65** (2002) 112002, arXiv:hep-ex/0111030 [hep-ex].

[96] D. Ibanez, S. Morisi, and J. Valle, "Inverse tri-bimaximal type-III seesaw and lepton flavor violation," *Phys.Rev.* **D80** (2009) 053015, arXiv:0907.3109 [hep-ph].

[97] **ISS Physics Working Group** Collaboration, A. Bandyopadhyay *et al.*, "Physics at a future Neutrino Factory and super-beam facility," *Rept.Prog.Phys.* **72** (2009) 106201, arXiv:0710.4947 [hep-ph].

[98] D. Forero, S. Morisi, M. Tortola, and J. Valle, "Lepton flavor violation and non-unitary lepton mixing in low-scale type-I seesaw," *JHEP* **1109** (2011) 142, arXiv:1107.6009 [hep-ph].

[99] S. Weinberg, *The Quantum theory of fields. Vol. 1: Foundations*. Cambridge University Press, first ed., 1995.

[100] S. Willenbrock, "Symmetries of the standard model," arXiv:hep-ph/0410370 [hep-ph].

[101] M. E. Peskin, "Beyond the standard model," arXiv:hep-ph/9705479 [hep-ph].

[102] T. Cheng and L. Li, *Gauge theory of elementary particle physics*. Oxford University Press, first ed., 1984.

[103] R. Foot, H. Lew, X. He, and G. C. Joshi, "Seesaw Neutrino Masses Induced by a Triplet of Leptons," *Z.Phys.* **C44** (1989) 441.

[104] W. Grimus, "Neutrino Physics - Models for Neutrino Masses and Lepton Mixing," *PoS* **P2GC** (2006) 001, arXiv:hep-ph/0612311 [hep-ph].

[105] G. Senjanovic, "Neutrino mass: From LHC to grand unification," *Riv.Nuovo Cim.* **034** (2011) 1–68.

[106] E. K. Akhmedov, M. Lindner, E. Schnapka, and J. Valle, "Dynamical left-right symmetry breaking," *Phys.Rev.* **D53** (1996) 2752–2780, arXiv:hep-ph/9509255 [hep-ph].

[107] D. Wyler and L. Wolfenstein, "Massless Neutrinos in Left-Right Symmetric Models," *Nucl.Phys.* **B218** (1983) 205.

[108] M. Dittmar, A. Santamaria, M. Gonzalez-Garcia, and J. Valle, "Production Mechanisms and Signatures of Isosinglet Neutral Heavy Leptons in Z^0 Decays," *Nucl.Phys.* **B332** (1990) 1.

[109] G. 't Hooft, C. Itzykson, A. Jaffe, H. Lehmann, P. Mitter, *et al.*, "Recent Developments in Gauge Theories. Proceedings, Nato Advanced Study Institute, Cargese, France, August 26 - September 8, 1979," *NATO Adv.Study Inst.Ser.B Phys.* **59** (1980) pp.1–438.

[110] S. Barr and I. Dorsner, "A Prediction from the type III see-saw mechanism," *Phys.Lett.* **B632** (2006) 527–531, arXiv:hep-ph/0507067 [hep-ph].

[111] F. Bazzocchi, D. Cerdeno, C. Munoz, and J. Valle, "Calculable inverse-seesaw neutrino masses in supersymmetry," *Phys.Rev.* **D81** (2010) 051701, arXiv:0907.1262 [hep-ph].

[112] E. K. Akhmedov, M. Lindner, E. Schnapka, and J. Valle, "Left-right symmetry breaking in NJL approach," *Phys.Lett.* **B368** (1996) 270–280, arXiv:hep-ph/9507275 [hep-ph].

[113] M. Hirsch, S. Morisi, and J. Valle, "A4-based tri-bimaximal mixing within inverse and linear seesaw schemes," *Phys.Lett.* **B679** (2009) 454–459, arXiv:0905.3056 [hep-ph].

[114] H. Hettmansperger, M. Lindner, and W. Rodejohann, "Phenomenological Consequences of sub-leading Terms in See-Saw Formulas," *JHEP* **1104** (2011) 123, arXiv:1102.3432 [hep-ph].

[115] M. Raidal, A. van der Schaaf, I. Bigi, M. Mangano, Y. K. Semertzidis, *et al.*, "Flavour physics of leptons and dipole moments," *Eur.Phys.J.* **C57** (2008) 13–182, arXiv:0801.1826 [hep-ph].

[116] **MEG Collaboration** Collaboration, J. Adam *et al.*, "New constraint on the existence of the $\mu^+ \to e^+\gamma$ decay," *Phys.Rev.Lett.* **110** no. 20, (2013) 201801, arXiv:1303.0754 [hep-ex].

[117] **SINDRUM Collaboration** Collaboration, U. Bellgardt *et al.*, "Search for the Decay $\mu^+ \to e^+e^+e^-$," *Nucl.Phys.* **B299** (1988) 1.

[118] P. Wintz, "Results of the SINDRUM-II experiment," *Conf.Proc.* **C980420** (1998) 534–546.

[119] **SINDRUM II Collaboration** Collaboration, W. H. Bertl *et al.*, "A Search for muon to electron conversion in muonic gold," *Eur.Phys.J.* **C47** (2006) 337–346.

[120] **BaBar Collaboration** Collaboration, B. Aubert *et al.*, "Searches for Lepton Flavor Violation in the Decays $\tau^{+-} \to e^{+-}\gamma$ and $\tau^{+-} \to \mu^{+-}\gamma$," *Phys.Rev.Lett.* **104** (2010) 021802, arXiv:0908.2381 [hep-ex].

[121] K. Hayasaka, K. Inami, Y. Miyazaki, K. Arinstein, V. Aulchenko, *et al.*, "Search for Lepton Flavor Violating Tau Decays into Three Leptons with 719 Million Produced Tau+Tau- Pairs," *Phys.Lett.* **B687** (2010) 139–143, arXiv:1001.3221 [hep-ex].

[122] T. Toma and A. Vicente, "Lepton Flavor Violation in the Scotogenic Model," *JHEP* **1401** (2014) 160, arXiv:1312.2840.

[123] F. Deppisch, T. Kosmas, and J. Valle, "Enhanced mu- - e- conversion in nuclei in the inverse seesaw model," *Nucl.Phys.* **B752** (2006) 80–92, arXiv:hep-ph/0512360 [hep-ph].

[124] R. Alonso, M. Dhen, M. Gavela, and T. Hambye, "Muon conversion to electron in nuclei in type-I seesaw models," *JHEP* **1301** (2013) 118, arXiv:1209.2679 [hep-ph].

[125] J. Hisano, T. Moroi, K. Tobe, and M. Yamaguchi, "Lepton flavor violation via right-handed neutrino Yukawa couplings in supersymmetric standard model," *Phys.Rev.* **D53** (1996) 2442–2459, arXiv:hep-ph/9510309 [hep-ph].

[126] S. Glashow, J. Iliopoulos, and L. Maiani, "Weak Interactions with Lepton-Hadron Symmetry," *Phys.Rev.* **D2** (1970) 1285–1292.

[127] A. Ilakovac and A. Pilaftsis, "Flavor violating charged lepton decays in seesaw-type models," *Nucl.Phys.* **B437** (1995) 491, arXiv:hep-ph/9403398 [hep-ph].

[128] F. Deppisch and J. Valle, "Enhanced lepton flavor violation in the supersymmetric inverse seesaw model," *Phys.Rev.* **D72** (2005) 036001, arXiv:hep-ph/0406040 [hep-ph].

[129] B. He, T. Cheng, and L.-F. Li, "A Less suppressed mu-e-gamma and tau-nu-gamma loop amplitude and extra dimension theories," *Phys.Lett.* **B553** (2003) 277–283, arXiv:hep-ph/0209175 [hep-ph].

[130] L. Lavoura, "General formulae for f1–> f2 gamma," *Eur.Phys.J.* **C29** (2003) 191–195, arXiv:hep-ph/0302221 [hep-ph].

[131] J. Casas and A. Ibarra, "Oscillating neutrinos and muon –> e, gamma," *Nucl.Phys.* **B618** (2001) 171–204, arXiv:hep-ph/0103065 [hep-ph].

[132] G. D'Ambrosio, G. Giudice, G. Isidori, and A. Strumia, "Minimal flavor violation: An Effective field theory approach," *Nucl.Phys.* **B645** (2002) 155–187, arXiv:hep-ph/0207036 [hep-ph].

[133] V. Cirigliano, B. Grinstein, G. Isidori, and M. B. Wise, "Minimal flavor violation in the lepton sector," *Nucl.Phys.* **B728** (2005) 121–134, arXiv:hep-ph/0507001 [hep-ph].

[134] R. Alonso, G. Isidori, L. Merlo, L. A. Munoz, and E. Nardi, "Minimal flavour violation extensions of the seesaw," *JHEP* **1106** (2011) 037, arXiv:1103.5461 [hep-ph].

[135] S. Kovalenko, Z. Lu, and I. Schmidt, "Lepton Number Violating Processes Mediated by Majorana Neutrinos at Hadron Colliders," *Phys.Rev.* **D80** (2009) 073014, arXiv:0907.2533 [hep-ph].

[136] A. Atre, T. Han, S. Pascoli, and B. Zhang, "The Search for Heavy Majorana Neutrinos," *JHEP* **0905** (2009) 030, arXiv:0901.3589 [hep-ph].

[137] E. Roulet, "MSW effect with flavor changing neutrino interactions," *Phys.Rev.* **D44** (1991) 935–938.

[138] M. Guzzo, A. Masiero, and S. Petcov, "On the MSW effect with massless neutrinos and no mixing in the vacuum," *Phys.Lett.* **B260** (1991) 154–160.

[139] J. Kopp, M. Lindner, T. Ota, and J. Sato, "Non-standard neutrino interactions in reactor and superbeam experiments," *Phys.Rev.* **D77** (2008) 013007, arXiv:0708.0152 [hep-ph].

[140] Z. Berezhiani and A. Rossi, "Limits on the nonstandard interactions of neutrinos from e+ e- colliders," *Phys.Lett.* **B535** (2002) 207–218, arXiv:hep-ph/0111137 [hep-ph].

[141] S. Davidson, C. Pena-Garay, N. Rius, and A. Santamaria, "Present and future bounds on nonstandard neutrino interactions," *JHEP* **0303** (2003) 011, arXiv:hep-ph/0302093 [hep-ph].

[142] J. Barranco, O. Miranda, C. Moura, and J. Valle, "Constraining non-standard interactions in nu(e) e or anti-nu(e) e scattering," *Phys.Rev.* **D73** (2006) 113001, arXiv:hep-ph/0512195 [hep-ph].

[143] J. Barranco, O. Miranda, C. Moura, and J. Valle, "Constraining non-standard neutrino-electron interactions," *Phys.Rev.* **D77** (2008) 093014, arXiv:0711.0698 [hep-ph].

[144] D. Forero and M. Guzzo, "Constraining nonstandard neutrino interactions with electrons," *Phys.Rev.* **D84** (2011) 013002.

[145] G. Mangano, G. Miele, S. Pastor, T. Pinto, O. Pisanti, *et al.*, "Effects of non-standard neutrino-electron interactions on relic neutrino decoupling," *Nucl.Phys.* **B756** (2006) 100–116, arXiv:hep-ph/0607267 [hep-ph].

[146] R. Leitner, M. Malinsky, B. Roskovec, and H. Zhang, "Non-standard antineutrino interactions at Daya Bay," *JHEP* **1112** (2011) 001, arXiv:1105.5580 [hep-ph].

[147] C. Biggio, M. Blennow, and E. Fernandez-Martinez, "Loop bounds on non-standard neutrino interactions," *JHEP* **0903** (2009) 139, arXiv:0902.0607 [hep-ph].

[148] C. Biggio, M. Blennow, and E. Fernandez-Martinez, "General bounds on non-standard neutrino interactions," *JHEP* **0908** (2009) 090, arXiv:0907.0097 [hep-ph].

[149] G. Mention, M. Fechner, T. Lasserre, T. Mueller, D. Lhuillier, *et al.*, "The Reactor Antineutrino Anomaly," *Phys.Rev.* **D83** (2011) 073006, arXiv:1101.2755 [hep-ex].

[150] A. Hayes, J. Friar, G. Garvey, G. Jungman, and G. Jonkmans, "Systematic Uncertainties in the Analysis of the Reactor Neutrino Anomaly," *Phys.Rev.Lett.* **112** (2014) 202501, arXiv:1309.4146 [nucl-th].

[151] T. Cheng and L. Li, *Gauge theory of elementary particle physics: Problems and solutions*. Oxford University Press, first ed., 2000.

[152] B. Lee, S. Pakvasa, R. Shrock, and H. Sugawara, "Muon and Electron Number Nonconservation in a v-a Six Quark Model," *Phys.Rev.Lett.* **38** (1977) 937.

[153] T. Cheng and L.-F. Li, "$\mu \to e\gamma$ in Theories With Dirac and Majorana Neutrino Mass Terms," *Phys.Rev.Lett.* **45** (1980) 1908.

[154] S. Antusch, C. Biggio, E. Fernandez-Martinez, M. Gavela, and J. Lopez-Pavon, "Unitarity of the Leptonic Mixing Matrix," *JHEP* **0610** (2006) 084, arXiv:hep-ph/0607020 [hep-ph].

[155] J. Schechter and J. Valle, "Neutrino Decay and Spontaneous Violation of Lepton Number," *Phys.Rev.* **D25** (1982) 774.